2018

Single Enzyme Biomineralization of Semiconductor Nanocrystals

Leah Spangler
Lehigh University

SINGLE ENZYME BIOMINERALIZATION OF SEMICONDUCTOR NANOCRYSTALS

by

Leah Spangler

A Dissertation Presented to the Graduate and Research Committee
of Lehigh University
in Candidacy for the Degree of
Doctor of Philosophy

in
Chemical Engineering

Lehigh University
Bethlehem, PA

May 2018

Approved and recommended for acceptance as a dissertation in partial fulfillment of requirements for the degree of Doctor of Philosophy.

_____
Date

_____
Steven McIntosh
(Dissertation Advisor)

_____
Accepted Date

Committee members:

_____
Bryan W. Berger

_____
Christopher J. Kiely

_____
Angela Brown

Acknowledgments

The completion of this work would not have been possible without the support of my family and friends. Firstly, I would like to thank my parents, Skip and DJ Spangler, who have always encouraged me in all of my endeavors, whether it was school, writing, ballet, or music. I also want to thank them for showing me how to be a leader, and for teaching me the importance of kindness, patience, and perseverance. I also want to thank my brother, Joel, and sister, Beckah, to whom I owe my great taste in music and wonderful sense of humor.

I would like to thank my advisor, Steven McIntosh, for not only teaching me how to be an effective researcher, but for giving me a lot of great career and life advice along the way. I'd also like to thank Christopher Kiely for his constant optimism and enthusiasm, even during times when I thought my project was going terribly.

I have had many great friends at Lehigh who have made my time in graduate school a lot of fun: Zhou Yang, Evan Koufus, Chris Curran, Li Lu, Matt Wehrman, Matt Urich, Justin B. Nice, Shannon Collins, Roxanne Chu, Nate Sallada, Hamid Sadeghnejad, John Sakizadeh, and many more.

Finally, I want to thank Daniel Gregory, who I cannot possibly ever thank enough, for all of the advice, ideas, feedback, support, help and laughter he has provided along every step of the way.

Contents

List of Tables

List of Figures

Abstract

Biomineralization, the process by which living organisms generate minerals, has recently gained interest as a pathway towards the green synthesis of crystalline materials under ambient conditions for energy and catalytic applications. Semiconductor quantum dots are desirable for their size-tunable optical and electronic properties but their commercial use is currently cost-limited due to the high temperatures and stringent reaction conditions employed during synthesis. Biomineralization offers a low cost, greener approach to synthesis as quantum dots are synthesized in the aqueous phase at ambient temperature and pressure. These nanocrystals are well suited for biological applications as they are capped with DNA, amino acids, or short-chain peptides. This work seeks to better understand the biomineralization of quantum dots by *Stenotrophomonas maltophilia* through the study of proteins excreted in response to high concentrations of heavy metals. One enzyme, cystathionine γ-lyase (CSE), has been identified as playing the main role in both catalyzing mineralization and controlling growth by continuously generating a reactive sulfur species, H_2S, from the amino acid L-cysteine. CSE was then isolated and utilized for the direct, single enzyme synthesis of many types of metal chalcogenide nanocrystals. Specifically, we have prepared and characterized CdS, PbS, and $CuInS_2$ nanocrystals using CSE. Additionally, we demonstrate the biomineralization of core/shell quantum dots

(e.g. PbS/CdS and $CuInS_2$/ZnS) using a sequential growth method. Tunable optical properties are confirmed by absorbance and photoluminescence measurements. HRTEM and HAADF are utilized to determine the size distribution and crystal phase of the resulting nanocrystals, while single particle XEDS confirms the composition. The functional properties of these materials are demonstrated by their incorporation into quantum dot sensitized solar cells, as fluorescent markers for the bio-imaging of cancer cells, and as a stable photocatalyst for H_2 generation. Lastly, nanocrystal biomineralization by CSE is studied in the context of classical theories for colloidal particle nucleation and growth to better understand the effect of synthesis parameters on the resultant quantum dot populations.

Chapter 1

Introduction

1.1 Motivation

Semiconductor quantum dots or nanocrystals have many unique optical and electronic properties which make them desirable for use in solar cells, photocatalysis, LEDs, and bio-imaging. However, quantum dots have yet to be used commercially on a large scale due to costly synthesis routes that require toxic chemicals and high temperatures or pressures.[3] Additionally, most bio-applications require quantum dots in the aqueous phase or in biologically relevant buffers. While several groups have attempted aqueous synthesis of quantum dots with some success most still require high temperatures or the addition of a strong reducing agent to achieve crystallization.[4, 5]

Biomineralization is the process by which organisms make crystalline materials for various functions and structural support. While this was first observed and studied in entire organisms, the existance of biomineralization pathways that consists of organic biomolecules capable of synthesizing and templating crystal growth have recently been discovered.[6] Many groups have now looked towards biomineralization as an

aqueous, green route to synthesis of crystalline materials for energy and catalysis applications. In particular, quantum dots synthesized using biological routes are beneficial for bio-imaging applications, which require nanocrystals that are stable in biologically relevant buffers. While several groups have studied the biosynthesis of quantum dots using both organisms and isolated proteins, little work has been done to understand the synthesis mechanism of biomineralization or to improve upon it from a biological standpoint. Improvements to nanoparticle stability and optical properties are needed before biomineralized quantum dots can be used commercially.

This work first studies the biomineralization of metal chalcogenide quantum dots by the bacteria *Stenotrophomonas maltophilia* (SMCD1). Next, the pathway to mineralization is studied by examining cystathionine γ-lyase (CSE), one of the enzymes associated with quantum dot biomineralization by SMCD1. Both SMCD1 and CSE can synthesize several types of metal sulfide nanoparticles, such as CdS, PbS, and $CuInS_2$, without further modification, demonstrating the generality of the synthesis mechanism. Additionally, the ability of CSE to form core/shell structures such as PbS/CdS and $CuInS_2$/ZnS, improves the optical properties of the as synthesized quantum dots under the same ambient conditions. The nanocrystals are all synthesized with size-control and optical properties consistent with quantum dots produced using traditional chemical synthesis techniques. The functional properties of the biosynthetic quantum dots are demonstrated by using them in various applications; quantum dot sensitized solar cells, bio-imaging of cancer cells, and as photocatalysts.

1.2 Background

1.2.1 Quantum Dots, Quantum Confinement and the Origin of Optical Properties

Quantum dots are semiconductor nanocrystals, often only 1-10 nm in size, that have optical properties that differ from the corresponding bulk semiconductor material due to their small size. Typically, these nanocrystals are only 10-50 atoms and can be considered as a species that exists between molecules and bulk crystals. Molecules are only made up of a few atoms, and their electron binding can be described as discrete energy states or binding orbitals. A bulk crystal, on the other hand, has many atoms and electron interactions, and these energy levels overlap and form valence and conduction bands.[4, 7, 8]

The bandgap, or the spacing between these two bands, is a constant for each material when the radius of the crystallites is equal to or larger than the Bohr radius. The Bohr radius is a physical constant and was originally used to describe the most probable distance between an electron and a proton in a hydrogen atom. Thus, the Bohr radius of a semiconductor material would be the most probable distance between an electron and the nucleus. If the electrons are confined to an orbit which is smaller than the Bohr radius, quantum confinement occurs. When the electrons are confined spatially, the separation between the valence and conduction bands of the crystallite increases. Thus, the stronger the quantum confinement, the larger the band gap.[8]

This phenomenon causes fluorescence in the UV, visible, or infrared range. The energy of the emitted light depends on the band gap of the material and the amount of quantum confinement. For example, 2 nm CdSe quantum dots will fluoresce blue

light while 6 nm CdSe quantum dots will fluoresce red light. Therefore, the optical properties of a solution of quantum dots can be controlled by tuning the crystallite size.[9]

1.2.2 Traditional Quantum Dot Synthesis Techniques

Quantum dots can be prepared using several techniques. Originally, quantum dots were prepared using lithography or epitaxially grown by molecular beam epitaxy or metal-organic chemical vapor deposition techniques. However, these techniques do not produce free nanocrystals as the quantum dots are attached to a substrate or embedded into a matrix. The development of colloidal routes to nanocrystal growth solved this problem by implementing wet chemistry techniques, resulting in solutions of free quantum dots.[9]

One commonly studied colloidal synthesis route is known as hot injection, and was first demonstrated by Murray *et al.*[3] In this technique, metal precursors are swiftly injected into an organic solution at high temperature. This causes the rapid formation of monomer precursors in solution which provide a favorable environment for crystal nucleation and growth. The crystallites are stabilized by the addition of hydrophobic surfactants which bind preferentially to the crystal surfaces. Organic solvents are used so that elevated temperatures can be employed to obtain high crystallinity and specific crystal phases. Additionally, the organic solvents also play a role in controlling growth rate by binding dynamically to the quantum dots.

A disadvantage of the hot injection synthesis route is the use of organic solvents,

high temperatures, and often inert atmosphere. Specifically, the use of organic solvents results in hydrophobic quantum dots that cannot be used in biological applications without capping exchange to allow resuspension in a biologically relevant buffer. This phase transfer step typically reduces the fluorescent properties of the quantum dots. To avoid this, many groups have begun studying the aqueous synthesis of quantum dots.[4, 5] By synthesizing quantum dots directly in water, no phase transfer step is necessary and less toxic precursors are required. Typical aqueous synthesis of quantum dots consists of mixing reacting metal ions and a chalcogenide precursor in a solution with a stabilizing hydrophilic ligand. Generally, soluble metal salts such as acetates, chlorides, perchlorates, and nitrates are used as a metal precursor. Reactive sulfur is easily obtained by the addition of Na_2S, but can also be derived from the decomposition of thiourea or thioacetamide. Se^{2-} and Te^{2-} are more difficult to obtain and are often supplied by H_2Se and H_2Te derived from corresponding precursors.[7]

Compared to traditional colloidal synthesis, aqueous synthesis results in slower nucleation and growth of the nanocrystals. This allows smaller quantum dots and even 'magic size' clusters of atoms to be formed. These smaller crystallites have stronger quantum confinement and expand the achievable fluorescence range of quantum dots. A disadvantage of this slower growth process is that a perfect arrangement of atoms in the crystallite is more difficult to obtain. This can be remedied by using higher synthesis temperatures or microwave irradiation. However, these techniques will increase the cost of synthesis and limit scale up.[4, 8]

1.2.3 Expected Optical Properties

As mentioned in Section 1.2.1, the optical properties of nanocrystals result from quantum confinement of the electron-hole pairs, or excitons. The confinement causes an increase in band gap with decreasing size of the nanoparticle. Optically, this can be observed by measuring the absorbance of a solution of quantum dots. As the band gap shifts, the absorption onset will blue shift. This onset is usually a sharp peak and corresponds to the lowest excited state of the quantum dots. The position is determined by the band gap, but the intensity and width are determined by the concentration and size distribution of quantum dots in solution, respectively.[7]

Similarly, photoluminescence or fluorescence blue shifts with increasing band gap. The origin of fluorescence is a result of the relaxation of an excited electron from the conduction band down to the valence band. The relaxation energy is emitted as light with energy corresponding to the band gap. The actual maximum value of the photoluminescence spectrum is typically shifted 10-20 nm when compared to the excitonic peak from the absorbance spectra. This phenomenon is known as the Stokes shift and results from the structure of the exciton energy levels within the quantum dot.[10]

An important measure of quality for quantum dots is the quantum yield, which represents the efficiency of emission. Essentially, the quantum yield is a ratio of the number of emitted photons to the number of absorbed photons. This shows how many excited electrons relax via the radiative pathway verses other nonradiative pathways resulting from trap states on the surface. Trap states are extremely common in quantum dots because they have such large surface to volume ratios. They can be passivated by improving the capping agent, or more favorably, by growing an

inorganic shell over the core quantum dot.[10]

1.2.4 Material Characterization Techniques

In addition to characterizing quantum dots optically, material characterization techniques provide structural information about the crystallites. X-ray diffraction (XRD) is commonly used to determine the crystal structure of powders and can also be used to analyze dried quantum dot samples. Peak broadening occurs due to the random orientations of the crystallites, causing diffraction from various crystal planes. The destructive interference, which would typically yield a sharp peak for a bulk crystallite, is reduced and the peak is broadened. By using the Debye-Scherrer formula, an approximate crystallite size can be calculated by using the full-width half-maximum of the broadened peaks.[11, 12]

Another important technique for quantum dot characterization is Transmission Electron Microscopy (TEM). This type of microscope is critical for surpassing the traditional resolution limit of light microscopes. By utilizing electrons, the structure of objects on the nanoscale can be resolved. High resolution TEM (HRTEM) allows the imaging of single atoms, which can be used to determine crystal structure and size. Additionally, the use of a Scanning TEM (STEM) and a High Angle Annular Dark Field (HAADF) detector allows the visualization of different atomic weights of atoms that are present in the sample. Using STEM also allows mapping or line scans of X-ray Energy Dispersive Spectroscopy (XEDS). XEDS is a method that detects x-rays which are generated from the electron interactions with the atoms as they pass through the sample. Each element will emit a characteristic x-ray, allowing elemental composition of a material to be detected.[13]

1.2.5 Alloyed and Core/shell Quantum Dots

The most commonly used materials for quantum dots are II-VI semiconductor compounds. These are typically cadmium or zinc chalcogenides that have emission in the visible range. In order to access the NIR range, more groups are looking towards IV-VI type materials, such as Pb chalcogenides. Another materials group that has gained interest for medical applications are II-V compounds, which use nontoxic elements such as In or Ga.[10]

In addition to binary systems, which tune emission using size control, alloyed or ternary compounds yield optical tuning through composition control. Some early examples were demonstrated with CdZnS, CdZnSe, and CdSeS. Recently, work has been focused on $CuInS_2$ and $CuInSe_2$, which give tunable optical properties in the visible range while remaining nontoxic.[14, 15]

One method for improving optical properties is the growth another semiconductor shell on top of an already synthesized core. The growth of a shell can improve quantum yield by the passivation of surface defects on the crystal surface, or from a change in the electronic structure of the two materials, resulting in trapping of the electrons within the core. Typically, the shell material must have a similar crystal structure and small lattice mismatch to promote crystal growth on the surface of the pre-existing quantum dot.[8, 10]

The shell can be grown two ways; epitaxially on the surface of the quantum dot, increasing overall size, or by cation exchange of the metal ions, resulting in quantum dots of the same size. Epitaxially grown core/shell quantum dots are typically made of CdSe/ZnS or similar II-VI semiconductor materials. Cation exchange has been observed for PbS/CdS core/shell systems as well as $CuInS_2$/ZnS systems.[16, 17]

Cation exchange is more likely to occur when the core material is more labile than the shell material.[18]

1.2.6 Applications of Quantum Dots

Quantum dots are ideal for many types of applications due to the wide variety of materials available for synthesis, large range of emission properties, and compatibility as a result of surface capping. The most developed application in industry are for display technologies, such as televisions. Quantum dots are also suitable to serve as lasers or detectors, especially for the NIR range.[19] Several groups have studied quantum dots for use in catalysis applications, such as water splitting for hydrogen generation. [20]

Another application which is better suited for biomineralized quantum dots in particular is bio-imaging. Many groups have shown that quantum dots can be conjugated to antibodies and used for fluorescent assays or cell labeling. Using nanocrystals offers advantages over traditionally used fluorescent dyes because they can be excited at wavelengths much lower than the emission wavelength, and have a high resistance to photobleaching. Additionally, nanocrystals of two different sizes could be used to tag different parts of the cell and then be excited by the same wavelength of light.[9]

Other groups have used the quantum dots in vivo by targeting specific organs in mice. One concern for biomedical applications are the toxicity of quantum dots. Typically, quantum dots used in these studied have a nontoxic ZnS shell, or more preferably, are made of nontoxic materials such as $CuInS_2$.[21]

1.2.7 Biomineralization of Quantum Dots

Biomineralization is the process living organisms use to generate minerals.[6] These minerals are usually generated for structural support or for a mechanical purpose. Some common examples of organisms that utilize biomineralization are sponges, corals, and crustaceans, who form $CaCO_3$, unicellular eukaryotes, such as diatoms and radiolarians, that form biosilicate cell walls, and Magnetotatic bacteria that use iron oxide nanoparticles for alignment to the Earth's magnetic field.[22] While most examples of biomineralization from nature are observed from entire organisms, the pathway of mineralization can be studied and potentially isolated for independent use. In many cases, the materials are formed under the influence of organic macromolecules produced by the organisms, such as proteins, carbohydrates and lipids. Determining the enzyme or biomolecule responsible for mineralization could lead to a new, low cost synthesis route towards functional materials.

Recently, biomineralization has gained interest as a method for synthesizing quantum dots under biological conditions, i.e. physiological pH and ambient temperature/pressure. Semiconductor nanocrystal biomineralization was first identified in organisms which have detoxification mechanisms against heavy metals.[23, 24, 25] Several yeasts [23, 26], bacteria [25, 27, 28], and even higher order organisms such as earthworms [29] have demonstrated the ability to generate metal chalcogenide nanocrystals when exposed to low concentrations of heavy metals such as Cd or Pb. Additionally, several groups have also studied quantum dot templating in water using biomolecules, such as DNA [30, 31], amino acids [32], or short length peptides [33, 34] to stabilize quantum dots in the aqueous phase. However, these methods still require the addition of a reactive precursor and lack size control of the resultant

nanoparticles.

1.2.8 Directed Evolution of *S. maltophilia* and Identification of CSE

The organism studied for quantum dot synthesis in this work is *S. maltophilia*. This bacteria was chosen due to a known resistance to heavy metal toxicity.[24, 25] Biomineralization by *S. maltophilia* was first achieved with the synthesis of CdS nanocrystals by Yang *et al.* and will be briefly described here.[35] *S. maltophilia* was iteratively subcultured on media containing low concentrations of cadmium. A variant was selected that could tolerate >1mM cadmium concentrations and showed visible fluorescence when excited with UV light. The selected colonies (SMCD1) were then incubated with Cd^{2+} and L-cysteine, an amino acid containing a thiol group, in Tris-HCl buffer. The resulting solutions showed absorbance and fluorescence in the visible range that was only present when all four precursors were in solution and was consistent with the formation of CdS quantum dots. TEM images confirmed the crystallinity of the quantum dots and the crystals fit to either the wurzite or zinc blende phases of CdS; there was not an observed majority crystal phase for the entire population of quantum dots. XEDS of a single particle confirms the presence of Cd and S.

After removing SMCD1 using centrifugation, the supernatant retains optical properties indicative of quantum dots, demonstrating an extracellular quantum dot growth mechanism. Additionally, removing SMCD1 during biomineralization does not stop quantum dot growth but does reduce the rate of synthesis. These observations suggest an enzymatic route to synthesis. Enzymes associated with the biomineralized quantum dots were isolated using an SDS-PAGE gel (shown in Figure 1.1). Bands

corresponding to proteins which are associated with the lyophilized quantum dots were cut from the gel and sent to be analyzed by electrospray ionization mass spectroscopy (ESI-MS). A putative cystathionine γ-lyase (CSE) was identified from the band at 42 kDa. CSE is known to catalyze the decomposition of cysteine to H_2S, which could then be used as a reactive precursor for quantum dot growth.

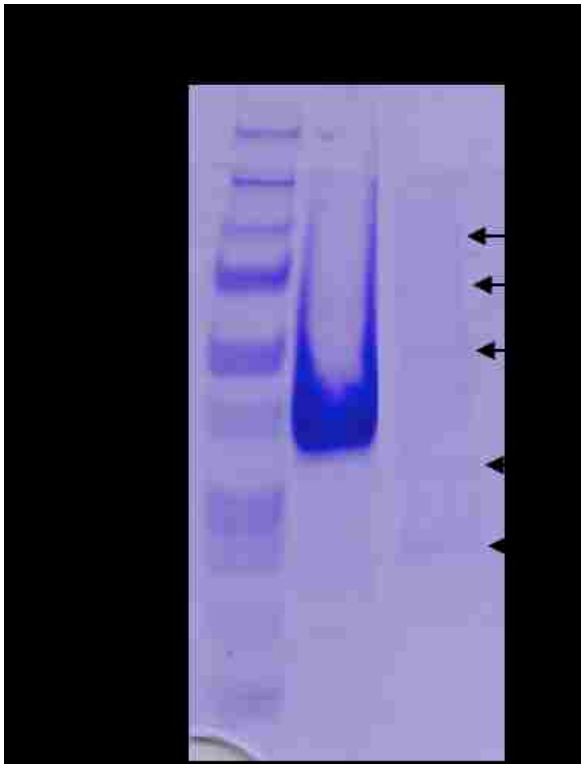

Figure 1.1: Protein gel of recombinant CSE (lane 2) and a concentrated quantum dot solution synthesized by SMCD1 (lane 3). Several bands are shown in addition to a band correlated to smCSE.

1.2.9 Single Enzyme Biomineralization of CdS using CSE

The identified CSE enzyme from SMCD1 biomineralization was independently expressed in *E. coli* using recombinant DNA by Dunleavy *et al.* Recombinant smCSE

was capable of synthesizing CdS quantum dots independently of any other peptides present in solution. CSE come from a class of enzymes known to turn cysteine over to H_2S. This was hypothesized to be the mechanism of quantum dot synthesis and was confirmed by monitoring the generation of H_2S in solution by a lead acetate assay.[36]

Chapter 2

Experimental Details

2.1 Biomineralization of Quantum Dots Using *Stenotrophomonas maltophilia* (SMCD1)

Quantum dot biomineralization was initially developed using an engineered strain of *Stenotrophomonas maltophilia* (SMCD1).[36] This strain was engineered for cadmium tolerance from a wild-type by directed evolution. This same strain was then utilized for PbS and PbS/CdS core/shell quantum dot growth without any further evolution.

SMCD1 was sub-cultured into 100 mL of lysogeny broth and grown for 12 h at 37 °C with shaking. Cells were collected by centrifugation at 5000 rpm for 10 minutes and re-suspended in aqueous Tris-HCl buffer (0.1 M, pH 7.5).

CdS Quantum dot growth was performed by preparing an aqueous solution of cadmium acetate (1 mM, Alfa Aesar Puratronic, 99.995% metals basis), L-cysteine, and SMCD1 (OD_{600}=0.5) in Tris-HCl buffer (pH 7.5). The solutions were incubated at 37 °C with shaking for 30 minutes and then centrifuged for 5 minutes at 8000 rpm

to remove SMCD1 from solution. The solutions were further incubated at 37 °C for up to 6 hours. CdS growth continues during this incubation phase due to the presence of a γ-cystathionine lyase enzyme (CSE) produced by SMCD1 in response to heavy metal toxicity stress.

For PbS particle growth, an aqueous solution of lead acetate (1 mM, Alfa Aesar Puratronic, 99.995% metals basis), L-cysteine (8 mM, Spectrum Chemicals, 99.55%) and Tris-HCl buffer (pH 7.5) was chilled on ice prior to addition of re-suspended SMCD1 cells (OD_{600}=0.5). The solution was kept on ice during growth. Following incubation for 5 mins, the cells were removed by centrifuging the solution at 8000 rpm for a further 5 mins. The supernatant was then collected and kept at 18 °C for a series of prescribed time periods. For CdS shell growth, as grown PbS QDs in the aqueous phase were further concentrated using centrifugation at 12,000 rpm for 10 minutes. The supernatant was discarded and the particles re-suspended in an aqueous solution of L-cysteine (8 mM). Cadmium acetate (1 mM, Alfa-Aesar Puratronic, 99.999% metals basis) and tetramethylammonium hydroxide (5 mM, Alfa Aesar, 98%) were added and the solution was incubated at 37 °C for 18 h.

2.2 Identification of Cystathionine γ-Lyase in Solution

In order to confirm the identity of CSE, a synthesized batch of nanocrystals was dialyzed against DI water for 24 hours, lyophilized and the proteins associated with purified PbS nanocrystals directly identified from dried samples via electrospray ionization mass spectrometry. Both CdS and PbS quantum dots were tested to confirm

the same enzyme is associated with both types of nanocrystals.

2.3 Expression and Purification of Recombinant CSE

A putative form of the *S. maltophilia* CSE identified from the mass spectrometry results was optimized with E. coli codons (Smal_0489 Genscript), subcloned into pET28a (+), and transformed into BL21. The enzyme was then produced using typical expression protocols. In summary, the transformed BL21 cells were subcultured into 200 mL of lysogeny broth with 50 μg/mL Kanamycin antibiotic and grown at 37 °C for 12-24 hours. The BL21 cells were then resuspended in fresh lysogeny broth with 50 μg/mL Kanamycin and 1 mM IPTG to induce expression. The expression was performed at 20 °C for 10 hours. Following expression, the BL21 cells were harvested using centrifugation at 3000 x g, resuspended in lysis buffer (10 mM imidazole, 100 mM HEPES, 500 mM NaCl, 10% glycerol), and sonicated on ice at 12W for 10 seconds on/10 seconds off. The enzyme containing supernatant was separated from cell debris using centrifugation and then purified using immobilized metal affinity chromatography (IMAC). The IMAC column contained Ni-NTA chelating sepharose (GE Healthcare) and the cell lysate was eluted using increasing concentrations of imidazole buffer (20 mM HEPES, 500 mM NaCl, 10% glycerol, and 10-500 mM imidazole). CSE was stored in imidazole buffer until use.

2.4 Single Enzyme Biomineralization of CdS Quantum Dots using CSE

CdS quantum dots were synthesized by the single enzyme cystathione γ-lyase (CSE) as previously reported. [36] In summary, CSE was overexpressed using recombinant *E. coli* and purified using ionic metal affinity chromatography (IMAC). Quantum dot synthesis was initiated by combining 1 mM Cd acetate (Alfa Aesar,99.999% Puratronic), 8 mM L-cysteine, and 0.05 mg/mL CSE in 0.1 M Tris-HCl (pH 9). The solutions were incubated at 37 °C for 4-5 hours until an absorbance peak of 380 nm was obtained. Following growth, the CdS quantum dot solutions were subjected to purification to remove any unreacted cadmium acetate from solution. Purification was performed by either dialysis (Snakeskin, MWCO 3500 kDa) against 2 mM L-cysteine in 0.05 M Tris-HCl (pH 9) to retain colloidal stability, or by several successive rounds of centrifuge filtering and resuspension in 2 mM L-cysteine, 0.05 M Tris-HCl (pH 9).

2.5 Single Enzyme Biomineralization of $CuInS_2$ Quantum Dots using CSE

$CuInS_2$ quantum dot were synthesized using a two-part incubation process. First, indium nitrate (4 mM, Alfa Aesar Puratronic), L-cysteine (16 mM, Spectrum Chemicals, 99.55%), and CSE (0.1 mg/mL) in Tris-HCl buffer (0.1 M, pH 7.5) were incubated for 2-6 hours at 37 °C. After verifying the presence of a 290 nm peak in the absorbance spectrum, which indicates the formation of <1 nm In-S^{2-} clusters, copper acetate (2 mM, Alfa Aesar Puratronic, 99.99%) was added to solution. The

solution immediately turned yellow, orange, or red, depending on the size of the nanocrystals formed in solution. Some samples were grown with glutathione (10 mM, Spectrum Chemicals) from the initial incubation of indium, cysteine, and CSE to improve nanocrystal stability.

Subsequent ZnS shell growth was performed by adding zinc acetate (2 or 4 mM, Alfa Aesar Puratronic) to the unpurified $CuInS_2$ solution after 1 hour of incubation at room temperature. The solutions were then left to incubate at room temperature for 1-16 hours.

2.6 Phase Transfer of Biomineralized Nanocrystals to the Organic Phase

Phase transfer of the as-prepared quantum dots from aqueous to organic solvents was performed following the procedure developed by Gaponik et al.[4] 5 mL of aqueous quantum dot solution was placed in a glass vial, followed by addition of 5 mL 1-dodecanethiol (DDT) and then 5 mL acetone. The mixture was then vigorously agitated for 15 mins at 60 °C. After phase transfer, the organic phase was withdrawn and mixed with an equal volume of toluene. Finally, the DDT capped nanocrystals were precipitated with methanol and then resuspended in chloroform or tetrachloroethylene for subsequent optical absorption and fluorescence measurements.

2.7 Chemical synthesis of CdS

A solution of cadmium acetate (1 mM, Sigma-Adlrich, 99.999% metals basis) and L-cysteine (8 mM, Spectrum Chemicals) in Tris buffer (0.1 M, pH 7.5, VWR) was placed into a 4 mL cuvette with a stir bar. NaHS was then quickly pipetted into the cuvette while stirring and allowed to react for 1 minute before removing from the stir plate for measurement. Incubation of the solution was performed in an incubator at 37 °C with shaking to ensure even mixing. The titration experiments were performed as above with a few minor changes: the NaHS was added in 2 μM increments with 1 minute of stirring between each addition. The solutions were kept at room temperature throughout the experiment. UV-vis measurements were recorded after the addition of every 10 μuM NaHS.

2.8 Graphene Oxide Synthesis

Graphene oxide was synthesized using the modified Hummers method.[37] Briefly, 20 g of graphite powder (Carbon Bay) was first preoxidized by mixing with a solution of 30 mL sulfuric acid (BDH, 96%), 10 g potassium peroxisulfate (Alfa Aesar, 99%), and 10 g phosphorous pentoxide (Alfa Aesar, 99.99%) preheated to 80 °C. The solution was then slowly cooled to room temperature over 6 hours. The resulting preoxidized graphite was then diluted, filtered and washed with DI water until the rinse water reached a neutral pH. Oxidation was performed by adding the rinsed graphite powder to a 460 mL solution of sulfuric acid cooled to 4°C. Then, 60 g of potassium permanganate (Alfa Aesar, 99.0%) was slowly added so that the temperature of the solution

remained below 25°C. The solution was then heated to 35 °C for 2 hours before dilution with 920 mL DI water. After 15 more minutes, the reaction was stopped by adding an additional 2.8 L of DI water and 50 mL of hydrogen peroxide (BDH, 30%). The resulting graphene oxide was filtered and washed with 5 liters of a 10% hydrogen chloride solution (BDH, 37.6%) before being resuspended to a final concentration of 2 g/L. The GO was further purified by dialysis (Snakeskin, MWCO 3500 kDa) and several iterations of centrifuge washing to completely remove any remaining acid.

2.9 Functionalization of GO by Poly-L-lysine and Reduction via CSE

In order to facilitate the loading of CdS QDs, GO was functionalized with the linker molecule poly-L-lysine (PLL, MW 30,000-50,000, Alfa Aesar) prior to reduction by L-cysteine (Spectrum Chemicals, 99.7%) and CSE. Briefly, 0.5 g/L of purified GO was sonicated on ice for 15 minutes. Then, 8 mg of PLL were added to a 10 mL solution of GO (0.2 g/L) in 0.1 M Tris buffer (pH 9, VWR, 99.5%) and heated at 37 °C for 2 hours. Next, either 10 mM L-cysteine or 10 mM L-cysteine and 0.4 mg/mL CSE were added to the GO-PLL solution and incubated for up to 48 hours. The partially reduced graphene oxide functionalized by PLL (rGO_{PLL}) was then purified by several rounds of centrifuging and resuspension in DI water to remove excess PLL from solution.

2.10 Functionalization of GO by Poly-L-Lysine and Reduction via $NaBH_4$

In order to facilitate the loading of CdS QDs, GO was functionalized with the linker molecule poly-l-lysine (PLL, MW 30,000-50,000, Alfa Aesar) prior to reduction by sodium borohydride (Sigma Aldrich) following the procedure of Shan et al.[1] Briefly, 0.5 g/L of purified GO was sonicated on ice for 15 minutes. Then, 8 mg of PLL and 10 mg of potassium hydroxide (Alfa Aesar) were added to a 10 mL solution of GO (0.2 g/L) and heated at 70 °C for 24 hours. Next, 1 mL of 1 M sodium borohydride was added and the solution was heated at 70 °C for an additional 2 hours. The partially reduced graphene functionalized by PLL (rGO_{PLL}) was then purified by several rounds of centrifuging and resuspension in DI water to remove excess PLL from solution.

2.11 Material Characterization Techniques

Optical absorbance measurements were performed using a Shimadzu UV-vis 2600 spectrophotometer equipped with an ISR-2600-Plus integrating sphere attachment. Photoluminescence spectra were acquired with a QuantaMaster 400 (Photon Technology International) in the visible range and a Horiba Fluorolog-3 equipped with a liquid nitrogen cooled InGaAs detector in the near infrared range. Photoluminescence lifetime measurements were obtained using Horiba Fluorometer. To inhibit further nanocrystal growth during aqueous photoluminescence measurements, each sample was chilled on ice for 2 mins and the temperature controller was set to 5 °C. Quantum yields (QYs) for $CuInS_2$ quantum dots were measured using the standard

reference dye Coumurin 153 with a QY of 0.5336. QYs for PbS quantum dots were determined using the reference dye IR-26 in 1,2-dichloroethane.[38]

FTIR spectra were acquired using a Thermo Nicolet iS50 infrared spectrometer equipped with a Mercury-Cadmium-Tellurium (MCT) liquid nitrogen cooled detector was used with a Harrick Praying Mantis diffuse reflection accessory and ZnSe windows. All spectra were averaged over 96 scans at a resolution of 4 cm^{-1}. Raman spectra were obtained using an Alpha300RA confocal Raman microscope equipped with a 532 nm laser and UHTS 400NIR spectrometer with a diffraction grating of 2400 lines/mm (Witec). Powder XRD measurements were performed on precipitated, dried quantum dots using Cu Kα (1.5418 $\mathring{A}$) radiation in a Rigaku Miniflex II diffractometer.

Samples used for transmission electron microscopy analysis were used as is, or in the case of rGO-CdS composites, first purified by centrifuging and resuspending in DI water to remove any unbound quantum dots. Samples suitable for electron microscopy analysis were obtained by drop-casting diluted quantum dot solutions onto a holey carbon coated grid and allowing the solvent to evaporate. The samples were analyzed at 200 kV in an aberration corrected JEOL ARM 200CF analytical electron microscope equipped with a JEOL Centurio XEDS system.

2.12 Solar Cell Fabrication

Solar cell structures were fabricated on fluorine doped tin oxide (FTO) coated glass slides (Sigma Aldrich, 7 Ω/sq) that were cleaned by a three stage process. Firstly, by sonication in a 50:50 ethanol-to-acetone mixture, secondly, by sonication in a 1:10 Contrad 70 soap to DI water solution, and finally, by sonication in 200 proof ethanol.

The cleaned FTO substrates were then rinsed with 200 proof ethanol and blown dry with N_2. A TiO_2 blocking layer was then deposited using a modified convective deposition method described below.[39] The cleaned FTO substrate was held horizontally and placed in contact with an inclined glass microscope slide touching at a 45° angle. The lower side of the inclined glass slide was rendered hydrophobic using parafilm. Next, 15 μL of a titanium (IV) butoxide precursor solution was placed in the wedge formed between the FTO and glass slide, and the substrate was pushed using a linear motor in order to spread the solution uniformly across the FTO slide. After deposition, the material was annealed at 500 °C for 3 hours to form the TiO_2 blocking layer. Following this, a macroporous TiO_2 layer was deposited onto a 1 cm^2 area of the FTO with TiO_2 blocking layer using an opaque titania paste (Sigma Aldrich) applied with the doctor blade method and then annealed at 500 °C for 1.5 h. The PbS or PbS-CdS quantum dots were deposited onto the TiO_2 electrode by a sequence of 20 drop-casting/drying steps of the organic colloidal solutions. A gold anode was deposited by the doctor blade technique on a cleaned FTO surface and annealed at 200 °C for 1 h. The solar cell structures were completed by sandwiching 15 μL of 0.5 M polysulfide electrolyte [40] between the TiO_2-quantum dot substrate and the anode using a parafilm spacer. The current density-voltage (J-V) characteristics of the solar cell were measured using a Gamry instruments electrochemical workstation operating under AM 1.5 (100 mW/cm^2) illumination conditions created by an ABET Technologies (Model No. 10500) solar simulator.

2.13 Bioimaging of THP-1 cells

Bioconjugates of quantum dots were formed using EDC and NHS crosslinkers. Prior to performing the conjugation, the quantum dots underwent buffer exchange from Tris-HCl to phosphate buffered saline (PBS) using successive concentration and re-suspension via centrifugation filters (9K, Thermo Fisher Scientific). The EDC solution was prepared immediately prior to use to prevent hydrolysis. 10 μL of an EDC solution (20 mg/mL, Thermo Fisher Scientific) and 1 μL of NHS (20 mg/mL, Thermo Fisher Scientific) were added to 100 μL of a concentrated $CuInS_2$/ZnS quantum dot solution. The solutions were briefly centrifuged to remove any precipitated nanocrystals and then 100 μL of 151-IgG was added to the solution. 151-IgG or 151-8 AE4 was deposited to the DSHB by Hubbard, A. (DSHB Hybridoma Product 151-IgG or 151-8 AE4). The solutions were then incubated for 1 hr at 37 °C. THP-1 cells were maintained at 37 °C under 5% CO_2 in RPMI 1640 medium containing 10% FBS. THP-1 cells were deposited onto ibiTreat μ-Dishes (Ibidi, Martinsried, Germany), treated with poly-L-lysine. These cells were then incubated with 50 μL of quantum dot antibody mixture and incubated at 37 °C for 3 hours. The μ-Dish, containing the THP-1 cells and quantum dot antibody mixture, was imaged using a Nikon C2si+ confocal microscope equipped with a LU-N4S laser unit and a 40× air objective (NA = 0.95). The images were processed using Elements version 4.3, Nikons imaging software suite, and Fiji. The cells were then washed twice with PBS buffer prior to imaging. To check for cell viability in the presence of quantum dots, THP-1 cells were incubated with 50 μL of the quantum dot antibody mixture and were maintained at 37 °C under 5% CO_2 in RPMI 1640 medium containing 10% FBS. Over a period of 6 hours, cell viability was measured every 20 minutes using a Trypan blue assay. Cell

viability remained around 95-99% over the entire time period.

2.14 Preparation and testing of CdS-rGO photocatalysts

Conjugation of CdS QDs and rGO_{PLL} was achieved by mixing various concentrations of purified CdS QDs and rGO_{PLL} solution to a final volume of 80 mL and allowing them to incubate for 1 hour at room temperature. Prior to initiating the photoreaction, the as-prepared photocatalyst was degassed under vacuum for 1 hour in a 100 mL round bottom flask while stirring vigorously. Following the degas step, the remaining head space was purged with N_2 for 15 minutes to ensure no oxygen was present within the reactor. The reactor was then sealed shut and positioned 20 cm away from a 350 W Xenon lamp with a >420 nm UV cut-off filter. A 0.4 mL gas sample was obtained every hour through a septum and analyzed for hydrogen and oxygen content by an in-line model 8610C gas chromatograph (SRI Instruments) equipped with thermal conductivity and flame ionization detector.

Chapter 3

Biomineralization of PbS and PbS-CdS Core-Shell Nanocrystals and their Application in Quantum Dot Sensitized Solar Cells

3.1 Introduction

Previously, we demonstrated the ability of *S. maltophilia* to synthesize size controlled CdS nanocrystals.[35] This chapter illustrates the generality of our method by showing that the same strain of *S. maltophilia* can be used to produce PbS nanocrystals without any further evolution. In addition, we are able to synthesize PbS-CdS core-shell structures using this low temperature biosynthetic route without having to resort to using a conventional chemical route to deposit the shell material.

PbS nanocrystal quantum dots have a relatively large Bohr radius (18-20 nm)[41] with an easily accessible quantum confinement region, which makes them highly interesting for energy harvesting applications. The strong quantum confinement effects displayed by sub-20 nm PbS particles leads to highly tunable band-gap energies that can be several times greater than that of the bulk PbS material (0.41 eV). This tunable band gap, when coupled with the smaller intrinsic line width exhibited by nanocrystals significantly below the Bohr radius, can lead to enhancements in non-linear optical properties.[41, 42] Such PbS nanocrystals are an ideal candidate for use in quantum dot sensitized solar cells as they can be designed to absorb in the near infrared, optimally harvesting light in the peak region of the solar spectral range.[43] Additionally, PbS quantum dots are potential multi-exciton generators [44, 45] which can be used to further improve solar cell efficiency by breaking the Shockley-Queisser limit.[46] Core-shell morphology PbS-CdS nanocrystals are also of interest due to the further enhancement of the non-linear optical properties they offer when compared with the basic PbS core materials. For example, Neo *et al* demonstrated a significant increase in free-carrier absorption upon growth of a CdS shell on PbS QD cores in materials prepared by conventional methods.[47] Within a quantum dot sensitized solar cell environment the PbS-CdS core-shell morphology was found to lead to an increased electron lifetime, a decreased electron transit time and an increased photostability through passivation of PbS surface defects. [48]

3.2 Results and Discussion

Strain SMCD1 was originally evolved to produce CdS nanocrystals from aqueous solutions of Cd acetate, L-cysteine in M9 minimal media at 37 °C.[35] Replacing cadmium acetate in this preparation with lead acetate under the same concentration and temperature conditions leads to formation of an opaque brown solution within 20 minutes. XRD analysis of the centrifuged and dried solid after 3 hours of growth, Figure 3.1 a), shows a diffraction pattern consistent with the cubic rock salt phase of PbS (JCPDS #5-592). This precipitate is only formed in a buffered aqueous solution in the presence of strain SMCD1, lead acetate, and L-cysteine. Removal of any of these components, including utilizing unbuffered de-ionized water, does not lead to the formation of a brown precipitate. The solutions without all components present appear turbid due to the optical density of the cell suspension (Figure 3.1 b). The solution that does not contain L-cysteine is more opaque due to the formation of a white precipitate, most likely $Pb(OH)_2$, which forms due to the absence of L-cysteine as the metal complexing agent. Note that the cells were not centrifuged from any of these samples shown in Figure 3.1 b) during PbS growth.

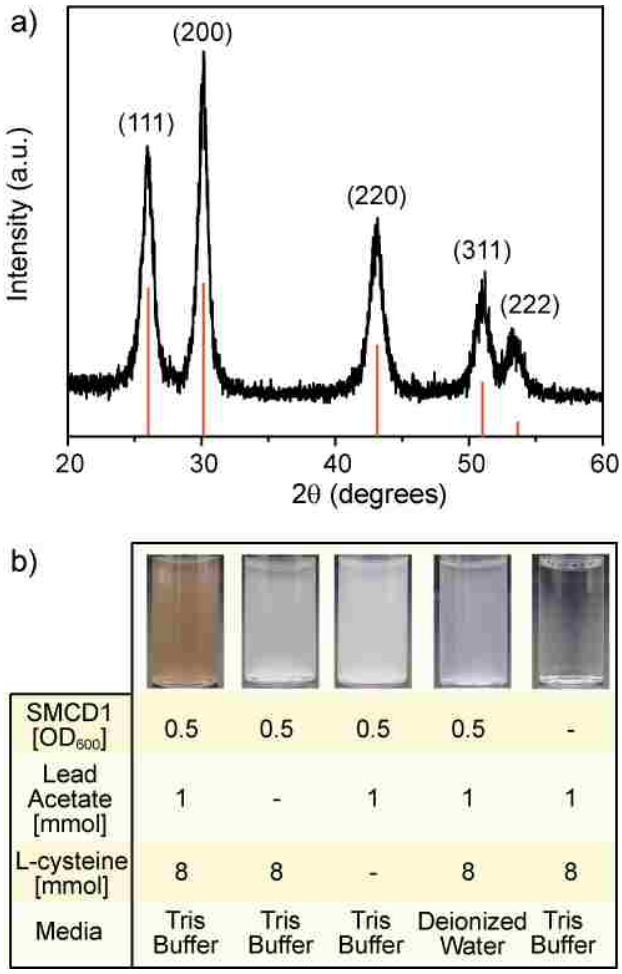

Figure 3.1: a) X-ray diffraction pattern obtained from the brown precipitate formed after 3 hours at 37 °C in a tris buffered (pH 7.5) aqueous solution of lead acetate, L-cysteine, and strain SMCD1. b) Matrix of reaction ingredients and the corresponding photographs of solutions containing all components and those with one component deliberately missing.

The ability of the same strain of *S. maltophilia* to independently produce both CdS and PbS nanocrystals clearly demonstrates its flexibility in synthesizing various metal sulfide quantum dots. SMCD1 is therefore facilitating biomineralization of PbS from solution in an analogous manner to that described in our previous reports of CdS biomineralization. This observation is consistent with the known heavy metal tolerance of *S. maltophilia*.[24]

The driving mechanism underlying this mineralization process is most likely through the expression of a putative cystathionine γ-lyase (smCSE) previously found to be associated with the extracellular biomineralization of CdS quantum dot nanocrystals from SMCD1.[35] Cystathionine γ-lyases are a class of enzymes that catalyze the production of H_2S, NH_3 and pyruvate from L-cysteine; we propose that the reactive H_2S thus generated leads to the mineralization of PbS. This concept of enzymatic generation of reactive sulfur has been suggested in a number of prior studies focused on CdS biomineralization, typically utilizing endogenous levels of sulfur-containing biomolecules present in the cells.[23, 49, 50, 28, 51] In the present case, the addition of excess L-cysteine beyond endogenous levels provides both an abundant sulfur source and a useful nanoparticle capping agent.[40, 52, 53, 54, 55, 56]

The calculated crystallite size by the Scherrer equation for the data in Figure 3.1 is 7 nm. Modification of the synthesis procedure was necessary in order to access the strong quantum confined size range with optical properties in the desirable near-IR range.[57] Building on the hypothesis that biomineralization occurs via a cystathionine γ-lyase catalyzed H_2S generation from L-cysteine, and noting prior literature demonstrating that a decreased supply rate of H_2S results in a decrease in average

PbS crystallite size during chemical synthesis [58], the biomineralization rate was deliberately lowered by reducing the rate of H_2S generation. To achieve this goal, the solution was placed on ice during initial nanocrystal nucleation and the SMCD1 cells centrifuged from solution after 5 minutes of growth time. The aqueous centrifuged supernatant was buffered at pH 7.5 and contained residual lead acetate, L-cysteine and enzyme produced by the cells during the first 5 min of growth; removal of the cells was implemented to halt production of additional enzyme and thus limit growth rate. The temperature for subsequent nanocrystal growth in the centrifuge supernatant was carefully controlled at 18 °C for a variety of time periods. The presence of the expected cystathionine γ-lyase associated with the PbS nanocrystals was indeed confirmed by electrospray ionization mass spectrometry (Figure 3.8).

Figure 3.2 shows a systematic series of photoluminescence spectra obtained from the aqueous solution at various incubation time intervals between 15 and 95 minutes following centrifugation and removal of the cells. The apparent photoluminescence peak is seen to red-shift with increasing incubation time from 1040 nm after 15 mins to 1135 nm after 95 mins. It should be noted, however, that the true maximum of the fluorescence peak is obscured due to the overlapping absorption profile of water in this region, as indicated by the dotted line in Figure 3.2. This unfortunate overlap combined with the low concentration of PbS nanocrystals present inhibited our ability to collect the corresponding absorption spectral data as a function of incubation time. The peak luminescence positions and red-shift with increasing incubation time are however entirely consistent with those expected for a gradual increase in the average size of quantum confined PbS nanocrystals with increasing growth time.[41, 59, 60] The bulk direct band gap for PbS is 0.41 eV (3024 nm) and the excitonic

Bohr radius is 18 nm, and reports suggest that strong quantum confinement effects should occur for particles below 8 nm in diameter.[59] While we cannot determine the absorption positions to obtain the direct bandgap, calculating a band gap and thus nanocrystallite size from the photoluminescence peak wavelengths of 1040 nm (1.2 eV) and 1135 nm (1.1 eV) leads to maximum mean particle diameters of ∼3.5 and ∼4.0 nm, respectively.

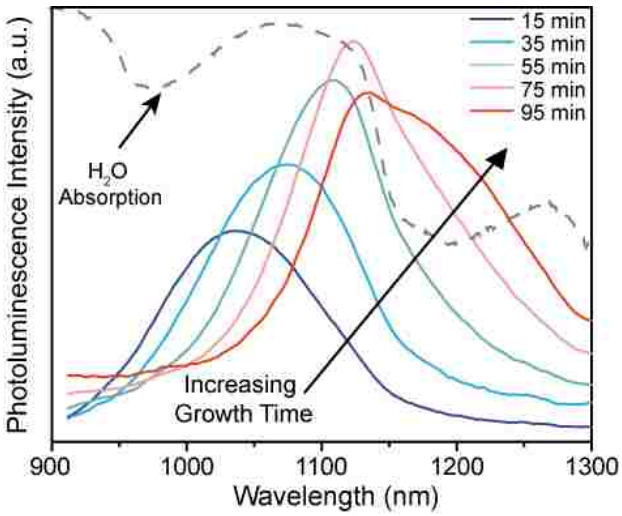

Figure 3.2: Photoluminescence spectra obtained from the aqueous PbS nanocrystal solution as a function of incubation time at 18 °C. The observed red-shift of the peak maxima with increasing incubation time is consistent with a gradual increase in average nanocrystallite size within the quantum confined range. The dotted line indicates the expected absorption profile for water.

The required time (<60 min) for our PbS nanoparticle formation is substantially faster than any other report of PbS biomineralization which typically take 24 to 48 hours at physiological temperature.[61, 62, 63] This is because these prior studies relied solely on utilizing the natural abundance of reactive sulfur generated in the cell in response to Pb exposure. In contrast, in our work the engineered bacterial strain SMCD1 expresses a putative cystathionine γ-lyase enzyme in response to exposure to

the heavy metals present in solution. This cystathionine γ-lyase enzyme then actively catalyzes H_2S production from the excess L-cysteine added to the solution, leading to a much more rapid biomineralization response.

In order to measure the absorption spectrum, the PbS nanocrystals grown in the aqueous phase for 30 mins were phase transferred into chloroform with 1-dodecanethiol as capping agent using the method described by Gaponik et *al.*[5] The resulting absorption and photoluminescence spectra, now free of water absorption artefacts, are shown in Figure 3.3, and have maxima at 910 nm and 1080 nm, respectively, which are fully consistent with that expected for quantum confined PbS nanocrystals of $\sim$3.0 nm in size.[41, 59, 60] The measured full-width-at-half-maximum (FWHM) for the photoluminescence peak from our biomineralized PbS nanocrystals is 144 nm. This FWHM value is consistent with previous reports of biotemplated synthesis of PbS QDs.[64] For example, Levina *et al* report a photoluminescence peak with FWHM of 135 nm at 1060 nm, corresponding to 4 nm QDs.[65] In the absence of any size-selective precipitation steps, PbS QD chemical synthesis in the organic phase typically lead to a FWHM of $\sim$100 nm.[66, 67] As with other QD materials, post-synthesis size selective precipitation, which has not been attempted in our case, can significantly narrow the particle size distribution and further improve the FWHM for photoluminescence.

The quantum yield (QY) of the PbS nanocrystals transferred to the organic phase and capped with DDT varied with synthesis batch between 16 and 45%. This batch-to-batch variation and the range of quantum yield is in agreement with previous reports for QDs synthesized from chemically reactive precursors through traditional high temperature approaches, where typical reported QY values range from 20% to 80%.[60, 66, 67, 68, 16, 69] To the best of our knowledge ours is the highest reported

QY for any biomineralized PbS quantum dots. There are two previous reports of QY values for bio-templated materials that are particularly relevant to the current study. Firstly, Ma *et al* reported a QY value of 3.6% when utilizing luciferase to template the chemical reaction between bound Pb^{2+} and Na_2S.[64] Secondly, Levina *et al* reported a QY value of 11.5% when using a DNA template and reactive precursors comprising Pb^{2+} and Na_2S.[65]

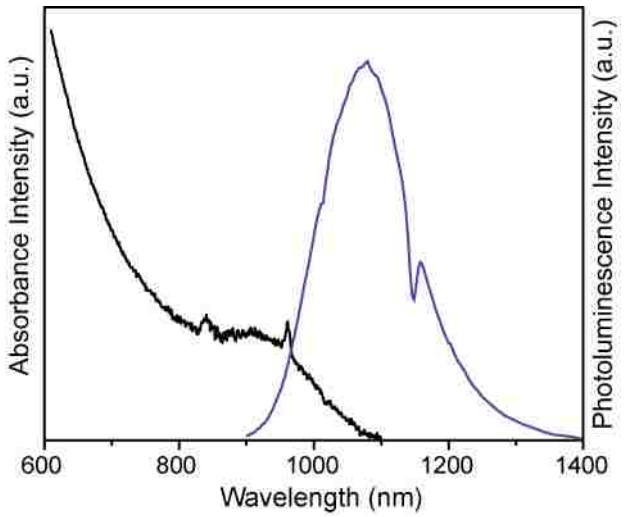

Figure 3.3: Absorbance and corresponding photoluminescence spectra of biomineralized PbS nanocrystals grown in the aqueous phase for 30 min following ligand and phase transfer into chloroform. The sharp peaks in the absorbance spectrum (black line) at 820 and 980 nm are artefacts from the instrument detector switch and 1-dodecanethiol (DDT) ligands, respectively. The dip in the photoluminescence spectrum (blue line) at 1150 nm is due to absorbance from chloroform.

The formation of quantum confined PbS nanocrystals by the biomineralization route has been confirmed by STEM high-angle annular dark field (HAADF) imaging and X-ray energy dispersive spectroscopy (XEDS) of phase transferred materials. Figure 3.4 shows representative electron microscopy data collected from nanocrystals grown for 30 minutes; namely the same material for which optical characterization

data are presented in Figure 3.3. The PbS nanoparticles are crystalline in nature, exhibiting lattice spacings and interplanar angles consistent with the rock salt structure of PbS (Figures 3.4 a) & c), b) & d) and Table 3.1). The nanocrystals have a somewhat irregular shape and are typically around 4.0-4.5 nm in diameter. This is consistent with the PbS particle size deduced from analysis of the optical properties shown in Figure 3.3. The XEDS spectrum obtained on a single nanocrystal, Figure 3.4 e), confirms the presence of both Pb and S atoms in the particles. Both the M and L families of Pb are identified due to the overlap of the Pb M_α and S K_α peak energies.

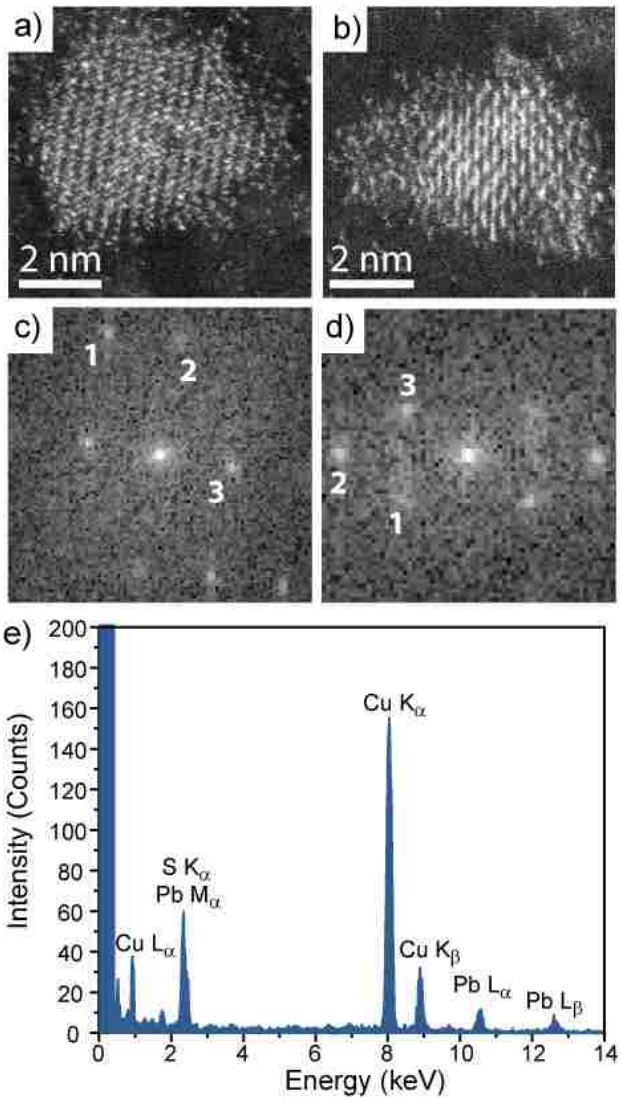

Figure 3.4: a, b) HAADF-STEM images and c, d) corresponding FFT of 4.5 nm and 4.0 nm PbS nanocrystals viewed along the $[11\bar{2}]$ and $[11\bar{0}]$ projections respectively. Lattice fitting of indicated planes is reported in Table 3.1. e) Representative XEDS spectra acquired from a single biomineralized PbS nanocrystal (30 minutes incubation time at 18 °C) showing the co-existence of both Pb and S.

Having established a mechanistic similarity between biomineralization of PbS and CdS QDs using *S. maltophilia* [35], we attempted to grow a thin CdS shell on the PbS nanocrystal core by a sequential biomineralization process. Specifically, biomineralized PbS cores grown for 30 minutes were concentrated by high speed centrifugation and the supernatant was discarded. The PbS nanocrystals were then re-suspended in a pH 7.5 solution of L-cysteine and cadmium acetate. The solution was then incubated at 37 °C for 18 hours. The photoluminescence peak of the resultant PbS-CdS colloidal material shows a progressive blue-shift during this period, which is in good agreement with the expected shift in optical properties induced by the progressive growth of a thin CdS shell on the PbS cores (Figure 3.9).[47, 70] No SMCD1 cells were added in this process, instead CdS biomineralization is catalyzed solely by the residual cystathionine γ-lyase enzyme associated with the PbS nanocrystals after centrifugation. No CdS mineralization can occur in the absence of enzyme.[35] Hence, the low concentration of cystathionine γ-lyase present in this sequential growth step leads to slow CdS biomineralization ensuring that only a thin CdS shell is formed on the PbS core at the expense of a relatively long growth period.

Figure 3.5 a) shows the photoluminescence spectra of both the original PbS nanocrystals and the PbS-CdS core-shell nanocrystals after 18 hours of incubation in the cadmium acetate solution and then phase transfer into an organic solvent. The observed blue-shift in photoluminescence is characteristic of CdS shell growth on a PbS core [47, 16, 71], implying that CdS biomineralization has occurred on the PbS nanocrystals. The magnitude of the blue-shift is 100 nm, which is indicative of a CdS shell that is 0.4 nm thick [71], and corresponds to only one or two CdS layers. The corresponding absorbance spectrum for the same PbS-CdS particles is displayed

alongside the photoluminescence spectrum in Figure 3.5 b). Again, the observed blue-shift in both absorbance and photoluminescence peak positions relative to pure PbS QDs are consistent with the growth of an ultra-thin CdS shell on the PbS core. The measured quantum yield for the PbS-CdS core-shell nanocrystals was 9%. This reduction in QY compared with the parent PbS cores is likely due to the use of DDT capping agent which is well known to quench emission from CdS QDs.[72]

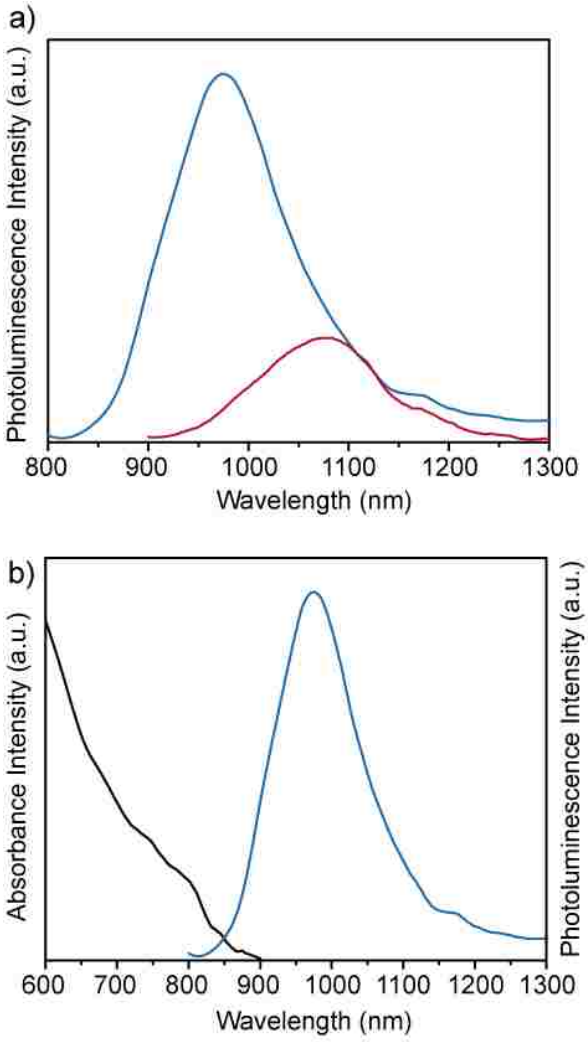

Figure 3.5: a) Photoluminescence spectra of biomineralized PbS (red line) and biomineralized PbS-CdS (blue line) core/shell nanocrystals. b) Absorbance (black line) and photoluminescence (blue line) spectra of the PbS-CdS core-shell nanocrystals. The above samples were phase transferred into chloroform for optical characterization.

Figure 3.6 shows both HAADF-STEM imaging data and XEDS compositional analysis from PbS-CdS morphology nanocrystals. No clearly defined crystalline CdS shells were detected in the HAADF-STEM images (Figs 3.6 a, b), which is not entirely unexpected since CdS is not isostructural with the PbS core. Instead, a disordered surface layer about 0.5 nm thick was frequently observed covering the original 3.0-4.0 nm PbS cores. The interior regions of the PbS-CdS particles maintain their original crystalline nature and display lattice spacings and interplanar angles that are fully consistent with the PbS rock salt structure (Figures 3.6 b) & c) and Table 3.2). To confirm that the change in optical properties is due to the formation of a CdS shell, an XEDS spectrum was collected from a single isolated nanoparticle (Figure 3.6 d)). This clearly demonstrates that Pb, Cd and S are all present in individual particles. Attempts to perform XEDS line-scans on individual core-shell particles were unsuccessful, even when utilizing a state-of-the-art JEOL ARM 200CF aberration corrected STEM equipped with a Centurio XEDS silicon drift detector, due to the small size of the particles and their electron beam sensitivity.

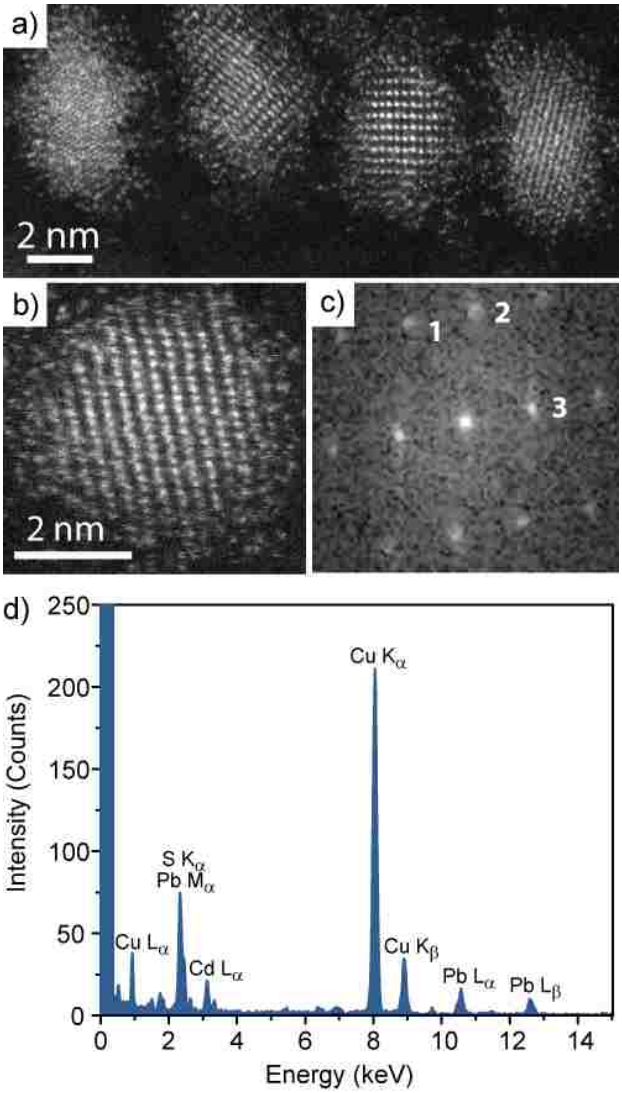

Figure 3.6: a) HAADF-STEM image of several typical biomineralized PbS-CdS core-shell nanoparticles; b) HAADF-STEM image and c) corresponding fast Fourier transform (FFT) from an individual core-shell morphology particle viewed along the [031] PbS zone axis (detailed fringe fitting is presented in Table 3.2); d) XEDS spectrum collected from a single PbS-CdS nanocrystal, confirming the co-existence of both Pb and Cd cations in the nanocrystal.

There are other possible explanations for the blue-shift noted in the optical properties for the PbS-CdS particles. For instance, a decrease in PbS core particle size by ∼0.8 nm would generate a blue-shift of ∼150 nm. However, the consistent size of the PbS seed particles with and without the CdS overlayer as noted from the HAADF-STEM images indicate that this is not the case. Another possibility is the formation of a $Pb_{1-x}Cd_xS$ solid solution via interdiffusion of the two cations within a particle during synthesis. The rapid and progressive blue-shift noted with increasing incubation time (Figure 3.8) indicates that such interdiffusion would have to occur very quickly at the growth temperature, which in our case is only 37 °C. We also note from other reports that chemical synthesis of CdS shells on PbS nanoparticles which are typically performed at significantly higher temperatures (i.e. 100 °C or higher) can apparently generate PbS-CdS core-shell morphology particles without any significant cation interdiffusion.[47, 48, 16, 73] Hence we conclude that the blue-shift modification to optical properties noted in our case arises from the production of PbS-CdS core-shell morphology particles rather than by size erosion of the PbS cores or by $Pb_{1-x}Cd_xS$ alloy formation.

While thicker, typically >2 nm, shells can be directly imaged [71, 74] or detected as slight peak shifts in powder XRD patterns [47], evidence for ultra-thin shells relies on detecting shifts in optical properties analogous to those reported here [75, 18]. Thus we cannot with absolute certainty rule out the possibility that CdS shell growth may, in part, occur via the well-known cation exchange reaction.[71, 76, 77, 78, 79] Pietryga *et al* demonstrated that cation exchange between Pb and Cd in the organic phase would result in a 50 nm blue-shift at room temperature, which is consistent with our data.[18] This issue is complicated by the presence of the enzyme which we

have previously shown to be capable of biomineralizing CdS. We have attempted to remove residual enzyme by utilizing typical enzyme denaturing agents (Protease K, SDS, and ethanol), however the addition of these agents leads to quenching of luminescence from the QDs. Evidence for aqueous phase active enzyme-driven CdS shell biomineralization comes from the previously demonstrated CdS biomineralization activity of this class of enzymes in solution and the presence of a small population of pure CdS nanocrystals in the PbS-CdS core-shell solution, as noted in Figure 3.10.

The functionality of our biomineralized PbS and PbS-CdS core-shell quantum dots has been demonstrated in a practical manner by incorporating these nanocrystals into a simple quantum dot sensitized solar cell structure. The current density/voltage (J/V) characteristics of the solar cells containing these two nanoparticle types are compared in Figure 3.7. The pure PbS quantum dots yield an open circuit potential, V_{OC}, of 0.43 V, whereas the PbS-CdS core-shell quantum dots improve the V_{OC} to 0.59 V. The V_{OC} values are entirely consistent with previous reports for chemically synthesized PbS-CdS core-shell quantum dot sensitized solar cells.[80, 70, 81] The measured increase in V_{OC} is thought to result from passivation of PbS surface defects by growth of the CdS shell.[70] There could also be a slight change due to the blue-shift in band-gap of the PbS-CdS core-shell particles.[80] Fill factors for the PbS and PbS-CdS core-shell quantum dot solar cells' J-V curves shown were 0.50 and 0.45 respectively. It should be noted that the structure of our solar cell devices has not been optimized and the performance difference highlighted here merely serves to (i) illustrate the difference between the biomineralized PbS and PbS-CdS core shell nanocrystals and (ii) demonstrate the potential for using these biomineralized quantum dots in real device applications.

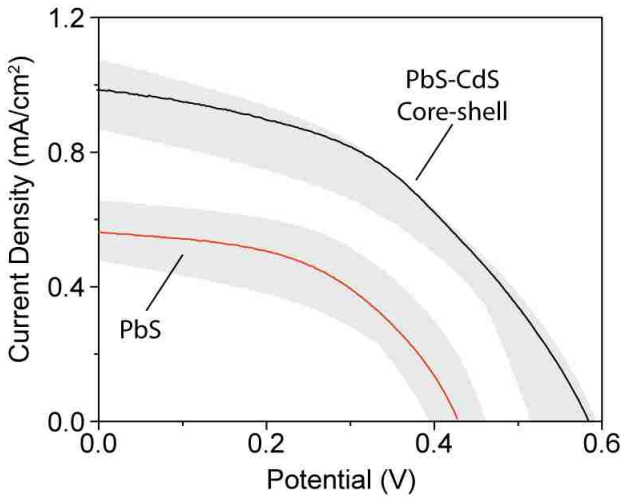

Figure 3.7: Current density as a function of cell potential of biomineralized PbS and PbS-CdS core shell quantum dot nanocrystal sensitized solar cells under AM1.5 illumination. The shaded region represents the reproducibility range achieved between four cells of each type.

3.3 Conclusions

We have demonstrated both a biomineralization route to PbS and PbS-CdS core shell quantum confined nanocrystals and their application in quantum dot sensitized solar cells. Biomineralization is facilitated by the extracellular production of a cystathionine γ-lyase by an engineered strain of *S. maltophilia* with the resulting nanocrystal size controlled through the growth time and temperature. Biomineralized PbS nanocrystals form with the rock-salt structure and demonstrate optoelectronic properties consistent with their size and prior reports of the band gap increase upon PbS quantum confinement. A CdS shell can be biomineralized on the PbS core by addition of cadmium acetate and L-cysteine to the PbS nanocrystals. The resulting quantum dots are amenable to facile phase transfer to an organic phase and lead to enhanced open circuit potential and current density in a quantum dot sensitized solar cells.

3.4 Supplementary Information

The following information is provided as supplementary information for the results presented in Section 3.2.

```
MSNATSQDRA LALATLAIHG GQSPDPSTGA VMPPIYATST YAQSSPGEHQ GFEYSRTHNP
TRFAYERCVA SLEGGTRGFA FASGMAASST VIELLDAGSH VVAMDDIYGG SFRLFERVRR
RTAGLDFSFV DLTDLAAFEA SITPKTKMVW IETPTNPMLK IVDIAAVAAI AKRHGLIVVV
DNTFASPMLQ RPLELGADLV LHSATKYLNG HSDMVGGMVV VGDNAELAEQ MAFLQNSVGG
VQGPFDSFLA LRGLKTLPLR MKAHCANALA LAQWLEKHPA VEKVIYPGLA SHPQHELAGK
QMAGYGGIVS IVLKGGFDAA KRFCEKTELF TLAESLGGVE SLVNHPAVMT HASIPVARRE
QLGISDALVR LSVGVEDLGD LQVDLGEALK
```

Figure 3.8: Sequence of the cystathionine γ-lyase that was derived from electrospray ionization mass spectrometry of a PbS QD solution synthesized using the *Stenotrophomonas maltophilia* strain SMCD1 (NCBI accession number WP 012509966). The QD containing supernatant was dialyzed against distilled water to reduce the free Pb salt and L-cysteine concentration, lyophilized and analyzed by electrospray ionization mass spectrometry(ESI-MS).

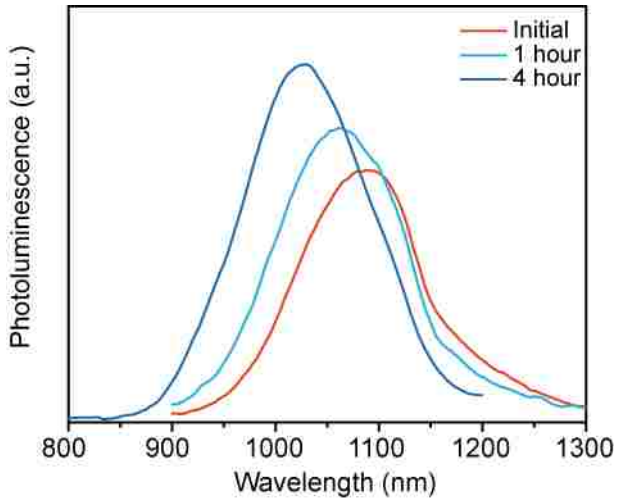

Figure 3.9: Photoluminescence characteristics of PbS-CdS core-shell nanoparticles, demonstrating a clear blue-shift as a function of the time that the PbS seed particles are in contact in the solution containing the Cd-precursor.

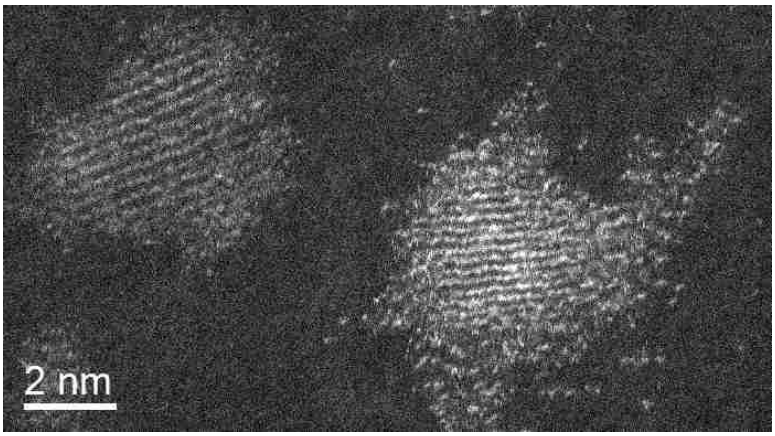

Figure 3.10: HAADF-STEM image of an intentionally grown PbS-CdS core-shell nanocrystal (right) and a pure CdS nanocrystal resulting from a secondary nucleation event (left).

Table 3.1: Lattice fitting of PbS nanocrystals shown in Figure 3.4 a) & c) and 3.4 b) & d) to the rock salt PbS structure. <x,y> denotes the angle between two intersecting planes x and y. Planes are identified in Figure 3.4 c).

Nanocrystal Identification as cubic PbS					
Figure 4a,c): $[1\bar{1}\bar{2}]$ projection			Figure 4b,d): $[1\bar{1}0]$ projection		
	Measurement	Matching		Measurement	Matching
Plane 1	d=1.79 Å	1.91 Å (311)	Plane 1	d=3.43 Å	3.49 Å (111)
Plane 2	d=2.10 Å	2.11 Å (220)	Plane 2	d=2.10 Å	2.13 Å (220)
Plane 3	d=3.43 Å	3.53 Å$(1\bar{1}1)$	Plane 3	d=3.43 Å	3.57 Å $(11\bar{1})$
<1, 2>	31.5°	32.2°	<1, 2>	35.3°	36.0°
<1, 3>	58.5°	57.9°	<1, 3>	70.5°	71.9°
<2, 3>	90.0°	89.9°	<2, 3>	35.3°	35.9°

Table 3.2: Lattice fitting of PbS-CdS nanocrystals shown in Figure 3.6 b) and 3.6 c) to the rock salt PbS structure. <x,y> denotes the angle between two intersecting planes x and y. Planes are identified in Figure 3.6 c).

Nanocrystal identification as cubic PbS		
Figure 6(c): [031] projection		
	Measurement	Matching
Plane 1	d=1.79 Å	1.76 Å ($11\bar{3}$)
Plane 2	d=1.79 Å	1.77 Å ($1\bar{1}3$)
Plane 3	d=2.97 Å	2.98 Å (200)
<1, 2>	31.5°	32.2°
<1, 3>	58.5°	57.9°
<2, 3>	90.0°	89.9°

Chapter 4

Enzymatic Biomineralization of Biocompatible $CuInS_2$, $(CuInZn)S_2$ and $CuInS_2$/ZnS Core/shell Nanocrystals for Bioimaging

4.1 Introduction

This work demonstrates a bioenabled fully aqueous phase and room temperature route to the synthesis of $CuInS_2$/ZnS core/shell quantum confined nanocrystals conjugated to IgG antibodies and used for fluorescent tagging of THP-1 leukemia cells. This elegant, straightforward and green approach avoids the use of solvents, high

temperatures and the necessity to phase transfer the nanocrystals prior to application. Non-toxic $CuInS_2$, $(CuInZn)S_2$, and $CuInS_2$/ZnS core/shell quantum confined nanocrystals are synthesized via a biomineralization process based on a single recombinant cystathionine γ-lyase (CSE) enzyme. First, soluble In-S complexes are formed from indium acetate and H_2S generated by CSE, which are then stabilized by L-cysteine in solution. The subsequent addition of copper, or both copper and zinc, precursors then results in the immediate formation of $CuInS_2$ or $(CuInZn)S_2$ quantum dots. Shell growth is realized through subsequent introduction of Zn acetate to the preformed core nanocrystals. The size and optical properties of the nanocrystals are tuned by adjusting the indium precursor concentration and initial incubation period. $CuInS_2$/ZnS core/shell particles are conjugated to IgG antibodies using EDC/NHS cross-linkers and then applied in the bioimaging of THP-1 cells. Cytotoxicity tests confirm that $CuInS_2$/ZnS core/shell quantum dots do not cause cell death during bioimaging. Thus, this biomineralization enabled approach provides a facile, low temperature route for the fully aqueous synthesis of non-toxic $CuInS_2$/ZnS quantum dots, which are ideal for use in bioimaging applications.

4.2 Results

Incubation of CSE with a buffered solution of copper acetate leads to the appearance of an optical absorption onset at $\sim$700 nm, which is in agreement with that expected for the formation of $Cu_{2-x}S$ nanocrystals, Figure 4.1 a). This process is similar to the biomineralization of CdS and PbS as previously reported by our group.[36, 82, 35, 83] Mineralization occurs as H_2S is generated by the enzymatic turnover of L-cysteine by CSE. This H_2S then reacts with the metal salt in solution to form the metal

sulfide. This process is analogous to the chemical route to aqueous phase sulfide mineralization whereby reactive Na_2S is added to induce mineralization of, for example, $Cu_{2-x}S$.[84] The formation of nanoparticles, as opposed to bulk materials, is due to (i) the presence of the L-cysteine which can act as a capping agent [85, 86] and (ii) the templating ability of the CSE enzyme itself [36]. Unfortunately, no corresponding fluorescence peak could be observed due to a very low fluorescence intensity. This is a common issue with $Cu_{2-x}S$ nanocrystals, and is typically attributed to oxidation of as-synthesized stoichiometric Cu_2S nanocrystals to form non-fluorescing non-stoichiometric $Cu_{2-x}S$. Hence, fluorescence data for these $Cu_{2-x}S$ materials is rarely reported. To our knowledge, only two groups have reported such data for $Cu_{2-x}S$ materials which were synthesized under strictly oxygen free conditions.[87, 88]

Similar incubation of CSE in a buffered solution of indium nitrate leads to the appearance of an absorbance peak centered at 290 nm that grows in intensity with increasing incubation time, Figure 4.1 b). A peak at the same position is observed when indium and Na_2S are combined in the presence of L-cysteine, Figure 4.10. When L-cysteine is not present in solution, a cloudy solution forms with no strong peak at 290 nm. This suggests the formation of bulk indium sulfide and indium hydroxide precipitates, which occur at neutral and basic pH.[89] The peak position at 290 nm is in agreement with prior reports and is due to the formation of small (< 1 nm) molecular indium sulfide clusters.[90, 91, 92, 93] No shift in the absorbance spectra was observed, indicating that the clusters remain the same size over the incubation period. The growth in intensity of this peak with synthesis time is indicative of an increasing concentration of these clusters, formed as the enzyme turns over more of the

L-cysteine to form H_2S. In support of this concept, doubling the concentration of L-cysteine and CSE was found to increase the rate of growth in peak intensity, see Figure 4.11, demonstrating an increased synthesis rate of the molecular clusters. Therefore, while reaction with transition metals leads to the formation of solid precipitates [94], reaction with indium leads to the formation of ultra-small soluble clusters.

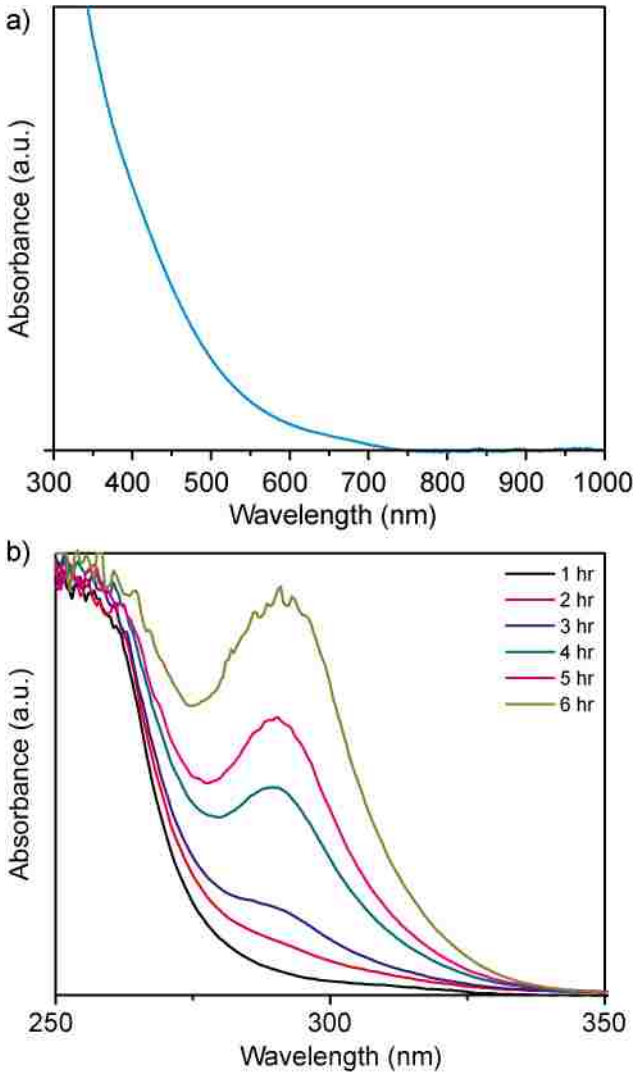

Figure 4.1: Absorbance spectra of a) $Cu_{2-x}S$ nanocrystals and b) In-S complex solutions as a function of time when synthesized by incubation of CSE, L-cysteine and copper acetate or indium nitrate, respectively.

The addition of 2 mM copper acetate to solutions containing these biomineralized In-S clusters leads to an immediate change in solution color to yellow, orange or red, Figure 4.2 a). Both the solution color and absorbance spectra, Figure 4.2 b), are consistent with the formation of $CuInS_2$ nanocrystals, agreeing with previously reported data for $CuInS_2$ formed by chemical synthesis routes.[95, 96, 97, 98, 99] The sequential method of synthesis is required in order to prevent the nucleation of a secondary population of $Cu_{2-x}S$ nanoparticles, shown by the altered absorbance peak shape and formation of a brown solution (Figure 4.12). The absorbance peak of the $CuInS_2$ quantum dot solutions was found to shift to longer wavelength positions with increasing incubation time and increasing L-cysteine concentration in the original indium containing solution. The shift in absorption peak wavelength is indicative of larger particles forming with increasing In-S precursor concentration. The band gap values for each solution shown in Figure 4.2 were calculated using a Tauc plot and range from 2.35 to 1.93 eV, Table 4.1. These band gap values indicate the formation of quantum confined nanocrystals with band gap values above 1.53 eV, which is the reported bulk band gap of $CuInS_2$.

The fluorescence from these samples is low (Figure 4.2 c), most likely suppressed due to the presence of surface defects resulting from the low temperature, aqueous synthesis.[100] For crystalline nanoparticles synthesized with 16 mM cysteine, photoluminescence peaks were obscured by fluorescence from the enzyme. However, a small shoulder could be identified at around ∼600 nm in Figure 4.2 c) for the case of a 4 h indium incubation. Solutions synthesized with 32 mM cysteine exhibit photoluminescence peaks shifting from 615 nm to 650 nm after 2 or 4 h indium incubation, respectively. After 6 h indium incubation, the photoluminescence peak no longer

shifts but appears to decrease in intensity. This suggests the maximum number of In-S complexes has been generated in solution after 4 h In incubation, so larger crystals are no longer able to form.

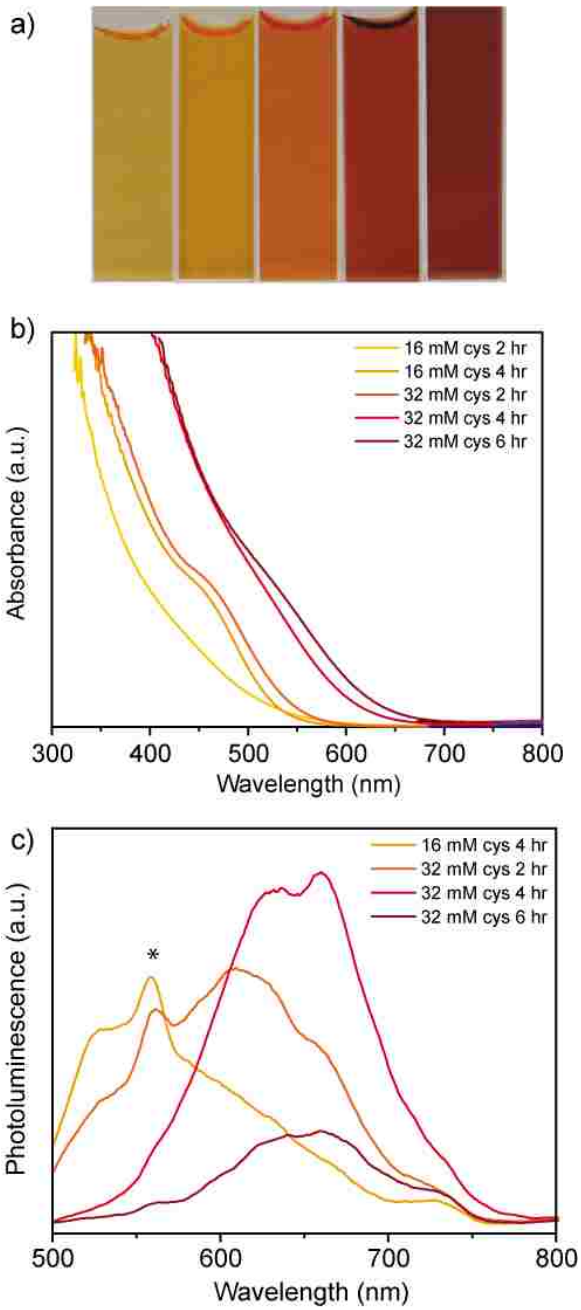

Figure 4.2: a) Photographs of solutions upon addition of 2 mM Cu acetate to solutions of CSE, L-cysteine and indium nitrate previously incubated for the time-period indicated and with the specified cysteine precursor concentrations. The corresponding absorbance and photoluminescence spectra of this set of materials are shown in b) and c) respectively. The * in c) denotes the Raman peak of water which is not part of the quantum dot fluorescence.

Some groups have also reported that changes in the relative Cu and In compositions (as well as size) can cause shifts in the optical spectra of $CuInS_2$ quantum dots.[101, 102, 103] Quantitative SEM-XEDS analysis was utilized to determine the compositions of quantum dots for three different indium incubation times. For $CuInS_2$ solutions made with 16 mM cysteine and 4 h In incubation time, the Cu/In ratio was 1.6±0.09. When 32 mM cysteine was used with In incubation times of 4 or 6 h, the Cu/In ratios were found to be 0.7±0.04 and 0.6±0.04, respectively. As previously shown in Figures 4.1 b) and 4.11, a lower concentration of cysteine decreases the number of In-S complexes; therefore, a higher Cu/In ratio is expected for the 16 mM cysteine sample. When more In-S complexes are present, (as in the latter two samples) the $CuInS_2$ nanocrystals appear to be Cu deficient. Typically, such Cu deficient $CuInS_2$ nanocrystals have blue-shifted optical properties. As our nanocrystal solutions prepared with 32 mM cysteine continue to show a red-shift in absorbance properties relative to the 16 mM sample, we believe the change in optical properties noted is being dominated by competing quantum confinement effects arising from particle size variations.[98, 104]

Figure 4.3 a) shows a HRTEM phase contrast image of a representative $CuInS_2$ nanocrystal from the 32 mM cysteine, 4 h In incubation specimen shown in Figure 4.2 b). A corresponding lower magnification HRTEM image showing a larger sampling of these nanocrystals is presented in Figure 4.13. The nanocrystal diameter is approximately 2.5 nm, which suggests that the quantum dot solutions should have a photoluminescence peak at ∼650 nm when compared to literature reports for chemically synthesized quantum confined $CuInS_2$ nanocrystals with a Cu/In ratio of 0.7.[97] As expected, the optical properties of our material are blue-shifted from chemically

synthesized nanocrystals of 2.7 nm mean diameter and 1:1 Cu:In stoichiometry, which are reported to have a photoluminescence peak at around 700 nm.[104] The corresponding fast Fourier transform (FFT) derived from Figure 4.3 a) and shown in Figure 4.3 b) can be indexed to the $[10\bar{3}]$ projection of the chalcopyrite structure of $CuInS_2$, Table 4.2. A representative X-ray energy dispersive spectrum (STEM-XEDS) from an isolated particle, Figure 4.3 c), confirms the co-existence of indium, copper, and sulfur within a single particle. The copper peaks have a slight overlap with Ni, which is present from the TEM support grid. HRTEM phase contrast images of nanocrystals formed from a solution of 4 mM indium, 16 mM L-cysteine, 0.1 mg/mL CSE for 4 h initial indium show even smaller, $\sim$2 nm particles (Figure 4.14). Again, the corresponding photoluminescence peak at $\sim$600 nm is consistent with those reported for 2 nm chemically synthesized particles of similar composition.[100]

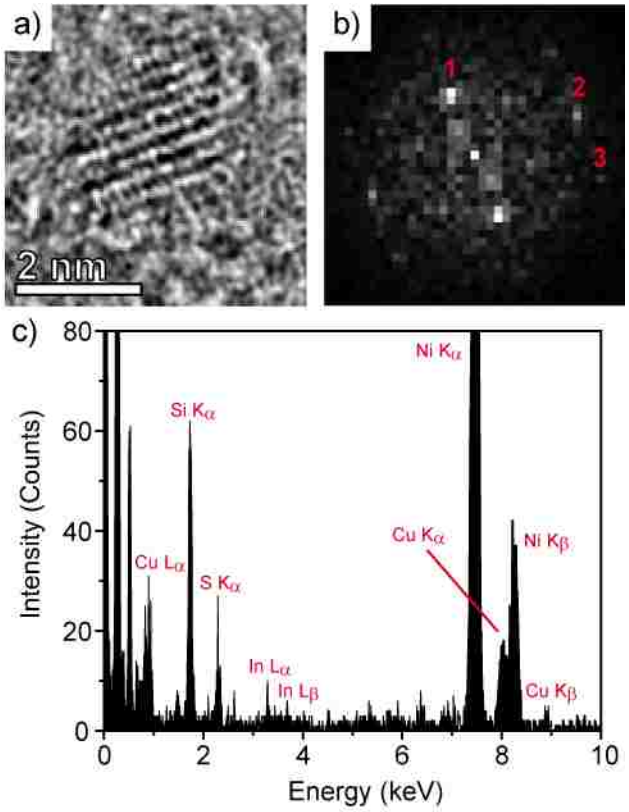

Figure 4.3: a) HRTEM phase contrast image and b) the corresponding FFT of a single 2.5 nm $CuInS_2$ nanocrystal. Fitting of the interplanar spacings and angles of the planes in the FFT are reported in Table 4.2 and are consistent with the chalcopyrite crystal structure viewed along $[10\bar{3}]$. c) Single particle STEM-XEDS analysis confirms the co-existence of Cu, In, and S within the particle.

Many groups have shown that the growth of a ZnS shell on $CuInS_2$ quantum dots significantly increases the quantum yield. We have previously reported biomineralization of PbS/CdS core/shell particles through the sequential addition of precursors.[82] Incubation of CSE in a buffered solution of zinc acetate and L-cystiene leads to the formation of an absorption peak at 280 nm, Figure 4.15, in agreement with reports of ZnS nanoparticle formation.[105, 106, 107] As such, we adapted our previously demonstrated procedure to incubate $CuInS_2$ core nanoparticles in a buffered zinc acetate solution with L-cysteine and CSE. Figure 4.4 shows the absorbance and photoluminescence spectra of the resulting material as a function of increasing incubation time with zinc acetate. Although the absorbance spectrum remains essentially unchanged except at the longest growth time, the photoluminescence properties improve dramatically over time. The photoluminescence peak slightly blue shifts relative to that of the core $CuInS_2$ nanocrystals, indicating the growth of a ZnS shell. Although core/shell quantum dots typically have photoluminecence spectra which are red-shifted from the core nanocrystals, many groups report a blue shift with $CuInS_2$/ZnS core/shell quantum dots and attribute this to a slight etching of the $CuInS_2$ core size during shell growth.[66, 104] The quantum yield of the as synthesized $CuInS_2$/ZnS quantum dots was determined to be approximately 0.1% relative to the standard dye Coumarin 153 in ethanol. While this quantum yield is low compared to previous reports of $CuInS_2$/ZnS prepared in the aqueous phase [100], these latter methods required high temperature and/or pressure to form the nanocrystals. Poor photoluminescence quantum yields are commonly found for biomineralized quantum dots made at low temperatures, and ongoing work is focused on further improving the overall quantum yield while retaining the application advantages of an aqueous synthesis

procedure that operates under ambient conditions.

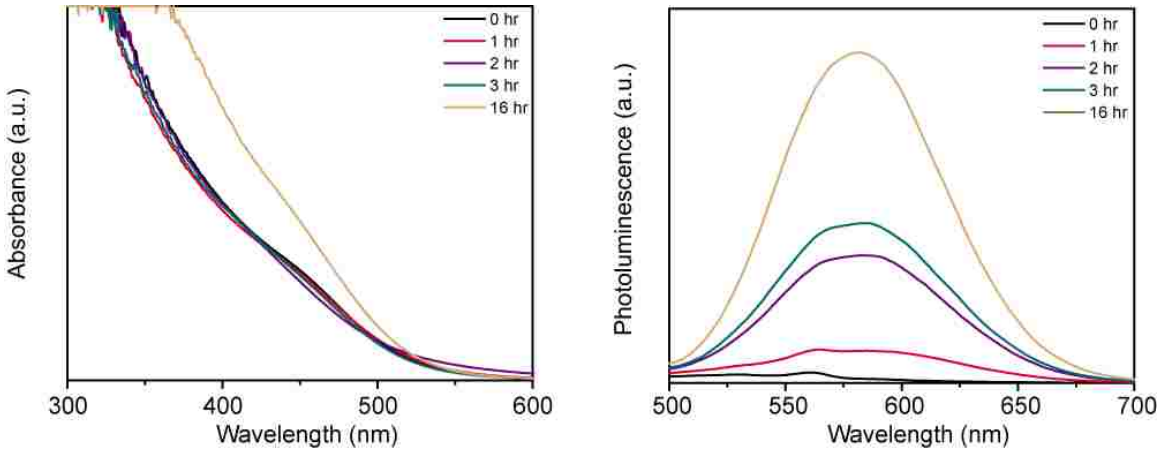

Figure 4.4: Absorbance and photoluminescence spectra of $CuInS_2$/ZnS core/shell nanocrystals grown with increasing incubation time at room temperature.

Figures 4.5 a, b) shows some representative HRTEM phase contrast images of the biomineralized $CuInS_2$/ZnS core/shell nanocrystals. A lower magnification image is shown in Figure 4.16. The crystals are approximately 4 nm in diameter, which is larger than the typical corresponding core nanocrystal shown in Figure 4.2 a). The lattice spacings and interplanar angles derived from the corresponding FFTs for both particles, Figure 4.5 c, d), can be assigned to the [010] projection of chalcopyrite structure of $CuInS_2$, Table 4.3. Based on the measured photoluminescence maxima of 630 nm for this material, we would expect the $CuInS_2$ core of these nanocrystals to be approximately 2-2.5 nm.[104, 108] Assuming no intermixing of the core and shell materials, the increased overall size of the observed quantum dots suggests the growth of a $\sim$0.75 nm thick ZnS shell on a $\sim$2.5 nm diameter core. The lattice parameter for sphalerite ZnS is 0.58 nm, suggesting the growth of $\sim$1.5 monolayers. The growth of an epitaxial shell is consistent with previous reports of chemically

synthesized $CuInS_2$/ZnS core/shell particles [109, 66] and is expected for this system because $CuInS_2$ and ZnS (the sphalerite form) have a lattice mismatch which is less than 2%.[21] Single particle STEM-XEDS analysis, Figure 4.5 e), confirms the co-existence of copper, indium, sulfur and zinc within individual particles. It was not possible using either HRTEM phase contrast or HAADF-STEM imaging modes to see a direct contrast difference between the core and shell material in this system.

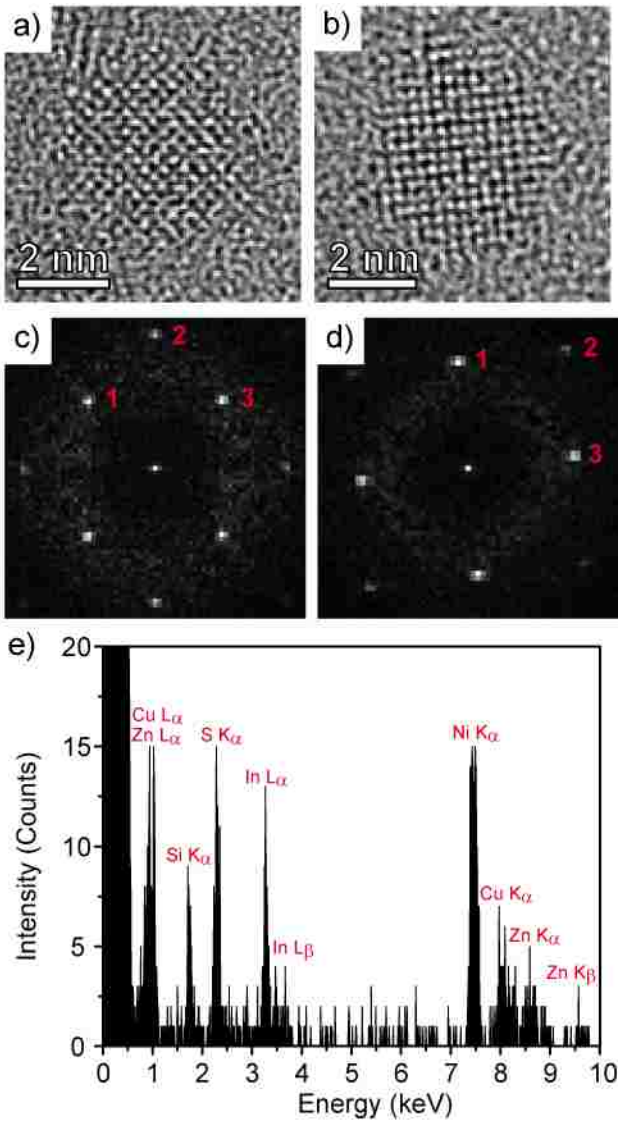

Figure 4.5: a,b) HRTEM phase contrast images and c,d) the corresponding FFTs of 4 nm $CuInS_2$/ZnS nanocrystals with cores grown with 32 mM cys, 4 h In incubation time and Zn acetate in solution for 12 h viewed along the [010] projection. Lattice fitting of the planes in the FFT are presented in Table 4.3. e) Representative STEM-XEDS spectrum showing the co-existence of Cu, In, S, and Zn within a single particle.

The average composition of the same $CuInS_2$/ZnS core/shell particle preparation shown in Figure 4.5 was analyzed using SEM-EDS. The Cu/In ratio was found to be 1.46 $\pm$0.18 (as compared the core material which had a Cu/In ratio of 0.74) and the Zn/In ratio was 2.3$\pm$0.29. The increase in Cu/In ratio relative to the starting core material suggests that the zinc is preferentially substituting for indium cations in the crystal lattice, as no additional copper was added to the solution during ZnS shell growth. This decrease of indium has also been reported by Chen et al., who also utilized an aqueous synthesis method in open air. In a similar manner to our system, they observed a reduction of indium content for $CuInS_2$/ZnS core/shell nanocrystals that have Cu/In ratios of less than 1 in the starting $CuInS_2$ core quantum dots.[100]

Several groups have also reported that the mixed quaternary $(CuInZn)S_2$ alloy shows improved photoluminescence properties over $CuInS_2$ nanocrystals.[110, 111, 17] To determine whether biomineralization with CSE was capable of producing a quaternary alloy, we simultaneously added zinc acetate and copper acetate to a solution of 4 mM indium acetate, 32 mM L-cysteine, and 0.2 mg/mL CSE which had been incubated for 4 hours. Figure 4.6 shows images, absorbance spectra, and photoluminescence spectra of the resulting quaternary sols compared to that for sols of $CuInS_2$ and sequentially prepared $CuInS_2$/ZnS core/shell nanoparticles. The absorbance and fluorescence peaks of the $(CuInZn)S_2$ material are both significantly blue shifted from those of the $CuInS_2$ quantum dots formed from the same In-S complex solution, consistent with the expected optical properties for quaternary alloy quantum dots.[17, 112] Additionally, the level of fluorescence is significantly improved compared to the $CuInS_2$ quantum dots, but was still not able to match the improved peak intensity shown by the core/shell type particles which had zinc acetate added

after the formation of the $CuInS_2$ core. This indicates that adding zinc with copper does in fact produce an intimately mixed quaternary alloy, whereas adding zinc after the initial $CuInS_2$ quantum dots are formed produces a more core/shell type morphology.

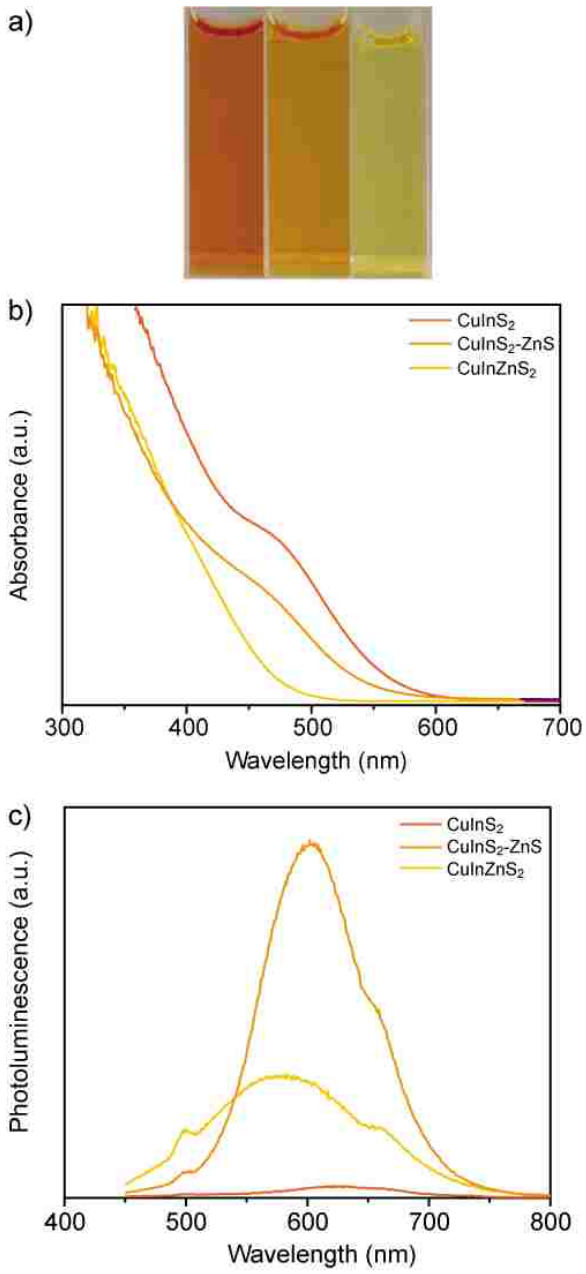

Figure 4.6: a) Images, b) absorbance spectra, and c) photoluminescence spectra showing the difference between the original $CuInS_2$ quantum dot sol and those materials synthesized with sequential addition versus simultaneous addition of Cu and Zn precursors leading to the formation of a $CuInS_2$/ZnS core/shell morphology or a $(CuInZn)S_2$ random alloy, respectively.

Figure 4.7 a) shows an HRTEM phase contrast image of a representative $(CuInZn)S_2$ nanocrystal from the sol whose optical properties are shown in Figure 4.6. The particles appear to be ∼5 nm in diameter and have a more irregular shape as compared to the corresponding $CuInS_2$ and $CuInS_2$/ZnS core/shell particles. The photoluminescence peak at 575 nm is blue-shifted in comparison to other reports for 4-5 nm $(CuInZn)S_2$ nanocrystals with a nominal 1:1:1 stoichiometry of Cu:In:Zn cations. However, the cationic ratios measured using SEM-EDS was 1.84±0.13 for Cu/In and 2.07±0.14 for Cu/Zn. Similar to the core/shell nanocrystals, the Cu/In ratio is significantly increased with the incorporation of Zn as compared to the $CuInS_2$ core-only material. Jiang et al. have reported a significant blue-shift in the optical properties for $(CuInZn)S_2$ nanocrystals having a small indium content relative to zinc.[110] The low indium content in addition to high zinc content in the alloy sample may play a dominant role in determining the optical properties as opposed to size quantization in this case. Figure 4.7 b) shows the corresponding FFT for the particle imaged on Figure 4.7 a) which matches well to the $[02\bar{1}]$ projection of the chalcopyrite phase (see lattice fringe fitting in Table 4.4). A STEM-XEDS spectrum acquired from a single nanoparticle is shown in Figure 4.7 c) and confirms that copper, indium, zinc, and sulfur all co-exist in a single particle. No separate nucleation of $Cu_{2-x}S$, In_2S_3, or ZnS nanocrystals was detected in our electron microscopy analyses.

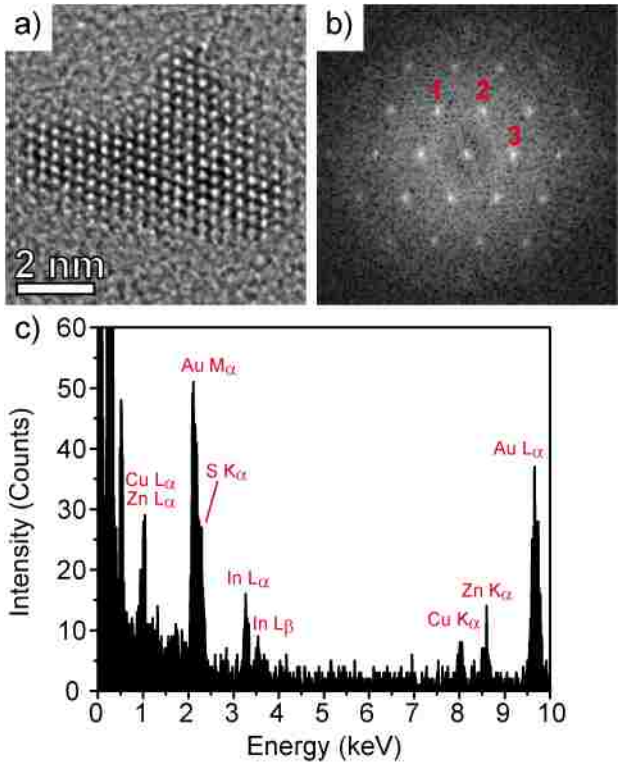

Figure 4.7: a) HRTEM phase contrast image and b) corresponding FFT of a representative 5 nm $(CuInZn)S_2$ nanocrystal viewed along the $[02\bar{1}]$ projection. Lattice fitting of planes indicated in the FFT are reported in Table 4.4. c) Representative STEM-XEDS spectrum showing the co-existence of Cu, In, S, and Zn within the single nanoparticle.

This proposition of core/shell formation versus quaternary alloy formation is further verified through photoluminescence lifetime measurements of core $CuInS_2$, alloy $(CuInZn)S_2$, and core/shell $CuInS_2$/ZnS nanocrystals, as shown in Figure 4.8. $CuInS_2$ particles typically have two decay lifetimes; the first, a short lifetime (∼10-50 ns) and second longer lifetime (∼100-500 ns), have been assigned to non-radiative and radiative decay processes, respectively.[95, 113] Because our $CuInS_2$ core-only nanocrystals have poor photoluminescence characteristics, overall shorter lifetimes of 2.4 ns and 13.9 ns for these two processes were observed. The time constants increase slightly to 2.8 ns and 31 ns, respectively, for the $(CuInZn)S_2$ quaternary alloy nanocrystals. Both time constants increase markedly to 9.4 ns and 74.5 ns respectively, upon incubation of $CuInS_2$ in the zinc acetate containing solution to form $CuInS_2$/ZnS core/shell nanocrystals. In the case of the $(CuInZn)S_2$ alloyed nanocrystals, the increase in the decay emission is attributed to a slight passivation of donor defects within the crystal lattice.[17] The substantial increase in the radiative decay lifetime for the $CuInS_2$/ZnS core/shell type quantum dots is a typical result of increased surface passivation upon growth of a shell onto core nanocrystals.[113]

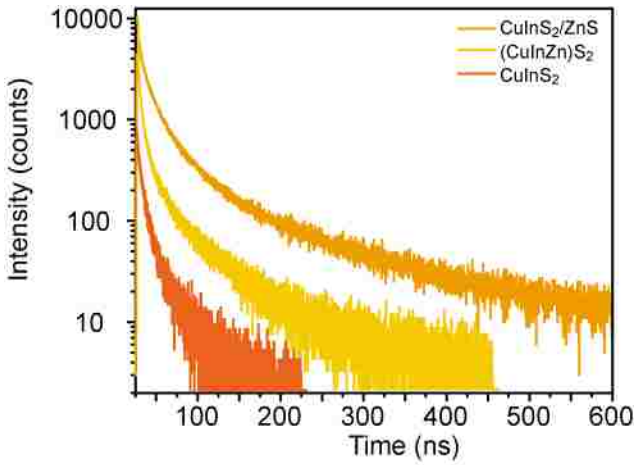

Figure 4.8: Time resolved photoluminescence decay curves for the $CuInS_2$ core nanocrystals only, the $(CuInZn)S_2$ quaternary alloy and the $CuInS_2$/ZnS core/shell nanocrystals.

To demonstrate that our biomineralized $CuInS_2$/ZnS core/shell nanocrystals could be effective for bio-labeling, the as-synthesized quantum dots were conjugated to IgG antibodies using EDC/NHS cross-linkers, which then bind to the epidermal growth factor receptor (EGFR) of the THP-1 leukemia cells. THP-1 is an established cell line used for biomarker detection in cancer and contains the target receptor of interest, namely EGFR.[114, 115] Figure 4.9 a) shows a confocal image of THP-1 cells incubated with $CuInS_2$/ZnS nanocrystals that had not yet been conjugated to anti-EGFR antibody. The red signal indicates fluorescence from the $CuInS_2$/ZnS quantum dots, which is even across the sample, confirming no site-specific fluorescence inside the cells. In contrast, Figure 4.9 b) shows a confocal image of THP-1 cells after 1 h of incubation with $CuInS_2$/ZnS quantum dots tagged with IgG. The cells were washed twice prior to imaging in the confocal light-optical microscope to remove any unbound quantum dots. The fluorescence from the $CuInS_2$/ZnS quantum dot-IgG conjugates is localized to patches on the cell surface; a similar pattern of EGFR clustering at

the cell surface has been described before due to the dimer-dependent activation of EGFR.[116, 117] The absence of site specific fluorescence in Figure 4.9 a) confirms that the $CuInS_2$/ZnS quantum dots were not taken into to cells using already present endocytosis or phagocytosis pathways, which has been previously reported for small nanocrystals.[118, 119] In order to monitor the toxicity of quantum dots, a Trypan blue assay was utilized to determine the percentage of dead THP-1 cells after incubation with the $CuInS_2$/ZnS quantum dot solution. Over a period of 6 h, the percentage of living cells remained at an average of 95.5% $\pm$ 2.6%, demonstrating that the quantum dots have little or no adverse toxic effect on the target THP-1 cells.

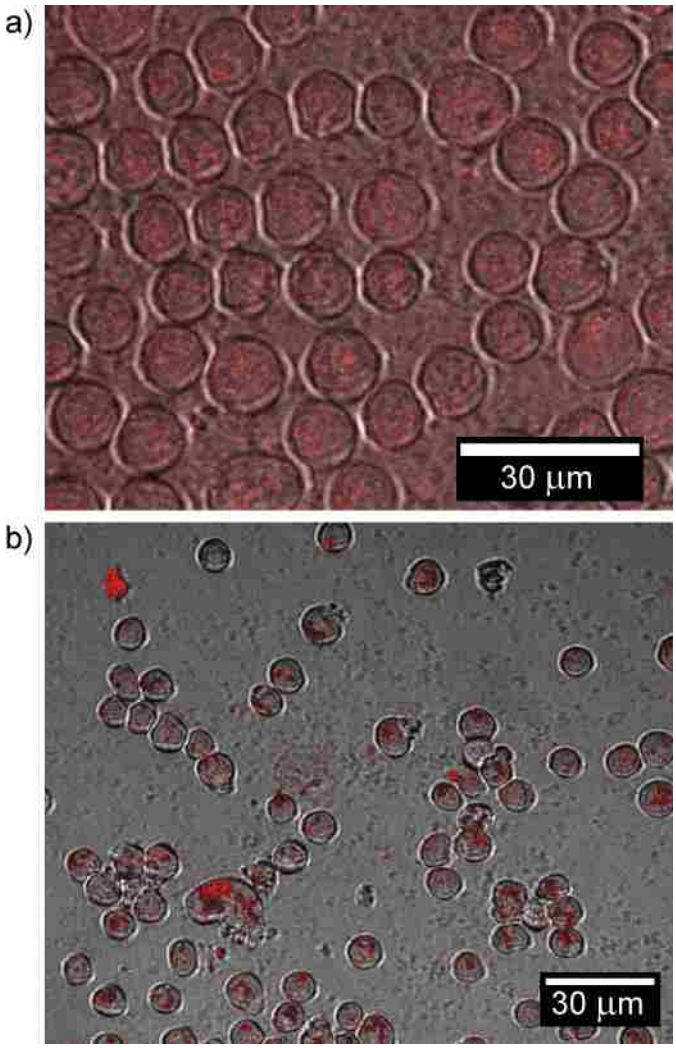

Figure 4.9: Light optical confocal microscope images of THP-1 cells a) incubated in solution with $CuInS_2/ZnS$ quantum dots with no IgG antibody tagging, and b) tagged with $CuInS_2/ZnS$ quantum dots, bioconjugated to an IgG antibody. The red coloration corresponds to quantum dot fluorescence, and is only site specific when the IgG antibody on the THP-1 leukemia cells are conjugated to the $CuInS_2/ZnS$ nanocrystals.

4.3 Discussion

The biomineralization of $CuInS_2$ or $(CuInZn)S_2$ nanocrystals requires a slightly more complex approach than the straightforward direct biomineralization from buffered solutions of metal salt, L-cysteine and CSE demonstrated for $Cu_{2-x}S$ and ZnS herein, and for PbS and CdS in our previous work.[82, 35] These latter materials will directly form a metal sulfide solid upon reaction with the reactive sulfur, likely H_2S, formed by the enzymatic turnover of L-cysteine by the putative cystathionine γ-lyase class CSE enzyme.[36] In contrast, reaction with indium nitrate forms a relatively stable species with a characteristic absorption peak at 290 nm, which has previously been identified as a molecular cluster of indium and sulfur [93], rather than bulk or nanocrystalline In_2S_3. A similar result is obtained upon addition of Na_2S to a mixture of indium nitrate with L-cysteine, whereas a bulk precipitate of In_2S_3 likely combined with indium hydroxide is formed in the absence of L-cysteine. Thus, it appears that L-cysteine acts to stabilize these clusters. Formation of $CuInS_2$ or $(CuInZn)S_2$ nanocrystals can be initiated by reaction of copper acetate, or copper acetate and zinc acetate, in solutions containing these biologically generated clusters containing indium and sulfur.

The biomineralized $CuInS_2$ and $(CuInZn)S_2$ nanocrystals produced are within the quantum confined size range and exhibit crystal structures, lattice parameters and optical absorbance maxima positions that are equivalent to their chemically synthesized counterpart materials. Single particle XEDS analysis confirms the co-existence of the constituent elements within individual particles. As further verification, a chemical aqueous synthesis of $CuInS_2$ prepared via the addition of reactive Na_2S to a solution of copper acetate, indium chloride and L-cysteine templating agent[100],

forms nanocrystals with optical properties analogous to our purely biomineralized materials. In the chemical synthesis case, Na_2S acts as the reactive sulfur source in place of the enzymatic generation of H_2S by CSE. Thus, our biomineralization approach is capable of producing biocompatible quantum dots in the aqueous phase under ambient conditions. Unfortunately, the photoluminescence characteristics of these as-generated nanoparticles are quite low, indicative of poor surface passivation in the aqueous phase due to the low synthesis temperature employed.

Photoluminescence from $CuInS_2$ and $(CuInZn)S_2$ nanocrystals is thought to occur from intrinsic defects in the crystal structure, although the exact decay pathway is still a matter of debate.[95] This leads to relatively wide peak widths, as indicated by large full-width-half-maxima (FWHM) of ∼300 meV, even with size selective precipitation, and a large Stokes shift of ∼450 meV.[113, 98, 120] Our aqueous phase, room temperature biosynthesized nanocrystals display similar FWHM values of 300, 590 and 430 meV, and a Stokes shift of 400, 300 and 650 meV, for the $CuInS_2$, $(CuInZn)S_2$ and $CuInS_2$/ZnS, particle variants respectively. Our Stokes shift values are slightly larger than those reported for analogous chemically prepared materials (c.f. ∼400 meV for $CuInS_2$/ZnS quantum dots chemically synthesized in the aqueous phase at 95 °C).[100] The $(CuInZn)S_2$ quaternary alloy nanocrystals have a significantly higher FWHM, which is to be expected based on their highly irregular shapes.[110]

The low photoluminescence intensity of the as-synthesized $CuInS_2$ nanocrystals is most likely due to the presence of surface trap states that lead to non-radiative recombination pathways [21], and cause the short lifetimes reported in Figure 4.6. The improvement in both photoluminescence intensity and lifetimes for the $(CuInZn)S_2$ alloy nanocrystals relative to $CuInS_2$ is most likely due to passivation of defects

within the crystal lattice. Further improvement in photoluminescence and lifetimes is achieved through passivation of surface defects through the growth of a ZnS shell on the $CuInS_2$ nanocrystals. While from electron microscopy studies we cannot completely exclude the possibility of some limited zinc diffusion into the $CuInS_2$ particles rather than solely forming a ZnS overlayer, shell growth is indicated by the substantial improvement in photoluminescence intensity and lifetime when compared to the corresponding fully alloyed $(CuInZn)S_2$ particles.

$CuInS_2$ and $(CuInZn)S_2$ nanocrystals are typically formed at high temperature in an organic phase and must be phase transferred and stabilized in the aqueous phase prior to application as a fluorescent marker in biological systems.[21, 109] While this chemical approach leads to high quality materials in terms of quantum yield, it is an energy intensive and more complex synthesis route which is intrinsically far away from the generally desirable ethos of green production of materials. In contrast, the direct biomineralization approach demonstrated in this paper results in the fabrication of stable quantum confined nanocrystals directly in the aqueous phase at room temperature.

Bioimaging applications generally require stable, aqueous phase nanocrystals that can be functionalized with a biological marker, such as an antibody. While $CuInS_2$ and $(CuInZn)S_2$ nanocrystals are typically chemically synthesized in the organic phase, they then need to be transferred into water using ligand exchange, or more commonly, encapsulation in a polymer shell, such as PEG.[66] Notably, any phase transfer procedure typically reduces the quantum yield [109, 66], while ligand exchange also reduces the stability of the quantum dots.[9] Polymer encapsulation also inevitably results in

nanocrystals which are much larger than their initial nominal size.[121] Our biomineralized quantum dots have the advantage of being synthesized in biologically relevant aqueous buffers, and have high stability while still retaining an ultra-small size. They do not require any additional processing steps after synthesis and can be conjugated to antibodies directly from the synthesis solution without adversely affecting cell-surface binding properties.

The primary drawback of the biomineralization approach is the relatively low photoluminescence intensity displayed by our nanocrystals even after ZnS capping, when compared to those fabricated at high temperature in the organic phase via traditional chemical routes.[66, 17] This is most likely due to the combination of the aqueous solvent and low temperature synthesis conditions employed. As noted, the quantum yield of chemically synthesized materials is reduced significantly upon phase transfer to the aqueous phase due to relatively poor capping by the aqueous stabilizing ligands.[109, 66] While some groups have reported quantum yields of up to 38% for aqueous synthesized $CuInS_2$/ZnS core/shell nanocrystals, these alternative chemical synthesis routes utilize elevated temperatures and/or pressure.[100] Growth at lower temperatures likely leads to a greater intrinsic defect population in the particles. However, this must be placed in context with the relative infancy of this enzymatic biomineralization approach to functional nanomaterial synthesis when compared to the more traditional routes. We anticipate that further developments of these embryonic biomineralized synthesis protocols will occur over time and lead to higher quality materials, just as they have over the past two decades for the chemical synthesis protocols.

4.4 Conclusions

This work has unambiguously demonstrated the direct biomineralization of $CuInS_2$, $(CuInZn)S_2$, and $CuInS_2$/ZnS core/shell quantum dots in the aqueous phase using a single enzyme, namely CSE. The $CuInS_2$ and $(CuInZn)S_2$ alloy nanocrystals are formed using a two-step nucleation process; the first step creates soluble In-S complexes stabilized by L-cysteine, while the second step immediately forms $CuInS_2$ or $(CuInZn)S_2$ nanoparticles following the addition of the corresponding non-indium precursor(s). The CSE can also be utilized for subsequent ZnS shell growth on $CuInS_2$, and is achieved by adding zinc acetate to the preformed $CuInS_2$ quantum dots, resulting in a dramatic improvement in their photoluminescence performance. The resultant $CuInS_2$/ZnS particles can be successfully conjugated to an IgG antibody using EDC/NHS cross-linkers and then utilized for the specific tagging of EGFR receptors on THP-1 leukemia cells and used for their subsequent visualization in confocal fluorescence optical microscopy experiments.

4.5 Supplemental Information

The following information is provided as supplementary information for the results presented in Section 4.2.

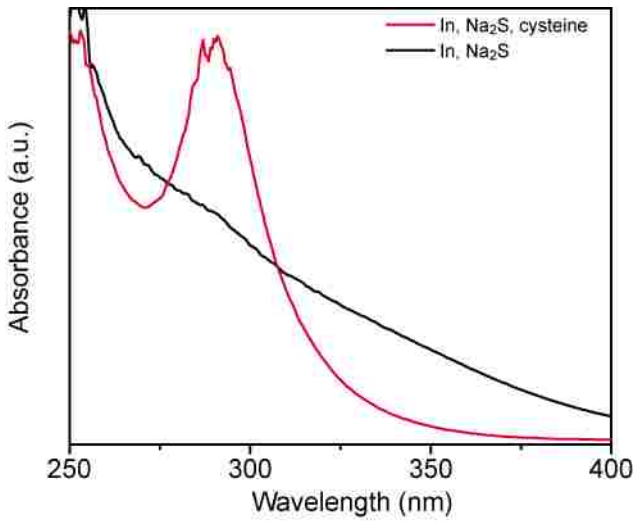

Figure 4.10: Absorbance spectrum with a peak at 290 nm of a buffered solution of 4 mM indium, 8 mM Na_2S with 8 mM cysteine and without L-cysteine.

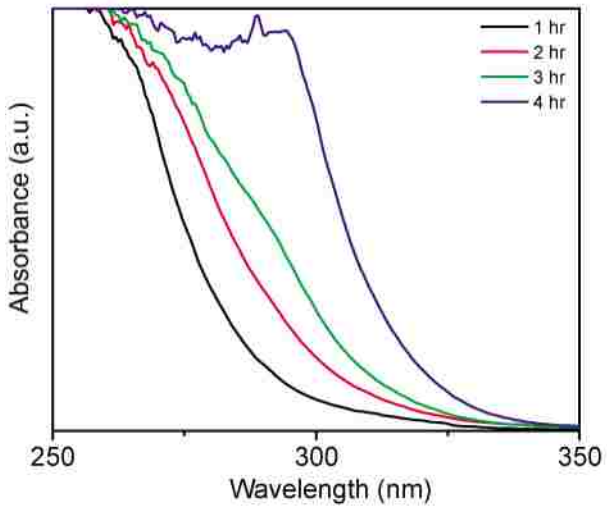

Figure 4.11: Absorbance spectrum of a buffered solution of 4 mM indium, 0.2 mg/mL CSE and 32 mM L-cysteine, showing faster growth of the peak at 290 nm relative to that in Figure 4.1(b).

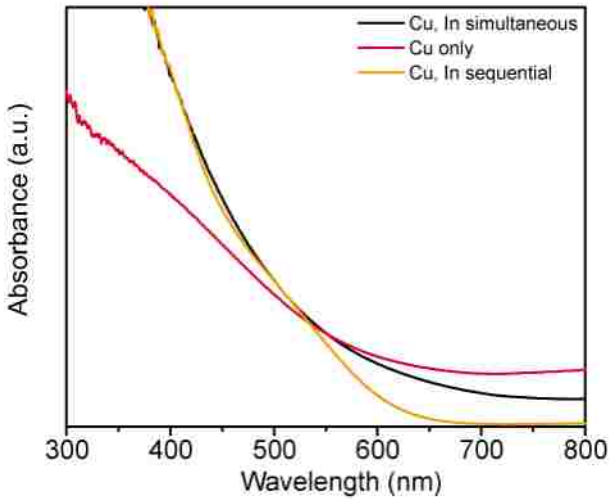

Figure 4.12: Absorbance spectra from a buffered solution of 0.2 mg/mL CSE and 32 mM L-cysteine with copper and indium incubated together compared to solutions incubated with only copper or pre-incubated with indium for 2 h before adding copper.

Table 4.1: Calculated band gap values for the various sols presented in Figure 4.2.

Sample	Band gap (eV)
16 mM cys 2 h	2.35
16 mM cys 4 h	2.33
32 mM cys 2 h	2.26
32 mM cys 4 h	2.04
32 mM cys 6 h	1.93

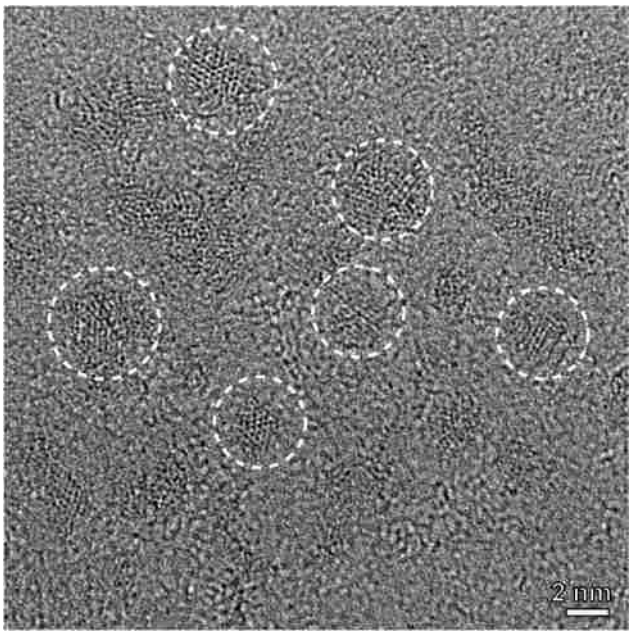

Figure 4.13: HRTEM image showing several $CuInS_2$ nanocrystals, with a mean size of 2.5 nm, from the 32 mM cysteine, 4 h In incubation sample whose optical properties are shown in Figure 4.2 b).

Table 4.2: Lattice fringe fitting of the $CuInS_2$ nanocrystal shown in Figure 4.3 a) to the chalcopyrite $CuInS_2$ structure.

Nanocrystal identification as tetragonal $CuInS_2$		
Figure 2(a): $[10\bar{3}]$ projection		
	Measurement	Matching
Plane 1	d=2.92 Å	2.76 Å (020)
Plane 2	d=1.75 Å	1.81 Å (301)
Plane 3	d=1.49 Å	1.51 Å (321)
<1, 2>	89.1°	90.0°
<1, 3>	57.5°	56.7°
<2, 3>	31.6°	33.3°

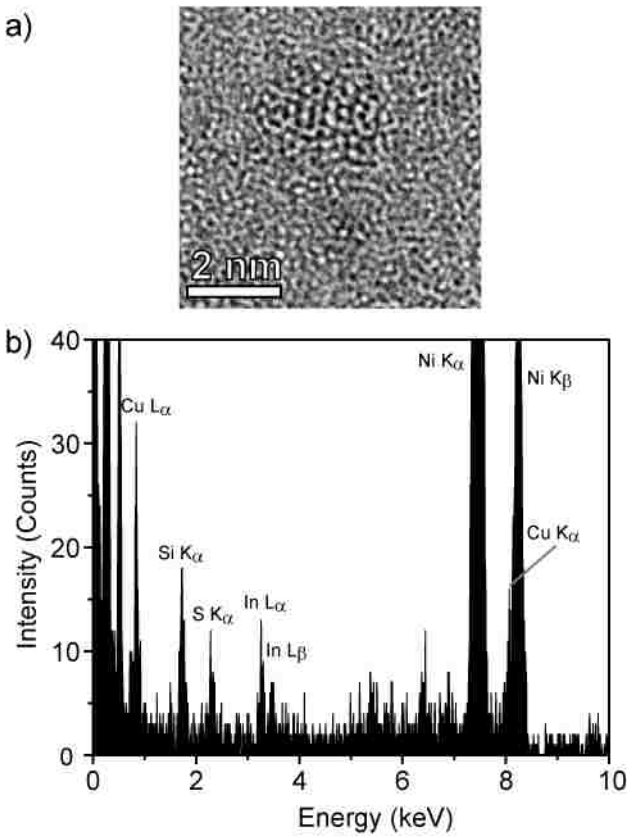

Figure 4.14: a) HRTEM phase contrast image of a 2 nm $CuInS_2$ nanocrystal and b) corresponding XEDS from single particle.

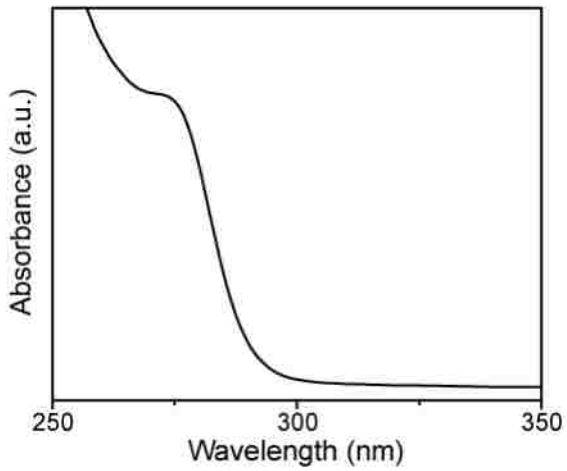

Figure 4.15: Absorbance spectrum a buffered solution of 1 mM Zn acetate, 8 mM cysteine, and 0.05 mg/mL CSE, showing an absorbance peak at 280 nm, demonstrating the formation of ZnS quantum dots.

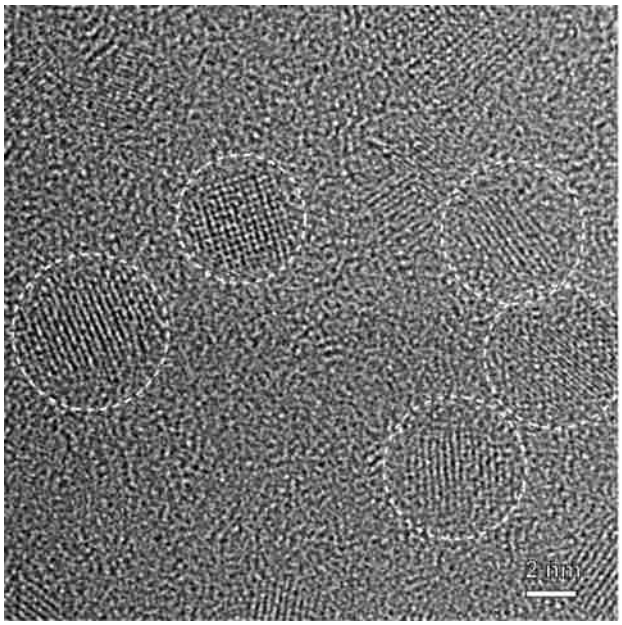

Figure 4.16: HRTEM phase contrast image showing several 4 nm $CuInS_2$/ZnS core-shell nanocrystals corresponding to core $CuInS_2$ formed from the pre-incubation of 32 mM cysteine with 4 mM In and 0.2 mg/mL CSE for 4 hr, and then incubated with Zn acetate for 12 hours.

Table 4.3: Lattice fitting of $CuInS_2$/ZnS nanocrystals shown in Figure 4.5 a) & c) to the chalcopyrite $CuInS_2$ structure.

Nanocrystal Identification as chalcopyrite $CuInS_2$					
Figure 5 a,c): [010] projection			Figure 5 b,d): [010] projection		
	Measurement	Matching		Measurement	Matching
Plane 1	d=2.80 Å	2.78 Å (004)	Plane 1	d=2.82 Å	2.78 Å (004)
Plane 2	d=1.99 Å	1.96 Å (204)	Plane 2	d=1.96 Å	1.96 Å (204)
Plane 3	d=2.77 Å	2.76 Å(200)	Plane 3	d=2.83 Å	2.76 Å (200)
<1, 2>	45.6°	45.2°	<1, 2>	44.4°	45.2°
<1, 3>	89.6°	90.0°	<1, 3>	88.8°	90.0°
<2, 3>	44.7°	44.8°	<2, 3>	44.4°	44.8°

Table 4.4: Lattice fitting of $(CuInZn)S_2$ nanocrystals shown in Figure 4.7 a) to the expected chalcopyrite structure.

Nanocrystal identification as chalcopyrite $CuInS_2$		
Figure 7(a): $[02\bar{1}]$ projection		
	Measurement	Matching
Plane 1	d=2.75 Å	2.76 Å (020)
Plane 2	d=3.13 Å	3.19 Å (301)
Plane 3	d=3.16 Å	3.19 Å (321)
<1, 2>	54.5°	54.6°
<1, 3>	56.1°	54.6°
<2, 3>	69.4°	70.7°

Chapter 5

Green Synthesis of Reduced Graphene Oxide and CdS Quantum Dots by the Single Enzyme CSE for Photocatalytic Hydrogen Generation

5.1 Introduction

The search for affordable and sustainable energy production is driven by an exponential increase in global energy demand and the high environmental cost of burning fossil fuels. One of the most promising alternative energy technologies is photocatalysis, which uses the sun to generate chemical fuels, such as hydrogen, from water. The

first material studied for use as a photocatalyst was TiO_2, which could effectively split water due to its large band gap of 3.2 eV, which provides more energy than the theoretical requirement of 1.23 eV [122]; however, TiO_2 is only able to absorb light in the UV range, which makes up approximately 4% of the suns light spectrum. Many researchers are now focused on utilizing metal sulfides, noble metals, and layered structures to develop photocatalysts that can absorb in the visible range of light while satisfying the standard potential needed for electrolysis of water.[123]

Due to its many desirable electronic and optical properties, graphene has recently gained interest for use in photocatalysis. Several groups have demonstrated the conjugation of CdS QDs to reduced graphene oxide (rGO) for hydrogen production from water.[124] CdS is a desirable material for use in photocatalysts due to its suitable band-gap of 2.4 eV and more negative conduction band potential compared to TiO_2, necessary for splitting of water.[125] Typically, these graphene-QD photocatalysts employ Pt nanoparticles as co-catalysts and sacrificial reagents to avoid photocorrosion of the metal sulfide nanocrystals. While these photocatalysts have been proven to have improved efficiencies in water splitting by visible light, the cost and environmental impacts of synthesis continue to limit their use commercially.

In this chapter, we utilize this single-enzyme synthesis approach for both CdS QD biomineralization and reduction of GO, which are then assembled into CdS QD-rGO photocatalysts. GO, the starting material for rGO, can be synthesized scalably and inexpensively by chemical exfoliation from graphite to produce single layer soluble sheets.[37] However, GO is an insulator; thus, partial reduction is required to recover the electronic properties while retaining solubility.[126] The most common methods for partial reduction use chemical reducing agents such as hydrazine and sodium

borohydride. While highly effective, these chemicals are extremely toxic or dangerous to use, limiting the ease of commercial production of GO.

Recently, several groups have begun exploring alternative, green methods for the partial reduction of GO; examples include amino acids [127, 128], phytoextracts [129], and metal reducing organisms [130, 131, 132]. The amino acid L-cysteine has been shown to reduced GO through the decomposition of L-cysteine to H_2S; however, high temperatures and pressures were required for L-cysteine breakdown.[133] There has been one example of room temperature reduction using L-cysteine, but long incubation periods of over 72 hours were needed for complete reduction.[128] Dissimilatory metal reducing bacteria, such as the *Sewanella* species, have been demonstrated to reduce GO using pre-existing extracellular electron transfer pathways.[131] However, scale-up of these processes is not economically viable as the cells need to be grown and maintained, as well as separated from the product following synthesis.[134] For a cleaner process, proteins such as bovine serum albumin (BSA) have been shown to reduce GO; however, elevated temperatures (55-90 °C) are still required.[135]

Herein, we report the first example of rGO biosynthesis using a single enzyme to rapidly generate low concentrations of H_2S, allowing effective reduction of GO while remaining non-toxic and easy to purify. We also demonstrate, to the best of our knowledge, the first utilization of enzymatically reduced rGO with biomineralized CdS QDs as a photocatalyst, capable of hydrogen generation using visible light.

5.2 Results

Incubation of graphene oxide (GO) in a buffered solution of poly-l-lysine (PLL), L-cysteine and CSE results in a solution color change from brown to black in as little

as 2 hours. Figure 5.1 shows the absorbance spectra of 0.2 g/L GO, synthesized from graphite using the modified Hummers method, and GO incubated for 4 hours with either 10 mM L-cysteine and 0.8 mg/mL PLL, or 10 mM L-cysteine, 0.8 mg/mL PLL and 0.05 mg/mL of CSE in Tris buffer.[37] PLL was added as a linker molecule for future functionalization of the graphene with QDs.[1] The spectrum of GO shows the expected absorbance peak and shoulder at 230 and 300 nm, resulting from the $\pi \rightarrow \pi^*$ transition of the aromatic C-C bonds and n $\rightarrow \pi^*$ transition of the C=O bonds, respectively.[136] With the addition of L-cysteine and PLL, a small peak shift from 230 nm to 255 nm is observed and the shoulder at 300 nm disappears, indicating the slight reduction of GO.[137] This is consistent with previous reports of GO reduction by cysteine at room temperature; however, the time required for complete reduction was 72 hours, and the concentration of cysteine was increased 8-fold.[128] The absorbance peak at 230 shifts to 270 nm with the inclusion of CSE, demonstrating improved reduction in the presence of both enzyme and L-cysteine. The reduction does not occur with CSE unless L-cysteine is also present in solution (Figure 5.6). This indicates that the enhancement in reduction occurs from the presence of H_2S, produced by CSEs enzymatic conversion of L-cysteine to H_2S. This is a known function of this class of enzymes [138], and was previously demonstrated for this specific enzyme by our group through the biomineralization of metal sulfide QDs.[36] H_2S has been shown to be an effective reducing agent, but is not commonly used due to its toxicity.[139]

To further confirm the improved reduction of GO by CSE, FTIR spectra were recorded for each sample, shown in Figure 5.2 a). Characteristic peaks of GO are

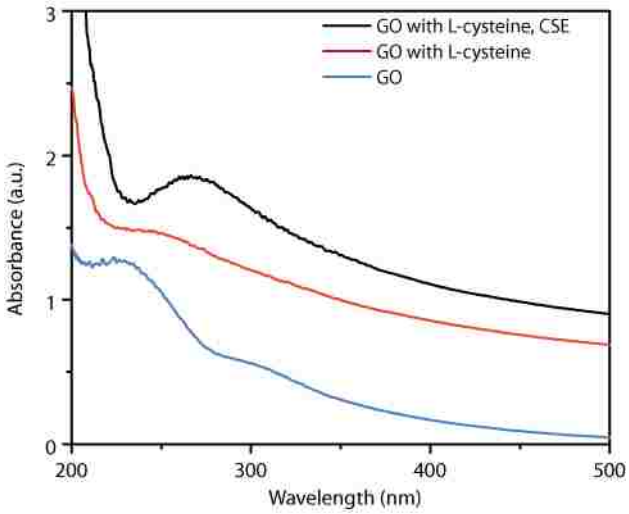

Figure 5.1: Absorbance spectra of: GO synthesized using the modified Hummers method; GO incubated with PLL and L-cysteine for 4 hours; and GO incubated with PLL, L-cysteine, and CSE for 4 hours.

located at 3450 cm^{-1} (O-H stretching), 1733 cm^{-1} (C=O stretching), 1180 cm^{-1} (C-O), and 1058 cm^{-1} (C-O stretching).[140] Following reduction by L-cysteine or both L-cysteine and CSE, these peaks are eliminated, indicating a loss of oxygen groups on the surface of the graphene sheets. Raman spectra were also recorded to evaluate the degree of reduction by comparing the intensity of the D/G peaks, shown in Figure 5.2 b). The intensity increased from 0.87 for GO, to 0.98 for rGO by L-cysteine alone, and to 1.07 for rGO by L-cysteine and CSE. These results are comparable to rGO_{PLL} reduced by $NaBH_4$, a traditional chemical reducing agent, as shown in the supplemental information, Figure 5.7.

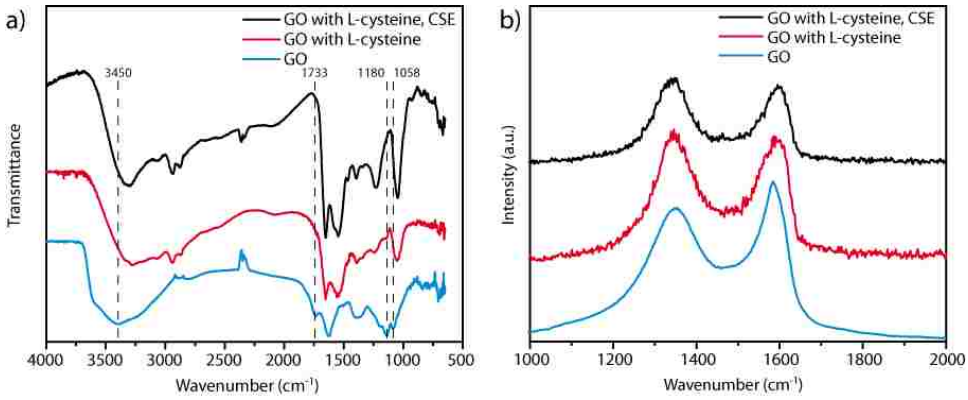

Figure 5.2: a) FTIR and b) Raman of GO and rGO by either L-cysteine or L-cysteine and CSE after 4 hours of reduction.

Following synthesis of rGO by CSE, biomineralized CdS QDs were conjugated to the surface via PLL crosslinkers. The CdS QDs were synthesized separately by CSE, as shown previously. [36] Typical absorbance data of the biomineralized CdS quantum dots is shown in Figure 5.8. In order to confirm the attachment of CdS QDs, samples were subjected to centrifugation to separate the conjugated rGO-QDs from any unattached QDs in the supernatant. Figure 5.3 shows the absorbance spectra of a mixed CdS QD and rGO solution prior to centrifugation, the supernatant following centrifugation, and the precipitated rGO resuspended in fresh Tris buffer. Before centrifugation, there is an absorbance peak around 400 nm from the CdS quantum dots with a high overall background from the rGO. Following centrifugation, the QD absorbance peak and rGO background is retained in the resuspended pellet, while the spectra from the supernatant no longer has any absorbance features. Control experiments confirm that unattached QDs cannot be separated by centrifugation due to their small size; therefore, the presence of QDs in the resuspended pellet must occur from those attached to rGO.

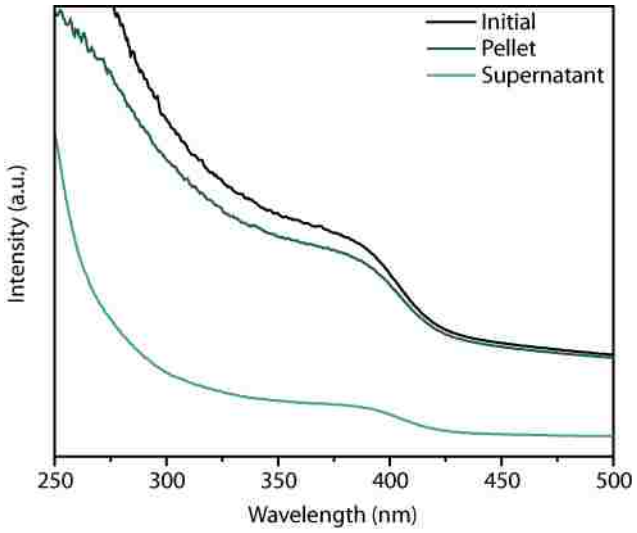

Figure 5.3: Absorbance spectra of the CdS-rGO mixture prior to centrifugation, and then both spectra for the resuspended pellet and separated supernatant following centrifugation.

Further confirmation of CdS QD attachment to rGO was achieved using STEM-HAADF imaging. Figure 5.4 shows a low magnification image of a rGO sheet decorated with CdS nanocrystals dispersed on a holey carbon film. In this case, the rGO sheet was reduced using sodium borohydride. The inset shows a high magnification image of an individual CdS nanocrystal located on rGO, with an approximate size of 5 nm. No QDs were found on the TEM grid, indicating the QDs were bound to rGO prior to TEM sample preparation.

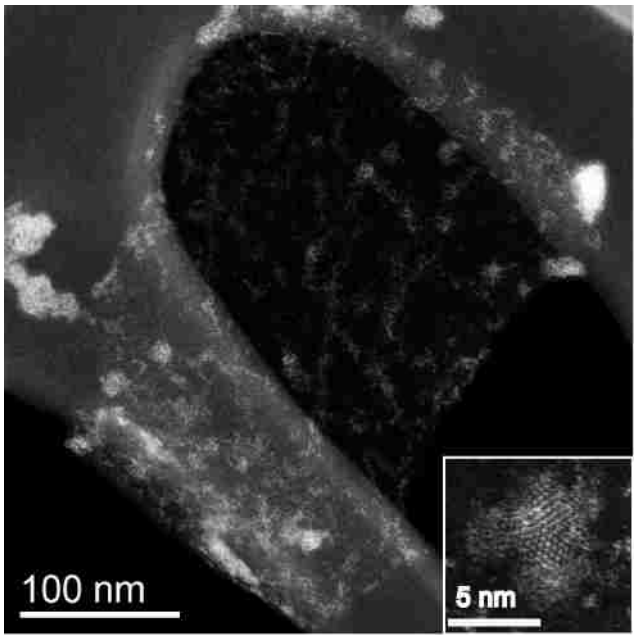

Figure 5.4: HRTEM of graphene sheet showing CdS QD attachment. Inset shows the high resolution image of a single CdS nanocrystal.

Photocatalytic activity of the rGO-CdS QD conjugates were evaluated using visible light irradiation in a photoreactor without the presence of a co-catalyst or sacrificial reagent. Figure 5.5 shows a representative plot of H_2 generation vs irradiation time for rGO-QD, CdS QDs only, and rGO only. The H_2 generation rate is pseudo first order, consistent with expected performance of a stable photocatalyst.[141] For the sample with CdS QDs only, a decrease in H_2 generation is observed after 4 hours. This is indicative of agglomeration of the QDs, which typically occurs when CdS QDs are used as the sole component.[142] In our experiments, rGO was not capable of generating hydrogen without the addition of CdS QDs. While there are some reports of photoactivity with rGO alone, the degree of reduction has been shown to be important to modifying the bandgap such that light can be harvested effectively.[124]

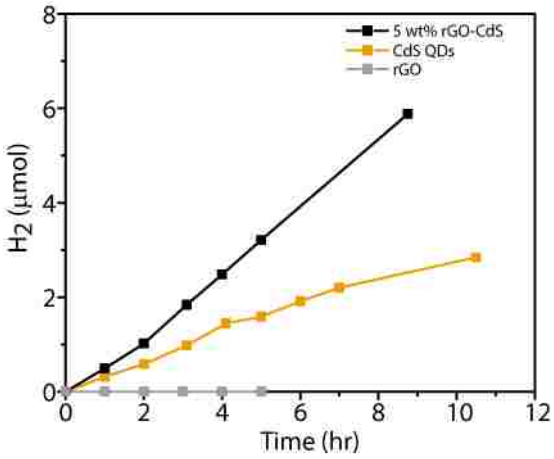

Figure 5.5: H_2 concentration vs time data for rGO-CdS, CdS, and rGO only.

5.3 Discussion

The proposed mechanism of improved GO reduction using CSE is by the presence of H_2S in solution that has been enzymatically produced from L-cysteine. This theory is indirectly confirmed by the lack of reduction when GO is incubated with CSE alone, and the known ability of H_2S production by the class of enzymes cystathionine γ-lyase.[138] While L-cysteine is capable of reducing GO on its own, the presence of H_2S as an extremely strong reducing agent enhances the process yielding a more complete reduction in a similar amount of time. The rGO retains solubility while regaining sp^2 hybridization of the C-C bonds, as indicated by the absorbance peak shift from 230 nm to 270 nm. This result is comparable to the absorbance peak shift when GO is reduced using $NaBH_4$ at 70 °C for 2 hours (Figure 5.7).

The restoration of these graphene domains is further confirmed by the change in intensity ratio between the D peak and G peak at ∼1340 cm^{-1} and ∼1580 cm^{-1}, respectively. The D band, or disorder induced band, appears after oxidation and is

inversely scaled to the amount of graphitic domains.[143] The D band intensity can be quantitatively compared to the G band, and used to determine the number of graphitic domains; an increase in D/G intensity indicates a larger number graphitic domains. FTIR analysis demonstrates the presence and removal of oxygen on GO and rGO, respectively. Peaks corresponding to C-O (1180, 1058 cm^{-1}) and C=O (1733 cm^{-1}) are likely found on the surface and edges of GO sheets. As GO is reduced, these peaks disappear, indicating the loss of most of the oxygen groups on the surface.[140] The large peak at 3450 cm^{-1} indicates the presence of OH. It is possible these OH groups are attached to carbon on the surface, however we cannot rule out the possibility that they result from water intercalated on the dried GO.[144] This peak is decreased for the reduced GO samples, indicating that some of the water or OH bonding on the surface is lost. An additional peak at 1620 cm^{-1}, found in both FTIR spectra, indicates C-C bonding within the graphene sheets.[140]

The binding of PLL onto the surface of rGO will also cause some additional peaks in the FTIR spectrum. Specifically, the peaks at 3271 cm^{-1} (N-H vibration), 1624 and 1533 cm^{-1} (Fermi resonance from N-H deformation), 1314 cm^{-1} (C-N aromatic ring binding) are all found in the FTIR spectra recorded for rGO reduce by both CSE and $NaBH_4$.[145] Incubation of GO with PLL prior to reduction allows adequate time for functionalization of the rGO surface with PLL. The absorbance spectra of GO mixed with PLL was measured following incubation to confirm reduction had not occurred prior to the introduction of CSE and L-cysteine. GO can be reduced by CSE and L-cysteine without the presence of PLL, as cysteine can act as both a reducing agent and as functional group on the surface of GO. However, following incubation with CSE and L-cysteine, the rGO had precipitated and was not able to be resuspended

even with sonication.

The conjugation of QDs to rGO using PLL has been demonstrated previously and applied for various applications such as fluorescent probes and cancer therapy agents.[1, 146] PLL is similar to serine proteins and capable of binding to rGO.[147] In comparison to a protein, PLL is a much shorter peptide, improving the transfer of electrons into rGO.[146] The successful conjugation of CdS QDs to rGO in our experiments was confirmed by washing the CdS-rGO composites with DI water and checking for the presence of adhered QDs. As the CdS QDs were able to withstand centrifugation and resuspension using both vortexing and sonication, they are most likely bound to the surface by PLL as opposed to physisorption. Following conjugation to rGO, the CdS QD peak did not shift with time, indicating that the CdS QDs had retained their size and did not aggregate. TEM analysis further demonstrates the dispersion of CdS nanocrystals on the rGO sheets following washing. The absence of CdS QDs on areas of the carbon grid that do not contain rGO confirms that they are attached and not drying onto rGO during TEM sample preparation.

The photocatalytic activity of CdS QDs suspended in solution alone is low compared to previously reported values. Additionally, the rate does decrease at long photoreaction times due to aggregation of CdS QDs in solution. Once the CdS QDs agglomerate, less surfaces are available for the photoreaction to occur. Also, aggregation increases the number of trap-states, increasing the probability of recombination of the exciton pair as opposed to being used for the water splitting reaction.[125] Once the CdS QDs are bound to rGO, this decrease is not observed at long times. This further confirms the strong binding of QDs to rGO by PLL. As expected, increasing rGO improves the hydrogen generation rate. This may be due to increased graphene

surface area, and improved dispersion of CdS QDs on graphene.[125]

Typically, sacrificial reagents, such as sodium sulfide electrolytes or alcohols, are utilized during photocatalysis to prevent photocorrosion of the CdS nanocrystals. These reagents act as electron donors and recombine with the photogenerated holes to prevent the formation of oxygen close to the catalyst's surface. However, sacrificial reagents artificially increase the H_2 production as a result of the electron accepting pathway that prevents oxidation.[148] Our rates are lower than expected due to the absence of a sacrificial reagent; however, the H_2 produced is truly from water splitting alone and not a result of another pathway.

One final additional component is the use of a co-catalyst. Typically, Pt nanoparticles are used because they have been shown to have high catalytic activity for water splitting. However, using a precious metal such as Pt increases the cost of the photocatalyst, introducing higher cost to an otherwise low-cost product.[149] However, the use of a co-catalyst may be necessary to produce a photocatalyst with efficiencies high enough for commercial use. Another possible low-cost co-catalyst is NiS or Ni_h.[150] Future work will aim to optimize a co-catalyst with our current low-cost photocatalytic system to improve efficiency.

5.4 Conclusions

The paper demonstrates the first use of a single enzyme for the synthesis of both CdS nanocrystals and reduced graphene oxide, which were then combined to form an active photocatalyst for H_2 generation. In both cases, synthesis occurs due to the presence of H_2S enzymatically generated from L-cysteine by CSE. Reduction of GO occurs in as little as 4 hours due to the strong reducing power of H_2S. CdS

nanocrystals are formed through the reaction of Cd acetate and H_2S in solution and stabilized by excess L-cysteine in solution. The as synthesized CdS quantum dots are conjugated to rGO through PLL crosslinkers using a simple incubation method. The CdS-rGO conjugates show improved H_2 generation over biomineralized CdS quantum dots alone due to the presence of rGO, most likely improving light absorption, nanocrystal stability, and the active surface area for photocatalytic reactions. The efficiency of the CdS-rGO photocatalysts could be improved in the future by incorporation of a co-catalyst, such as Ni_h.

5.5 Supplementary Information

The following information is provided as supplementary information for the results presented in Section 5.2.

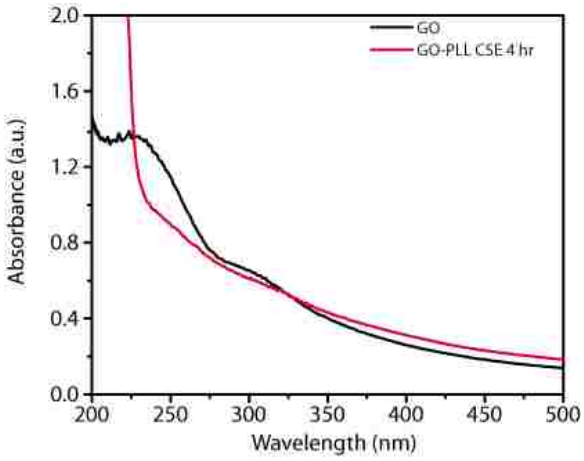

Figure 5.6: GO-PLL incubated with only CSE over 4 hours showing no reduction. A small peak shift may be due to functionalization by PLL and background absorbance from the added CSE solution.

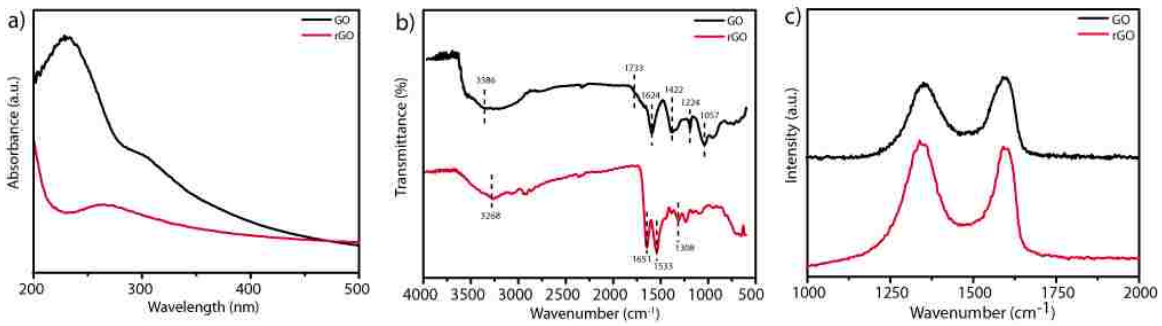

Figure 5.7: Absorbance, FTIR, Raman comparing GO and rGO reduced by $NaBH_4$ following the procedure by Shan *et al.*[1]

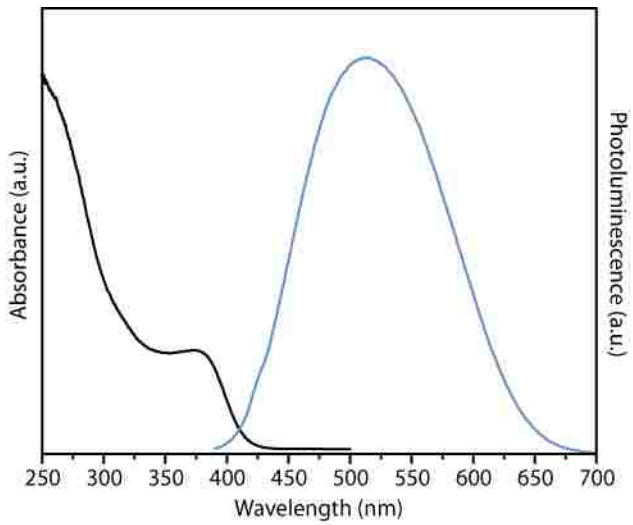

Figure 5.8: Absorbance photoluminescence of typical CdS QDs biomineralized by CSE and utilized for assembly of the rGO-CdS conjugate photocatalysts.

Chapter 6

Elucidating the Growth Mechanism of Quantum Dot Biomineralization by Single Enzyme Cystathionine γ-Lyase

6.1 Introduction

The ability of the single enzyme Cystathionine-γ lyase (CSE) to synthesize several types of metal sulfides and metal selenide nanoparticles has been demonstrated in Chapters 3-5 and in previous work performed by other members of our group. [36, 151, 152] Our previous work proposed that CdS is formed by the reaction of Cd acetate in solution with H_2S, generated from the enzymatic turnover of L-cysteine by CSE. Bulk precipitation of CdS is prevented by the presence of cysteine in solution,

which acts a capping agent.[36] We were able to demonstrate the capping ability of L-cysteine in the formation of one size of CdS nanocrystals by mixing Cd acetate and reactive sulfur precursor NaHS in the presence of L-cysteine. Despite our understanding of CdS synthesis and stabilization in solution, we were not able to explain the mechanism for size control observed during enzymatic synthesis. This chapter aims to study nanocrystal synthesis by CSE in the context of the classical theory for nanocrystal growth to better understand the parameters effecting the growth behavior of enzymatically synthesized quantum dots.

A closer examination of nanocrystal formation and growth requires an understanding of the classical theory for formation of a colloidal particle in solution. The most widely followed model for nanocrystal synthesis, proposed by LaMer *et al.*, theorizes that colloidal particle formation occurs in three stages; monomer accumulation, nucleation, and growth.[153] In most traditional nanocrystal syntheses, monomers are added rapidly to produce an instantaneous oversaturation of monomers, which causes a fast nucleation event followed by slower growth. The kinetics of nucleation are complex, but have been modeled by applying the Gibbs-Thompson equation, which describes how a particle's solubility increases as its size decreases.[154]

$$S_d = S_\infty \exp \frac{4\sigma V_M}{dRT} \tag{6.1}$$

Particle solubility is a function of: S_∞, bulk solubility of the crystal; σ, the surface energy; V_M, the molar volume of the crystal; R, the gas constant; and T, absolute temperature. Nucleation will occur at the point where the chemical potential of a crystal with a certain diameter is equal to the chemical potential of a concentration of monomers at the solubility of the crystal. When nucleation occurs, this corresponds

to a change in the free energy of the system, which can then be used to calculate a critical particle size, above which it is thermodynamically favorable for crystal formation and below which it is unfavorable, i.e., the crystal will dissolve. The full calculation has been performed elsewhere,[154, 155] and results in the critical radius (r_{crit}) as described in equation 6.2.

$$r_{crit} = \frac{8\sigma V_M}{3RT\ln(\omega)} \tag{6.2}$$

In the above equation, ω is the supersaturation, defined as the concentration of monomers over the solubility of a bulk crystal, $\frac{[M]}{S_\infty}$. The size of r_{crit} has a direct effect on the growth rate of nanocrystals in solution. For diffusion controlled growth, the growth rate for a population of nanocrystals in solution is given by equation 6.3.

$$\frac{d(\Delta r)}{dt} = \frac{2\omega V_M D S_\infty}{\bar{r}^2 RT}\left(\frac{1}{\bar{r}} - \frac{1}{r_{crit}}\right) \tag{6.3}$$

In this equation, $\bar{r}$ is the average crystal size, and D is the diffusion constant. There is also a growth equation for reaction limited growth, however, the monomers in our solutions are relatively dilute overall and therefore the diffusion limited case is more appropriate. Based on this equation, when the average particle size is larger than the critical radius, i.e. $\frac{r}{r_{crit}} \geq 1$ the size distribution will narrow, or focus. Once the critical size is larger, $\frac{r}{r_{crit}} < 1$, the size distribution will broaden. Physically, these two cases correspond to two different conditions in solution. In the focusing regime, the monomer concentration is still high enough to diffuse towards the already formed nanocrystals, resulting in overall growth. In this case, the small particles will grow quickly and the larger particles will grow slowly, leading to a narrowing of the

size distribution. Once the concentration of monomers in solution drops, the critical radius increases and particles smaller than this critical radius will dissolve, supplying monomers to the larger particles to continue growth. This effect, known as Ostwald ripening, leads to a broadening of the size distribution as the smaller particles begin to dissolve and only the larger particles continue to grow.

The traditionally used hot-injection method of quantum dot synthesis utilizes a rapid injection of Cd and S precursors in the presence of a capping ligand to create one burst of nucleation followed by controlled crystal growth. The crystal growth typically occurs by Ostwald ripening in the defocusing regime due to rapid consumption of monomers in the nucleation step, leading to a drop in the supersaturation term and an increase in the critical radius. In contrast, our synthesis has continuous CdS monomer addition through the slow enzymatic production of H_2S which reacts with Cd. Therefore, the supersaturation term remains high, the critical radius remains small, and size focusing is expected.

There have been a few similar reports of aqueous CdS synthesis that utilize slow sulfur introduction by decomposing sulfur precursors such as thiourea or MPA at high temperatures (100-200 °C) and pressures.[156] While the slow introduction of sulfur is similar to our synthesis method, the use of heat will alter the growth kinetics and mineralization of the resultant nanocrystals as compared to our room temperature synthesis. Several groups have demonstrated the mineralization of CdS nanocrystals at room temperature through the addition of Cd and a reactive sulfur source, such as Na_2S in the presence of capping agents such as TGA, MPA, or short chain peptides.[156, 33, 34] However, size control is only obtainable by altering the capping

agent; otherwise, a broad size distribution is obtained, resulting in a reduction quantum dot quality unless post-processing steps, such as size exclusion chromatography, are used.

This chapter demonstrates how the slow generation of H_2S by CSE, and thus retention of supersaturation of monomers in solution. This allows the production of uniform size distributions of quantum dots at room temperature by changing dwell time. By employing the reactive precursor sodium hydrosulfide (NaHS), we are able to remove CSE from the synthesis and control the concentration and timing of monomer formation in solution. This allows us to study the growth of nanoparticles with and without constant replenishment of monomers. We also examine the effect of precursor concentration and solution pH on the enzymatic synthesis and discuss these results in terms of the classical nucleation and growth theory presented above.

6.2 Results

Incubation of Cd acetate, L-cysteine, and CSE in Tris buffer at pH 7.5 produces solutions with absorbance and photoluminescence spectra consistent with the formation of CdS quantum dots with sizes between 2-4 nm, Figure 6.1. The proposed mechanism of synthesis by CSE is the enzymatic turnover of L-cysteine to H_2S, a known function of this class of enzymes. H_2S then reacts with any present metal in solution, such as Cd. L-cysteine must be present in elevated levels as it also acts as a capping agent.

In order to study the difference in growth kinetics during our enzymatic synthesis, we employed a chemical synthesis approach to mimic enzymatic growth. By utilizing the precursor sodium sulfide, NaHS, we are able to control the concentration of HS^-

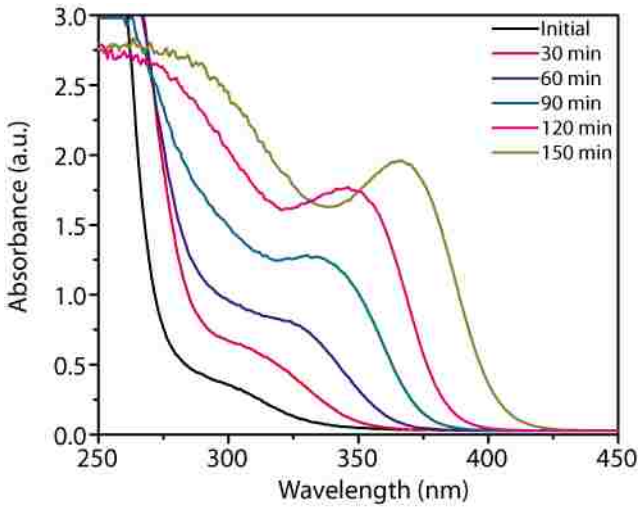

Figure 6.1: Typical absorbance spectra for CdS quantum dots synthesized using the single enzyme CSE.

in solution relative to cadmium acetate and L-cysteine. We are also able to control the timing of NaHS addition; i.e. added at one time, or added slowly over time during synthesis. The temperature was kept at room temperature or 37 °C, and the other precursor concentrations and buffers were the same as used for enzymatic synthesis.

We first studied CdS nanocrystal synthesis when NaHS was rapidly added at one time at the beginning of our synthesis. The amount of NaHS added was determined by estimating the amount of H_2S typically evolved by CSE over a synthesis time of 2 hours using the AzMC assay, which gives a quantitative value for the concentration of H_2S in solution (Figure 6.6). Figure 6.2 shows the absorbance spectra of the CdS quantum dots formed in solution as a function of total NaHS added for two cases; immediately following NaHS addition (Figure 6.2 a) and after 2 hours of solution incubation at 37 °C (Figure 6.2 b).

At very low concentrations, NaHS$\leq$100 μM, the initial absorbance spectra had a

single peak at 300 nm. The solution synthesized with 200 μM NaHS has a peak around 300 nm, but also a broad tail. For the solution at 300 μM, the initial absorbance peak was 330 nm. These absorbance peaks are extremely blue-shifted from the bulk absorbance peak of CdS, indicating very small particle size. Following incubation, the solution with a starting concentration of 100 μM had a final CdS cluster size of 330 nm. At other time points during incubation, no clusters with sizes between these two peaks were noted (Figure 6.7). This indicates that at these low concentrations, CdS nanocrystals may be growing by coalescence.[157] The solution with a starting concentration of 200 μM also has a main peak at 330 nm, but a smaller shoulder at 350 nm also appeared. Again, no other peaks were noticed between these two points, indicating growth by coalescence. For solutions with NaHS $>$ 300 μM, a more continuous shift in absorbance peak (350-360 nm) is observed. At these sizes, it is likely the nanocrystals are growing by classical Ostwald ripening in the size focusing regime. This indicates that the critical radius remains smaller than the average crystallite size under these growth conditions.

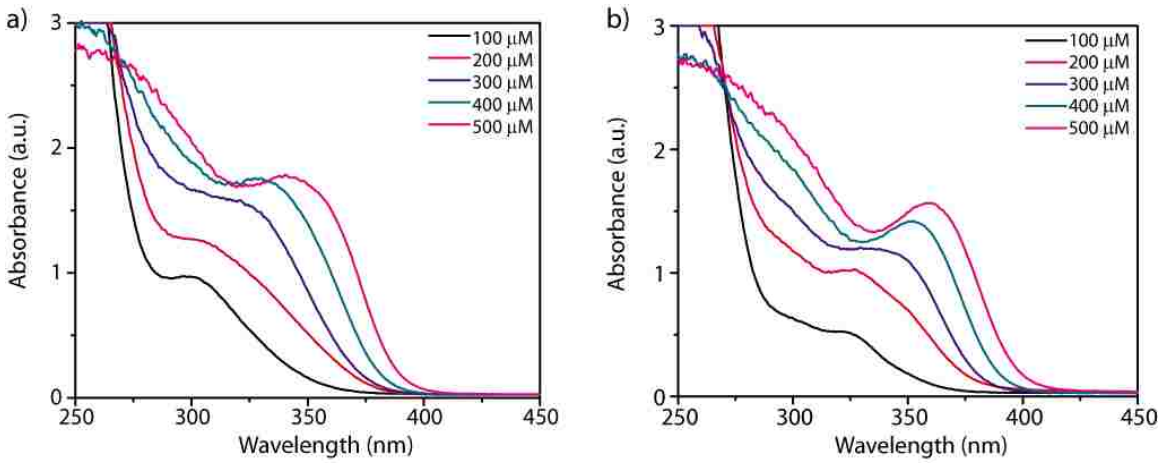

Figure 6.2: The absorbance spectra for solutions of CdS clusters formed by rapid addition of NaHS a) immediately after mixing and b) following 2 hours of incubation at 37 °C.

To demonstrate the effect of constant introduction of H_2S to solution, we altered our chemical synthesis procedure and added the NaHS in 2 μM increments over 2 hours to a final concentration of 500 μM, as opposed to adding it rapidly at once. Figure 6.3 shows the absorbance spectra recorded at 20 μM NaHS increments. In contrast to Figure 6.2, the absorbance peak shifts continuously, indicating that growth is occurring by the addition of monomers. Additionally, the absorbance intensity increases over time, indicating an increase in overall particle concentration during growth.

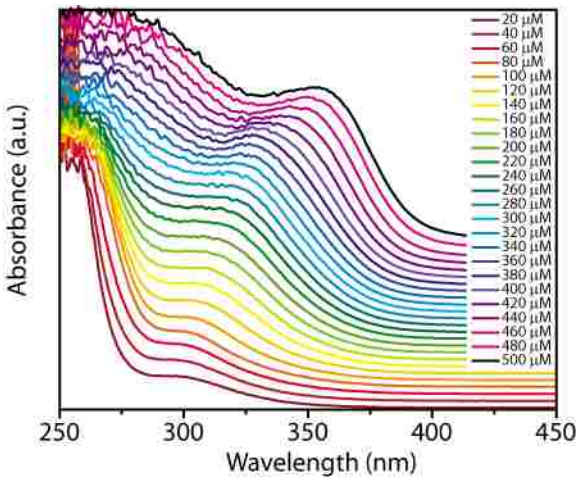

Figure 6.3: Absorbance spectra recorded after the stepwise addition of 20 μM NaHS for a solution of 1 mM Cd and 8 mM cysteine in 0.1 Tris buffer, pH 7.5.

The effect of supersaturation on critical radius and nanocrystal growth can also be observed during CdS mineralization by CSE. Figure 6.4 demonstrates the difference in absorbance and photoluminescence spectra of CdS nanocrystals synthesized for 2 hours with various cadmium acetate and L-cysteine concentrations using 0.05 mg/mL CSE. As demonstrated in both sets of data, using an elevated cadmium concentration results in the formation of a higher concentration of smaller CdS nanocrystals, indicated by a blue-shift in absorbance peak and increase in absorbance intensity relative to the typical growth conditions. Increasing the amount of L-cysteine in solution has no effect on the change observed with increased Cd concentration. This same phenomenon was also demonstrated by Priyam et al., who saw the formation of smaller CdS nanocrystals with tighter size distributions at high cadmium concentrations independent of L-cysteine concentration under similar synthesis conditions.[157]

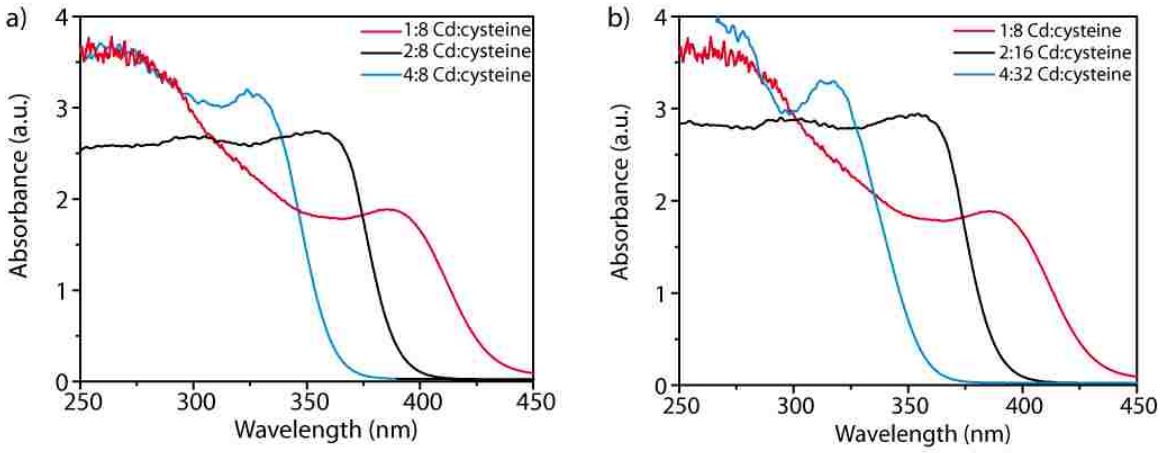

Figure 6.4: Absorbance and photoluminescence spectra of CdS nanocrystal solutions synthesized at pH 7.5 with 0.025 mg/mL CSE for 2 hours for a) varied and b) the same Cd:L-cysteine ratios.

Figure 6.5 shows the absorbance and photoluminescence spectra as a function of time for CdS nanocrystals synthesized enzymatically in Tris buffer pH 9. At pH 7.5, the CdS nanocrystals typically have an absorbance peak range of 330-390 nm (Figure 6.1). At pH 9, the CdS nanoparticle peak range is reduced to between 370-390 nm. However, the CdS nanocrystals formed at pH 9 are stable for at least 2 weeks at 4 °C, whereas those produced at pH 7.5 are only stable for 1-3 days. This indicates that stronger binding of L-cysteine to the particles alters growth, but improves capping of the particles and thus stability following growth.

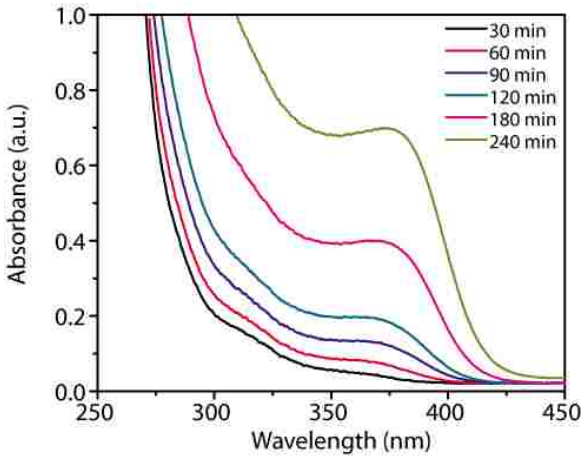

Figure 6.5: Absorbance and photoluminescence spectra of a solution of CdS quantum dots synthesized from 1 mM Cd, 8 mM L-cysteine, 0.04 mg/mL CSE in pH 9 Tris buffer.

6.3 Discussion

The absorbance spectra corresponding to CdS nanocrystals grown by CSE (Figure 6.1) are best approximated by the results of chemical synthesis shown in Figure 6.3. The constant addition of NaHS to solution yields the formation of CdS nanocrystals with an average size that shifts continuously. We believe this continuous shift is a result of a sustained concentration of monomers, provided by the enzymatic turnover of L-cysteine to H_2S. This allows growth to proceed by monomer addition at all times during synthesis. In relation to the theory presented in equation 6.2 and 6.3, a high monomer concentration will result in a high supersaturation term. This yields a small critical radius for nanocrystals in solution, driving the growth behavior to be size focusing.

The results in Figure 6.2 also show size focusing behavior during growth for nanocrystals synthesized with NaHS concentrations greater than or equal to 300 μM. These particles have starting sizes corresponding to an absorbance peak of 330-340 nm, and show continuous peak shifting over 2 hours of ripening at 37 °C. However, particle growth for nanocrystals with starting NaHS concentration 200 μM or less do not demonstrate this same continuous peak shift. Instead, the starting absorbance peak of 300 nm shifts to a peak at 330 nm. Vossmeyer *et al.* observed the same absorbance peaks at 300 and 330 nm for CdS nanocrystal synthesis under analogous synthesis conditions and proposed these peaks corresponded to small CdS clusters with an approximate size of 0.7 nm and 0.9 nm respectively.[158] They also only observed growth to distinct peak values of 330 nm and 350 nm, as opposed to a continuous shift of absorbance peak. They proposed that this indicates growth by coalescence. This result confirms our theory of coalescence for this type of chemical

synthesis; however, this is not the type of growth observed during our enzymatic synthesis.

Another difference between direct NaHS addition (Figure 6.2) and titration (Figure 6.3) are higher absorbance intensities for CdS quantum dots made using titration for the same NaHS concentration. This indicates that CdS clusters continue to be nucleated in addition to growth of preexisting clusters. The total volume of CdS in solution for the absorbance spectra at each NaHS concentration for Figure 6.2 and Figure 6.3 can be calculated by determining the concentration of nanocrystals from the absorbance intensity and multiplying it by the average nanocrystal volume. The concentrations were calculated based on the size dependent relation reported by Yu *et al.*[159] All the calculated volumes are presented in Table 6.1 and Table 6.2. As an example, the volume for the CdS nanocrystals grown by direct addition of 500 μM NaHS is approximately 5.57 $\times 10^{-3}$ nm^3 , while the titrated sample has a total volume of 8.23 $\times 10^{-3}$ nm^3. This increase in volume for the titrated sample was noticed for all absorbance spectra, reported in Table 6.1. This indicates that while most monomers are used for crystal growth, the nucleation of small clusters will still occur and then grow quickly in solution. Another interesting observation for the calculated crystal volume in Table 6.1 is the retention of volume before and after ripening for the direct addition chemical synthesis. This indicates that a majority of particles or clusters are nucleated at the initial time measurement, and then reform into larger particles by coalescence or Ostwald ripening following incubation. While the concentration of particles may decrease, the overall size increases, resulting in a preservation of overall CdS crystal volume.

The results presented in both Figure 6.2 and 6.3 demonstrate the effect of total

CdS concentration on the equilibrium nanocrystal size in solution. As the relative amount of NaHS to Cd was increased, the average nanocrystal size increased, as evidenced by a red-shift of the absorbance peak in solution. In the case of NaHS titration, the addition of monomers is slow and consistent. As the monomers are introduced, they are consumed quickly, balancing the supersaturation condition and leading to continuous growth. However, for direct addition of NaHS, a burst of monomers is introduced in solution and then consumed to create particles. Xie *et al.* have shown that the rapid change in monomer concentration during synthesis makes the application of classical nucleation theory inappropriate in this case.[154] It is more likely that the nucleation occurs in a reaction controlled regime, where the interactions between L-cysteine, Cd monomers, and small Cd-S clusters are competing.

So far we have assumed supersaturation occurs when monomers are introduced in solution and nanocrystal formation results. However, quantifying the degree of supersaturation, ω, allows for a better understanding of the effect of monomer concentration on the critical radius. ω can be calculated by dividing the monomer concentration by S_∞, or bulk crystal solubility. S_∞ can be calculated in terms of the anion species [HS^-] to allow a simple calculation of supersaturation given the generation of HS^- in solution. The solubility of the bulk crystal would traditionally be calculated using K_{sp} for CdS. However, the presence of ligands in solution will affect the solubility and must also be considered, yielding a new solubility constant, K_{obs}. This was calculated following the procedure of Xie *et al.*, shown in supplemental information. Based on the calculation for our system, $S_\infty = 0.047$ μM in terms of HS^- for a Cd concentration of 1 mM. In water, H_2S will dissociate into HS^- and H^+. This dissociation is favorable at pH > 7, and any H_2S in solution will completely dissociate; thus [H_2S] = [HS^-].[160]

Based on this result, any concentration of H_2S in solution which is greater than 0.047 uM will result in nucleation. This is well below our estimated the concentration of H_2S generated by CSE, 4 μM/min.

Another key value of interest is the critical radius corresponding to a specific degree of supersaturation. Several groups have demonstrated that the term $\frac{2\sigma V_M}{3RT}$ is typically ≤ 1 for diffusion controlled conditions.[156, 154] The low bulk solubility will result in a high supersaturation term, which tends to dominate the r_{crit} calculation.[161, 157] Using S_∞ calculated previously, we can estimate that for our system in the presence of 1 mM cadmium acetate at pH 7.5, r_{crit} will range from 0.58 nm for the case of 100 μM NaHS to 0.30 nm for 500 μM NaHS. These results indicate the reintroduction of monomers, even at low levels such as 100 μM NaHS, result in a critical radius much smaller than the average particle size, allowing growth to occur in the size focusing regime.

Following the study of chemical synthesis, we found that altering supersaturation during CdS nanocrystal synthesis by CSE also resulted in a change to the nanocrystal growth. This was achieved by increasing the amount of cadmium in solution as the amount of sulfur generated enzymatically cannot be well controlled. Figure 6.4 demonstrates that increasing the cadmium concentration by either two or found times results in the growth of a large number of particles at a much smaller size over the same amount of time. In context of equations 6.2 and 6.3, the supersaturation of monomers would also be 2 or 4 times as large for the same HS^- concentration. Given a NaHS concentration of 100 μM, this corresponds to a critical radius of 0.41 and 0.32 for 2 mM Cd and 4 mM Cd, respectively. These smaller critical radius values will drive the average radius to tend towards smaller values over time, resulting in

the nucelation of smaller particles.

As L-cysteine plays two roles in synthesis, we thought that increasing L-cysteine would change both the rate of synthesis and the chelation of cadmium during synthesis and capping of the particles. We found that increasing L-cysteine did not have a large impact on growth when the overall cadmium concentration was kept the same; mainly, the rate of nanocrystal synthesis was slightly accelerated due to higher L-cysteine availability for turnover by CSE. Based on our results, CSE appears to be the limiting factor in the turnover of H_2S as this increase is not dramatic. We also found that the ratio of L-cysteine to cadmium did not have a large effect on growth. However, at a ratio of Cd:cysteine less that 1:2, CdS precipitation is noticed. This suggests that a minimum amount of L-cysteine is required to stabilize both cadmium and cadmium sulfide in solution.

The effect of L-cysteine chelation does play a role in synthesis when the overall pH of the solution is altered. Figure 6.5 demonstrates that CdS nanocrystals synthesized at pH 9 grow to a much larger initial size and also have a more restricted size window of growth. This change most likely has to do with the interaction between cadmium and L-cysteine. L-cysteine is an amino acid with three side groups, each with its own pKa value; amine, carboxylic acid, and thiol, with pKa values of 8.7, 7.5, and 5.4 respectively. When the pH is above each pKa value, the side group will become deprotonated and more likely to bind cadmium. Therefore, depending on the pH, L-cysteine will have a different chelating structure with the respective metal.[162] This change in chelating strength as a function of pH affects the final size of the CdS nanocrystals by changing the surface energy term in equations 6.2 and 6.3. Given the complexity of calculating surface energy, we are not able to quantify this change.

However, the effect is clearly seen in the absorbance spectra for the CdS quantum dots formed in Figure 6.5. An additional term that may be affected in equation 6.2 is the bulk solubility, which is dependent on the K_a of all possible Cd-cys complexes in solution. However, this change would not be as significant as the change in surface energy of the crystals.

L-cysteine plays a major role in allowing growth of the CdS nanocrystals by binding strongly enough to prevent aggregation, but weakly enough to allow growth of the nanoparticles. This moderate binding strength is advantageous for our synthesis because it allows us to achieve size control of the CdS nanocrystals. However, it is unfavorable over long times due to the lack of stability of L-cysteine in solution. Over time, L-cysteine will form the dimer L-cystine, which is insoluble in solution. As the overall L-cysteine concentration drops, the CdS nanocrystals will begin to precipitate out of solution. The effect is noticed more rapidly at pH 7.5 than at pH 9 as binding is not as strong at a lower pH. Therefore, L-cysteine is good choice for nanocrystal growth, but does not allow long term stability. Alternative thiol capping agents, such as mercaptopropionic acid (MPA), have been shown to have better long term stability for aqueous Cd chalcogenide quantum dots. However, its use in our aqueous synthesis has been shown to slow down growth dramatically, and over 24 hours are required to form any nanocrystals in solution at 37 °C. Additionally, it is difficult to achieve larger sized particles due to the strength of capping.

6.4 Conclusions

This chapter has discussed the mechanism for CdS nanocrystal nucelation and growth by the single enzyme CSE. Nucleation occurs when H_2S is produced by the enzymatic turnover of L-cysteine in solution. Bulk precipitation is prevented in solution by the presence of L-cysteine. The typical evolution of enzymatically produced nanocrystal populations is best modeled using a stepwise addition of NaHS to a cadmium precursor solution in the presence of L-cysteine. The conditions used in our synthesis result in a high supersaturation of monomer in solution which is sustained during growth, producing a critical radius on the order of 0.3-0.6 nm. When the critical radius is smaller than the average nanocrystal size, size focusing behavior is observed. The degree of supersaturation can also be increased during enzymatic synthesis by increasing the total amount of cadmium in solution. This results in the formation of a higher concentration of smaller particles over the same amount of growth time. Finally, the effect on nanocrystal synthesis by altering the capping agent is examined by raising the pH and thus increasing overall binding strength of L-cysteine to cadmium. This results in the formation of larger, more stable particles that have a slower rate of growth.

6.5 Supplemental Information

The following information is provided as supplementary information for the results presented in Section 6.2.

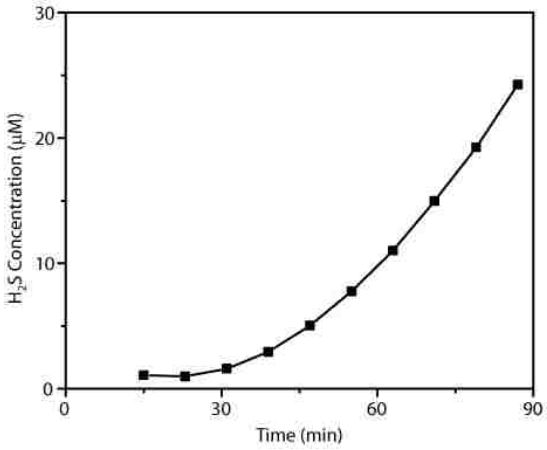

Figure 6.6: H_2S concentration in solution as a function of incubation time from a solution of 0.015 mg/mL CSE and 2.5 mM L-cysteine in activity buffer (pH 8).[2]

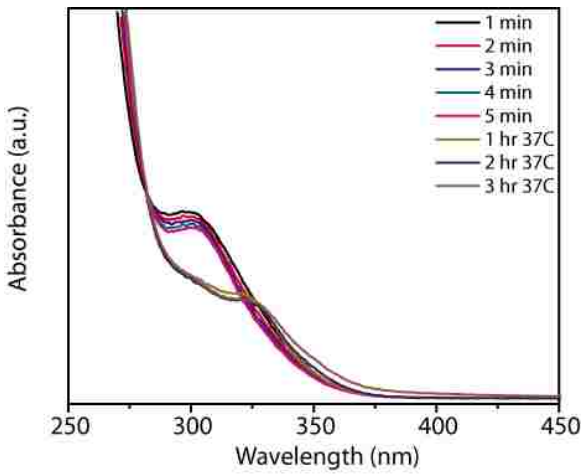

Figure 6.7: Absorbance spectra as a function of time for a solution of 1 mM Cd, 100 μM NaHS, and 8 mM cysteine in 0.1 M Tris buffer at pH 7.5 following rapid addition of NaHS and ripening at 37°C. The initial 5 minutes at room temperature are shown to demonstrate the changes at room temperature are very slow.

Table 6.1: The calculated total volumes for the nanocrystals shown in Figure 6.2, both before and after ripening at 37 °C.

NaHS Concentration (uM)	CdS volume (nm^3)
100 initial	2.15E-03
100 2 hr	1.41E-03
200 initial	2.93E-03
200 2 hr	2.93E-03
300 initial	4.33E-03
300 2 hr	3.54E-03
400 initial	4.95E-03
400 2 hr	4.70E-03
500 initial	5.46E-03
500 2 hr	5.57E-03

Table 6.2: The calculated total volumes for the nanocrystals shown in Figure 6.3.

NaHS Concentration (uM)	CdS volume (nm^3)
10	9.77E-04
50	1.64E-03
100	2.31E-03
150	3.30E-03
200	4.21E-03
250	4.98E-03
300	5.71E-03
350	6.24E-03
400	6.54E-03
450	7.34E-03
500	8.23E-03

The K_{obs} value used in the calculation of S_∞ was obtained by deriving the observed solubility constant as demonstrated by Xie *et al.*

$$CdS_{bulk} + 2.45Hcys \leftrightarrow 0.45CdH(cys)_2 + 0.1Cd(cys)_2 + 0.45CdH(cys)_3 + HS^- + 0.55H^+ \tag{6.4}$$

Hcys represents a protinated L-cysteine. Each of the possible Cd-cysteine chelation species are shown in the above equation: $CdH(cys)_2$,$Cd(cys)_2$, and $CdH(cys)_3$. These species and their relative ratios have been acquired from the supplemental information acquired by Jalilehvand *et al.*[162] Given equation 6.4, K_{obs} can be defined.

$$K_{obs} = \frac{[CdH(cys)_2]^{0.45}\,[Cd(cys)_2]^{0.1}\,[CdH(cys)_3]^{0.45}\,[HS^-]\,[H^+]^{0.55}}{[Hcys]^{2.45}} \tag{6.5}$$

Equation 6.5 can be rearranged in terms of the solubility constants for each species to yield a final relation for K_{obs}

$$K_{obs} = \frac{\beta^{0.45}_{CdH(cys)_2}\beta^{0.1}_{Cd(cys)_2}\beta^{0.45}_{CdH(cys)_3}(K_a^{cys})^{2.45}K_{sp}^{CdS\ bulk}}{K_d^{HS^-}} \tag{6.6}$$

Bulk solubility, S_∞, can then be calculated using this new K_{obs} in terms of HS^-.

Chapter 7

Conclusion

The work presented in this dissertation demonstrates the ability of cystathionine γ-lyase (CSE) to biomineralize several types of metal sulfide nanocrystals. These nanocrystals are synthesized in the aqueous phase at room temperature under ambient conditions. The proposed mechanism for metal sulfide synthesis is the reaction between Cd acetate and H_2S, which is generated enzymatically by CSE. The biomineralized nanocrystals are well suited for biological applications, but are capable of being phase transferred to the organic phase is necessary for energy applications.

Chapter 3 presented the detailed synthesis of PbS and PbS/CdS quantum dots using the bacteria *S. maltophilia*. This work demonstrates that although *S. maltophilia* was evolved to have a high cadmium resistance, the same biomineralization pathway was capable of producing PbS quantum dots. The proposed biomineralization pathway was from the extracelluar production of CSE as a response to the high levels of lead acetate in solution. PbS nanocrystal growth continues despite removing *S. maltophilia*, demonstrating enzymatic mineraliztion. The remaining CSE in solution can also be utilized to grow a CdS shell by introduction of Cd acetate following PbS

nanocrystal synthesis. Both PbS and PbS/CdS nanocrystals are phase transferred to the organic phase and utilized as absorbing layers in quantum dot sensitized solar cells.

Chapter 4 demonstrated the single enzyme synthesis of ternary alloy $CuInS_2$, $(CuInZn)S_2$, and $CuInS_2$/ZnS core/shell nanocrystals. In this case, CSE was over-expressed using recombinant *E. coli* and then purified before nanocrystal synthesis. A two step nanocrystal procedure was implemented; first In was incubated in the presence of cysteine and CSE to produce small cysteine stabilized InS^{2-} clusters. Next, either Cu or Cu and Zn simultaneously were added to solution to produce $CuInS_2$ or $(CuInZn)S_2$ respectively. A shell was biomineralized by the addition of Zn and cysteine to a solution of presynthesized $CuInS_2$ nanocrystals. These non-toxic nanocrystals were then conjugated to the IgG antibody and used for fluorescent cell tagging of Thp-1 leukemia cells.

An additional use for CSE besides biomineralization was demonstrated in chapter 5 for the reducing of graphene oxide. The enzymatically generated H_2S is capable of reducing GO to prepare soluble rGO sheets which can then be utilized for CdS-rGO conjugates. While the enzymatically reduced graphene oxide was not yet shown to produce hydrogen in a CdS-rGO system, biomineralized CdS on chemically reduced rGO showed improved H_2 generation compared to biomineralized CdS alone.

The exact mechanism of nanocrystal synthesis by CSE was studied in Chapter 6. By employing classical theoretical modeling of nanocrystal nucleation and growth, an understanding of the size focusing behavior during CdS quantum dot synthesis can be understood. The constant introduction of H_2S in solution retains a concentration of monomers in solution that drives the critical nucleus required for particle stability

to be small. This small critical nucleus also drives the growth behavior to be size focusing, leading to a narrowing of size distributions as opposed to a broadening typically observed during other traditional nanocrystal syntheses. This theory was demonstrated using both a chemical synthesis method to mimic enzymatic synthesis, and by altering typical parameters used during synthesis by CSE.

While the synthesis of many types of quantum dots has been shown, low quantum yields and lack of stability still place limitations on the commercial use of biomineralized semiconductor nanocrystals. Given a better understanding of the nucleation and growth mechanism demonstrated in Chapter 6, alterations to the synthesis procedure may help improve the biomineralized nanocrystals for other systems (PbS, CdSe, $CuInS_2$). For example, altering the synthesis temperature, overall precursor concentrations, or capping ligands could lead to improvements in particle quality and stability.

List of Publications

The presented dissertation was based on the following papers:

Peer-reviewed journal articles

Leah C. Spangler, Roxanne Chu, Li Lu, Christopher J. Kiely, Bryan W. Berger, and Steven McIntosh. "Enzymatic biomineralization of biocompatible $CuInS_2$, $(CuInZn)S_2$ and $CuInS_2$/ZnS core/shell nanocrystals for bioimaging", Nanoscale,2017, 9, 9340-9351

Leah C. Spangler, Li Lu, Christopher J. Kiely, Bryan W. Berger, and Steven McIntosh. "Biomineralization of PbS and PbSCdS coreshell nanocrystals and their application in quantum dot sensitized solar cells," J.Mater. Chem. A, 2016, 4, 6107-6115.

Hasti Majidi, Michael E. Edley, **Leah C. Spangler**, Jason B. Baxter, Tailoring absorber thickness and the absorber-scaffold interface in CdSe-Coated ZnO nanowire extremely thin absorber solar cells, Electrochimica Acta, 2014, 145, 291-299.

Refereed abstracts & talks

Single-enzyme direct biomineralization of metal chalcogenide nanocrystals with tunable optical properties, American Chemical Society (ACS) Spring Meeting, San Francisco, CA, April 2017.

Single-enzyme biomineralization of CuInS*2*/ZnS core/shell quantum dots for bioimaging applications, 2nd Annual Chemical Engineering Graduate Student Symposium, Lehigh University, Bethlehem, PA, Feb. 2017.

Biosynthesis of PbS/CdS core/shell quantum dots, Materials Research Society (MRS) Fall Conference, Boston, MA, Nov. 2015.

Bibliography

[1] Changsheng Shan, Huafeng Yang, Dongxue Han, Qixian Zhang, Ari Ivaska, and Li Niu. Water-soluble graphene covalently functionalized by biocompatible poly-l-lysine. *Langmuir*, 25(20):12030–12033, 2009.

[2] Megan K. Thorson, Tomas Majtan, Jan P. Kraus, and Amy M. Barrios. Identification of cystathionine β -synthase inhibitors using a hydrogen sulfide selective probe. *Angewandte Chemie International Edition*, 52(17):4641–4644, 2013.

[3] Christopher B. Murray, David J. Norris, and Moungi G. Bawendi. Synthesis and characterization of nearly monodisperse CdE (E= sulfur, selenium, tellurium) semiconductor nanocrystallites. *Journal of the American Chemical Society*, 115(19):8706–8715, 1993.

[4] Nikolai Gaponik and Andrey L. Rogach. *Aqueous synthesis of semiconductor nanocrystals*, pages 73–99. Semiconductor Nanocrystal Quantum Dots. Springer, 2008.

[5] Nikolai Gaponik, Dmitri V. Talapin, Andrey L. Rogach, Alexander Eychmller, and Horst Weller. Efficient phase transfer of luminescent thiol-capped nanocrystals: from water to nonpolar organic solvents. *Nano Letters*, 2(8):803–806, 2002.

[6] Stephen Mann. *Biomineralization: principles and concepts in bioinorganic materials chemistry*, volume 5. Oxford University Press, 2001.

[7] Stefan Kudera, Luigi Carbone, Liberato Manna, and Wolfgang J. Parak. *Growth mechanism, shape and composition control of semiconductor nanocrystals*, pages 1–34. Semiconductor nanocrystal quantum dots. Springer, 2008.

[8] Vladimir Lesnyak, Nikolai Gaponik, and Alexander Eychmller. Colloidal semiconductor nanocrystals: the aqueous approach. *Chemical Society Reviews*, 42(7):2905–2929, 2013.

[9] Wolfgang J. Parak, Daniele Gerion, Teresa Pellegrino, Daniela Zanchet, Christine Micheel, Shara C. Williams, Rosanne Boudreau, Mark A. Le Gros, Carolyn A. Larabell, and A. Paul Alivisatos. Biological applications of colloidal nanocrystals. *Nanotechnology*, 14(7):R15, 2003.

[10] Peter Reiss. *Synthesis of semiconductor nanocrystals in organic solvents*, pages 35–72. Semiconductor Nanocrystal Quantum Dots. Springer, 2008.

[11] Bernard Dennis Cullity. Elements of x-ray diffraction. 2001.

[12] Lesley E. Smart and Elaine A. Moore. *Solid state chemistry: an introduction*. CRC press, 2012.

[13] C. Barry Carter and David B. Williams. *Transmission electron microscopy*. Springer-Verlag US, 2009.

[14] F. Bensebaa, C. Durand, A. Aouadou, Ludmila Scoles, X. Du, D. Wang, and Yvon Le Page. A new green synthesis method of $CuInS_2$ and $CuInSe_2$ nanoparticles and their integration into thin films. *Journal of Nanoparticle Research*, 12(5):1897–1903, 2010.

[15] Dawei Deng, Yuqi Chen, Jie Cao, Junmei Tian, Zhiyu Qian, Samuel Achilefu, and Yueqing Gu. High-quality $CuInS_2$/ZnS quantum dots for in vitro and in vivo bioimaging. *Chemistry of Materials*, 24(15):3029–3037, 2012.

[16] Yolanda Justo, Pieter Geiregat, Karen Van Hoecke, Frank Vanhaecke, Celso De Mello Donega, and Zeger Hens. Optical properties of PbS/CdS core/shell quantum dots. *The Journal of Physical Chemistry C*, 117(39):20171–20177, 2013.

[17] Luca De Trizio, Mirko Prato, Alessandro Genovese, Alberto Casu, Mauro Povia, Roberto Simonutti, Marcelo JP Alcocer, Cosimo DAndrea, Francesco Tassone, and Liberato Manna. Strongly fluorescent quaternary CuInZnS nanocrystals prepared from Cu_{1-x} InS_2 nanocrystals by partial cation exchange. *Chemistry of Materials*, 24(12):2400–2406, 2012.

[18] Jeffrey M. Pietryga, Donald J. Werder, Darrick J. Williams, Joanna L. Casson, Richard D. Schaller, Victor I. Klimov, and Jennifer A. Hollingsworth. Utilizing the lability of lead selenide to produce heterostructured nanocrystals with bright, stable infrared emission. *Journal of the American Chemical Society*, 130(14):4879–4885, 2008.

[19] Ludmila Bakueva, Ivan Gorelikov, Sergei Musikhin, Xu Sheng Zhao, Edward H. Sargent, and Eugenia Kumacheva. PbS quantum dots with stable efficient

luminescence in the near-IR spectral range. *Advanced Materials*, 16(11):926–929, 2004.

[20] Matthew Booth, Andrew P. Brown, Stephen D. Evans, and Kevin Critchley. Determining the concentration of $CuInS_2$ quantum dots from the size-dependent molar extinction coefficient. *Chemistry of Materials*, 24(11):2064–2070, 2012.

[21] Liang Li, T. Jean Daou, Isabelle Texier, Tran Thi Kim Chi, Nguyen Quang Liem, and Peter Reiss. Highly luminescent $CuInS_2$/ZnS core/shell nanocrystals: cadmium-free quantum dots for in vivo imaging. *Chemistry of Materials*, 21(12):2422–2429, 2009.

[22] Fabio Nudelman and Nico AJM Sommerdijk. Biomineralization as an inspiration for materials chemistry. *Angewandte Chemie International Edition*, 51(27):6582–6596, 2012.

[23] CT Dameron, RN Reese, RK Mehra, AR Kortan, PJ Carroll, ML Steigerwald, LE Brus, and DR Winge. Biosynthesis of cadmium sulphide quantum semiconductor crystallites. 1989.

[24] A. Alonso, P. Sanchez, and J. L. Martinez. *Stenotrophomonas maltophilia* D457R contains a cluster of genes from gram-positive bacteria involved in antibiotic and heavy metal resistance. *Antimicrobial Agents and Chemotherapy*, 44(7):1778–1782, 2000.

[25] Delphine Pages, Jerome Rose, Sandrine Conrod, Stephane Cuine, Patrick Carrier, Thierry Heulin, and Wafa Achouak. Heavy metal tolerance in *Stenotrophomonas maltophilia*. *PLoS One*, 3(2):e1539, 2008.

[26] Mirne Fauchon, Gilles Lagniel, Jean-Christophe Aude, Luis Lombardia, Pascal Soularue, Cyrille Petat, Grard Marguerie, Andr Sentenac, Michel Werner, and Jean Labarre. Sulfur sparing in the yeast proteome in response to sulfur demand. *Molecular cell*, 9(4):713–723, 2002.

[27] T. Yano, H. Fukamachi, M. Yamamoto, and T. Igarashi. Characterization of L-cysteine desulfhydrase from *Prevotella intermedia*. *Oral microbiology and immunology*, 24(6):485–492, 2009.

[28] HJ Bai, ZM Zhang, Y. Guo, and GE Yang. Biosynthesis of cadmium sulfide nanoparticles by photosynthetic bacteria *Rhodopseudomonas palustris*. *Colloids and surfaces B: Biointerfaces*, 70(1):142–146, 2009.

[29] SR Strzenbaum, M. Hckner, A. Panneerselvam, J. Levitt, JS Bouillard, S. Taniguchi, LA Dailey, R. Ahmad Khanbeigi, EV Rosca, and M. Thanou. Biosynthesis of luminescent quantum dots in an earthworm. *Nature nanotechnology*, 8(1):57–60, 2013.

[30] Lorenzo Berti and Glenn A. Burley. Nucleic acid and nucleotide-mediated synthesis of inorganic nanoparticles. *Nature nanotechnology*, 3(2):81–87, 2008.

[31] Li Gao and Nan Ma. DNA-templated semiconductor nanocrystal growth for controlled DNA packing and gene delivery. *ACS nano*, 6(1):689–695, 2011.

[32] Jos M. Prez-Donoso, Juan P. Monrs, Denisse Bravo, Adam Aguirre, Andrew F. Quest, Igor O. Osorio-Romn, Ricardo F. Aroca, Thomas G. Chasteen, and Claudio C. Vsquez. Biomimetic, mild chemical synthesis of CdTe-GSH quantum dots with improved biocompatibility. *PloS one*, 7(1):e30741, 2012.

[33] Fang Liu, Seung Hyun Kang, Young-In Lee, Yong ho Choa, Ashok Mulchandani, Nosang V. Myung, and Wilfred Chen. Enzyme mediated synthesis of phytochelatin-capped CdS nanocrystals. *Applied Physics Letters*, 97(12):123703, 2010.

[34] Weibin Zhou, Daniel T. Schwartz, and Francois Baneyx. Single-pot biofabrication of zinc sulfide immuno-quantum dots. *Journal of the American Chemical Society*, 132(13):4731–4738, 2010.

[35] Zhou Yang, Li Lu, Victoria F. Berard, Qian He, Christopher J. Kiely, Bryan W. Berger, and Steven McIntosh. Biomanufacturing of CdS quantum dots. *Green Chemistry*, 17(7):3775 –3782, 2015.

[36] R. Dunleavy, L. Lu, C. J. Kiely, S. McIntosh, and B. W. Berger. Single-enzyme biomineralization of cadmium sulfide nanocrystals with controlled optical properties. *Proceedings of the National Academy of Sciences of the United States of America*, 113(19):5275–5280, 2016.

[37] Nina I. Kovtyukhova, Patricia J. Ollivier, Benjamin R. Martin, Thomas E. Mallouk, Sergey A. Chizhik, Eugenia V. Buzaneva, and Alexandr D. Gorchinskiy. Layer-by-layer assembly of ultrathin composite films from micron-sized graphite oxide sheets and polycations. *Chemistry of Materials*, 11(3):771–778, 1999.

[38] Octavi E. Semonin, Justin C. Johnson, Joseph M. Luther, Aaron G. Midgett, Arthur J. Nozik, and Matthew C. Beard. Absolute photoluminescence quantum yields of IR-26 dye, PbS, and PbSe quantum dots. *The Journal of Physical Chemistry Letters*, 1(16):2445–2450, 2010.

[39] Pisist Kumnorkaew, Yik-Khoon Ee, Nelson Tansu, and James F. Gilchrist. Investigation of the deposition of microsphere monolayers for fabrication of microlens arrays. *Langmuir*, 24(21):12150–12157, 2008.

[40] Masilamany Koneswaran and Ramaier Narayanaswamy. L-Cysteine-capped ZnS quantum dots based fluorescence sensor for Cu^2 ion. *Sensors and Actuators B: Chemical*, 139(1):104–109, 2009.

[41] Frank W. Wise. Lead salt quantum dots: the limit of strong quantum confinement. *Accounts of Chemical Research*, 33(11):773–780, 2000.

[42] S. Schmitt-Rink, D. A. B. Miller, and D. S. Chemla. Theory of the linear and nonlinear optical properties of semiconductor microcrystallites. *Physical Review B*, 35(15):8113, 1987.

[43] R. Vogel, P. Hoyer, and H. Weller. Quantum-sized PbS, CdS, Ag_2S, Sb_2S_3, and Bi_2S_3 particles as sensitizers for various nanoporous wide-band gap semiconductors. *The Journal of physical chemistry*, 98(12):3183–3188, 1994.

[44] Randy J. Ellingson, Matthew C. Beard, Justin C. Johnson, Pingrong Yu, Olga I. Micic, Arthur J. Nozik, Andrew Shabaev, and Alexander L. Efros. Highly efficient multiple exciton generation in colloidal PbSe and PbS quantum dots. *Nano letters*, 5(5):865–871, 2005.

[45] Ye Yang, William Rodrguez-Cordoba, and Tianquan Lian. Multiple exciton generation and dissociation in PbS quantum dot-electron acceptor complexes. *Nano letters*, 12(8):4235–4241, 2012.

[46] William Shockley and Hans J. Queisser. Detailed balance limit of efficiency of p-n junction solar cells. *Journal of Applied Physics*, 32(3):510–519, 1961.

[47] MS Neo, N. Venkatram, GS Li, WS Chin, and W. Ji. Synthesis of PbS/CdS core- shell qds and their nonlinear optical properties. *The Journal of Physical Chemistry C*, 114(42):18037–18044, 2010.

[48] Lai-Hung Lai, Loredana Protesescu, Maksym V. Kovalenko, and Maria A. Loi. Sensitized solar cells with colloidal PbS-CdS core-shell quantum dots. *Physical Chemistry Chemical Physics*, 16(2):736–742, 2014.

[49] Guiqiu Chen, Bin Yi, Guangming Zeng, Qiuya Niu, Ming Yan, Anwei Chen, Jianjian Du, Jian Huang, and Qihua Zhang. Facile green extracellular biosynthesis of CdS quantum dots by white rot fungus *Phanerochaete chrysosporium*. *Colloids and Surfaces B: Biointerfaces*, 117:199–205, 2014.

[50] C. Gallardo, JP Monrs, DO Plaza, B. Collao, LA Saona, V. Durn-Toro, FA Venegas, C. Soto, G. Ulloa, and CC Vsquez. Low-temperature biosynthesis of fluorescent semiconductor nanoparticles (CdS) by oxidative stress resistant *Antarctic bacteria*. *Journal of Biotechnology*, 187:108–115, 2014.

[51] D. P. Cunningham and L. L. Lundie Jr. Precipitation of cadmium by *Clostridium thermoaceticum*. *Applied and Environmental Microbiology*, 59(1):7–14, 1993.

[52] Zhao-Xia Cai, Hong Yang, Yi Zhang, and Xiu-Ping Yan. Preparation, characterization and evaluation of water-soluble L-cysteine-capped-cds nanoparticles

as fluorescence probe for detection of Hg (II) in aqueous solution. *Analytica Chimica Acta*, 559(2):234–239, 2006.

[53] Yao hai Zhang, Hua shan Zhang, Xiao feng Guo, and Hong Wang. L-cysteine-coated CdSe/CdS core-shell quantum dots as selective fluorescence probe for copper (II) determination. *Microchemical Journal*, 89(2):142–147, 2008.

[54] Wenhao Liu, Hak Soo Choi, John P. Zimmer, Eiichi Tanaka, John V. Frangioni, and Moungi Bawendi. Compact cysteine-coated CdSe(ZnCdS) quantum dots for in vivo applications. *Journal of the American Chemical Society*, 129(47):14530–14531, 2007.

[55] Yongfen Chen and Zeev Rosenzweig. Luminescent CdS quantum dots as selective ion probes. *Analytical Chemistry*, 74(19):5132–5138, 2002.

[56] Anindita Chatterjee, Amiya Priyam, Satyen K. Das, and Abhijit Saha. Size tunable synthesis of cysteine-capped CdS nanoparticles by γ-irradiation. *Journal of colloid and interface science*, 294(2):334–342, 2006.

[57] Frank CJM van Veggel. Near-infrared quantum dots and their delicate synthesis, challenging characterization, and exciting potential applications. *Chemistry of Materials*, 26(1):111–122, 2013.

[58] XK Zhao, J. Yang, Larry D. McCormick, and JH Fendler. Epitaxial formation of lead sulfide crystals under arachidic acid monolayers. *The Journal of physical chemistry*, 96(24):9933–9939, 1992.

[59] Inuk Kang and Frank W. Wise. Electronic structure and optical properties of PbS and PbSe quantum dots. *JOSA B*, 14(7):1632–1646, 1997.

[60] Iwan Moreels, Karel Lambert, Dries Smeets, David De Muynck, Tom Nollet, Jos C. Martins, Frank Vanhaecke, Andre Vantomme, Christophe Delerue, and Guy Allan. Size-dependent optical properties of colloidal PbS quantum dots. *ACS nano*, 3(10):3023–3030, 2009.

[61] Sachin Seshadri, K. Saranya, and Meenal Kowshik. Green synthesis of lead sulfide nanoparticles by the lead resistant marine yeast, *Rhodosporidium diobovatum*. *Biotechnology progress*, 27(5):1464–1469, 2011.

[62] Hong-Juan Bai and Zhao-Ming Zhang. Microbial synthesis of semiconductor lead sulfide nanoparticles using immobilized *Rhodobacter sphaeroides*. *Materials Letters*, 63(9):764–766, 2009.

[63] Satyajyoti Senapati, Asad Syed, Shadab Khan, Renu Pasricha, M. I. Khan, Rajiv Kumar, and Absar Ahmad. Extracellular biosynthesis of metal sulfide nanoparticles using the *Fungus Fusarium* oxysporum. *Current Nanoscience*, 10(4):588–595, 2014 2014.

[64] Nan Ma, Ann F. Marshall, and Jianghong Rao. Near-infrared light emitting luciferase via biomineralization. *Journal of the American Chemical Society*, 132(20):6884–6885, 2010.

[65] Larissa Levina, Vlad Sukhovatkin, Sergei Musikhin, Sam Cauchi, Rozalia Nisman, David P. Bazett-Jones, and Edward H. Sargent. Efficient infrared-emitting PbS quantum dots grown on DNA and stable in aqueous solution and blood plasma. *Advanced Materials*, 17(15):1854–1857, 2005.

[66] Dawei Deng, Junfei Xia, Jie Cao, Lingzhi Qu, Junmei Tian, Zhiyu Qian, Yueqing Gu, and Zhongze Gu. Forming highly fluorescent near-infrared emitting PbS quantum dots in water using glutathione as surface-modifying molecule. *Journal of colloid and interface science*, 367(1):234–240, 2012.

[67] Margaret A. Hines and Gregory D. Scholes. Colloidal PbS nanocrystals with size-tunable near-infrared emission: observation of post-synthesis self-narrowing of the particle size distribution. *Advanced Materials*, 15(21):1844–1849, 2003.

[68] Mark C. Weidman, Megan E. Beck, Rachel S. Hoffman, Ferry Prins, and William A. Tisdale. Monodisperse, air-stable PbS nanocrystals via precursor stoichiometry control. *ACS nano*, 8(6):6363–6371, 2014.

[69] Iwan Moreels, Yolanda Justo, Bram De Geyter, Katrien Haustraete, Jos C. Martins, and Zeger Hens. Size-tunable, bright, and stable PbS quantum dots: a surface chemistry study. *Acs Nano*, 5(3):2004–2012, 2011.

[70] Geoffrey J. Supran, Katherine W. Song, Gyu Weon Hwang, Raoul E. Correa, Jennifer Scherer, Eric A. Dauler, Yasuhiro Shirasaki, Moungi G. Bawendi, and Vladimir Bulovic. High-performance shortwave-infrared light-emitting devices using core-shell (PbS-CdS) colloidal quantum dots. *Advanced Materials*, 27(8):1437–1442, 2015.

[71] Haiguang Zhao, Mohamed Chaker, Nianqiang Wu, and Dongling Ma. Towards controlled synthesis and better understanding of highly luminescent PbS/CdS core/shell quantum dots. *Journal of Materials Chemistry*, 21(24):8898–8904, 2011.

[72] Jinzhong Niu, Weiwei Xu, Huaibin Shen, Sen Li, Hongzhe Wang, and Lin Song Li. Synthesis of CdS, ZnS, and CdS/ZnS core/shell nanocrystals using dodecanethiol. *Bulletin of the Korean Chemical Society*, 33(2):393–397, 2012.

[73] Maksym V. Kovalenko, Richard D. Schaller, Dorota Jarzab, Maria A. Loi, and Dmitri V. Talapin. Inorganically functionalized PbS-CdS colloidal nanocrystals: Integration into amorphous chalcogenide glass and luminescent properties. *Journal of the American Chemical Society*, 134(5):2457–2460, 2012.

[74] Keith A. Abel, Paul A. FitzGerald, Ting-Yu Wang, Tom Z. Regier, Mati Raudsepp, Simon P. Ringer, Gregory G. Warr, and Frank CJM van Veggel. Probing the structure of colloidal core/shell quantum dots formed by cation exchange. *The Journal of Physical Chemistry C*, 116(6):3968–3978, 2012.

[75] Haiguang Zhao, Hongyan Liang, Francois Vidal, Federico Rosei, Alberto Vomiero, and Dongling Ma. Size dependence of temperature-related optical properties of PbS and PbS/CdS core/shell quantum dots. *The Journal of Physical Chemistry C*, 118(35):20585–20593, 2014.

[76] HS Zhou, I. Honma, H. Komiyama, and Joseph W. Haus. Coated semiconductor nanoparticles; the cadmium sulfide/lead sulfide system's synthesis and properties. *The Journal of physical chemistry*, 97(4):895–901, 1993.

[77] Qianglu Lin, Nikolay S. Makarov, Weon kyu Koh, Kirill A. Velizhanin, Claudiu M. Cirloganu, Hongmei Luo, Victor I. Klimov, and Jeffrey M. Pietryga. Design and synthesis of heterostructured quantum dots with dual emission in the visible and infrared. *ACS nano*, 9(1):539–547, 2014.

[78] Keith A. Abel, Haijun Qiao, Jeff F. Young, and Frank CJM van Veggel. Four-fold enhancement of the activation energy for nonradiative decay of excitons in PbSe/CdSe core/shell versus PbSe colloidal quantum dots. *The Journal of Physical Chemistry Letters*, 1(15):2334–2338, 2010.

[79] Rainer T. Lechner, Gerhard Fritz-Popovski, Maksym Yarema, Wolfgang Heiss, Armin Hoell, Tobias U. Schulli, Daniel Primetzhofer, Martin Eibelhuber, and Oskar Paris. Crystal phase transitions in the shell of PbS/CdS core/shell nanocrystals influences photoluminescence intensity. *Chemistry of Materials*, 26(20):5914–5922, 2014.

[80] MJ Speirs, DM Balazs, H-H Fang, L-H Lai, L. Protesescu, MV Kovalenko, and MA Loi. Origin of the increased open circuit voltage in PbS-CdS core-shell quantum dot solar cells. *Journal of Materials Chemistry A*, 3(4):1450–1457, 2015.

[81] Belete Atomsa Gonfa, Haiguang Zhao, Jiangtian Li, Jingxia Qiu, Menouer Saidani, Shanqing Zhang, Ricardo Izquierdo, Nianqiang Wu, My Ali El Khakani, and Dongling Ma. Air-processed depleted bulk heterojunction solar cells based on PbS/CdS core/shell quantum dots and tio$_2$ nanorod arrays. *Solar Energy Materials and Solar Cells*, 124:67–74, 2014.

[82] Leah C. Spangler, Li Lu, Christopher J. Kiely, Bryan W. Berger, and Steven McIntosh. Biomineralization of PbS and PbSCdS coreshell nanocrystals and their application in quantum dot sensitized solar cells. *Journal of Materials Chemistry A*, 4(16):6107–6115, 2016.

[83] Zhou Yang, Li Lu, Christopher J. Kiely, Bryan W. Berger, and Steven McIntosh. Biomineralized CdS quantum dot nanocrystals: Optimizing synthesis conditions and improving functional properties by surface modification. *Industrial & Engineering Chemistry Research*, 55(43):11235–11244, 2016.

[84] Roshan H. Kore, Jaideep S. Kulkarni, and Santosh K. Haram. Effect of nonionic surfactants on the kinetics of disproportion of copper sulfide nanoparticles in the aqueous sols. *Chemistry of materials*, 13(5):1789–1793, 2001.

[85] Xijian Liu, Bo Li, Fanfan Fu, Kaibing Xu, Rujia Zou, Qian Wang, Bingjie Zhang, Zhigang Chen, and Junqing Hu. Facile synthesis of biocompatible cysteine-coated CuS nanoparticles with high photothermal conversion efficiency for cancer therapy. *Dalton Transactions*, 43(30):11709–11715, 2014.

[86] S. Prasanth, D. Rithesh Raj, TV Vineeshkumar, Riju K. Thomas, and C. Sudarsanakumar. Exploring the interaction of L-cysteine capped CuS nanoparticles with bovine serum albumin (BSA): a spectroscopic study. *RSC Advances*, 6(63):58288–58295, 2016.

[87] Ilka Kriegel, Chengyang Jiang, Jessica Rodrguez-Fernandez, Richard D. Schaller, Dmitri V. Talapin, Enrico Da Como, and Jochen Feldmann. Tuning the excitonic and plasmonic properties of copper chalcogenide nanocrystals. *Journal of the American Chemical Society*, 134(3):1583–1590, 2012.

[88] Yue Wu, Cyrus Wadia, Wanli Ma, Bryce Sadtler, and A. Paul Alivisatos. Synthesis and photovoltaic application of copper (I) sulfide nanocrystals. *Nano letters*, 8(8):2551–2555, 2008.

[89] PN Kumta, Pradeep P. Phule, and Subhash H. Risbud. Low-temperature wet-chemical synthesis of amorphous indium sulfide powders. *Materials Letters*, 5(10):401–404, 1987.

[90] Mariia V. Ivanchenko, Oleksandra E. Rayevska, Oleksandr L. Stroyuk, and Stepan Ya Kuchmiy. Colloidal indium sulfide quantum dots in water: synthesis and optical properties. In *MRS Proceedings*, volume 1617, pages 163–169. Cambridge Univ Press, 2013.

[91] Prashant V. Kamat, Nada M. Dimitrijevic, and Richard W. Fessenden. Photoelectrochemistry in particulate systems. 7. electron-transfer reactions of indium sulfide semiconductor colloids. *J.Phys.Chem.*, 92(8), 1988.

[92] Yoshio Nosaka, Nobuhiro Ohta, and Hajime Miyama. Photochemical kinetics of ultrasmall semiconductor particles in solution: effect of size on the quantum yield of electron transfer. *The Journal of physical chemistry*, 94(9):3753, 1990.

[93] Dattatri K. Nagesha, Xiaorong Liang, Arif A. Mamedov, Gordon Gainer, Margaret A. Eastman, Michael Giersig, Jin-Joo Song, Tong Ni, and Nicholas A. Kotov. In_2S_3 nanocolloids with excitonic emission: In_2S_3 vs CdS comparative study of optical and structural characteristics. *The Journal of Physical Chemistry B*, 105(31):7490–7498, 2001.

[94] CD Lokhande. Chemical deposition of metal chalcogenide thin films. *Materials Chemistry and Physics*, 27(1):1–43, 1991.

[95] Alice DP Leach and Janet E. Macdonald. Optoelectronic properties of $CuInS_2$ nanocrystals and their origin. *The journal of physical chemistry letters*, 7(3):572–583, 2016.

[96] David So and Gerasimos Konstantatos. Thiol-free synthesized copper indium sulfide nanocrystals as optoelectronic quantum dot solids. *Chemistry of Materials*, 27(24):8424–8432, 2015.

[97] Ward Van Der Stam, Anne C. Berends, Freddy T. Rabouw, Tom Willhammar, Xiaoxing Ke, Johannes D. Meeldijk, Sara Bals, and Celso de Mello Donega. Luminescent $CuInS_2$ quantum dots by partial cation exchange in $Cu_{2x}s$ nanocrystals. *Chemistry of Materials*, 27(2):621–628, 2015.

[98] Haizheng Zhong, Yi Zhou, Mingfu Ye, Youjun He, Jianping Ye, Chang He, Chunhe Yang, and Yongfang Li. Controlled synthesis and optical properties of colloidal ternary chalcogenide $CuInS_2$ nanocrystals. *Chemistry of Materials*, 20(20):6434–6443, 2008.

[99] Danilo H. Jara, Seog Joon Yoon, Kevin G. Stamplecoskie, and Prashant V. Kamat. Size-dependent photovoltaic performance of $CuInS_2$ quantum dot-sensitized solar cells. *Chemistry of Materials*, 26(24):7221–7228, 2014.

[100] Yanyan Chen, Shenjie Li, Lijian Huang, and Daocheng Pan. Green and facile synthesis of water-soluble $CuInS_2$/zns core/shell quantum dots. *Inorganic chemistry*, 52(14):7819–7821, 2013.

[101] Young-Kuk Kim, Si-Hyun Ahn, Kookchae Chung, Young-Sang Cho, and Chul-Jin Choi. The photoluminescence of $CuInS_2$ nanocrystals: effect of

non-stoichiometry and surface modification. *Journal of Materials Chemistry*, 22(4):1516–1520, 2012.

[102] Masato Uehara, Kosuke Watanabe, Yasuyuki Tajiri, Hiroyuki Nakamura, and Hideaki Maeda. Synthesis of $CuInS_2$ fluorescent nanocrystals and enhancement of fluorescence by controlling crystal defect. *The Journal of chemical physics*, 129(13):134709, 2008.

[103] Xianliang Wang and Mark T. Swihart. Controlling the size, shape, phase, band gap, and localized surface plasmon resonance of $Cu_{2x}S$ and Cu_xin_yS nanocrystals. *Chemistry of Materials*, 27(5):1786–1791, 2015.

[104] Liang Li, Anshu Pandey, Donald J. Werder, Bishnu P. Khanal, Jeffrey M. Pietryga, and Victor I. Klimov. Efficient synthesis of highly luminescent copper indium sulfide-based core/shell nanocrystals with surprisingly long-lived emission. *Journal of the American Chemical Society*, 133(5):1176–1179, 2011.

[105] Ankita Ghatak, Gouranga H. Debnath, Madhuri Mandal, and Prasun Mukherjee. Lanthanide cation-induced tuning of surface capping properties in zinc sulfide nanoparticles: an infrared absorption study. *RSC Advances*, 5(42):32920–32932, 2015.

[106] Neelesh Kumbhojkar, VV Nikesh, Anjali Kshirsagar, and Shailaja Mahamuni. Photophysical properties of ZnS nanoclusters. *Journal of Applied Physics*, 88(11):6260–6264, 2000.

[107] Lin Song Li, Narayan Pradhan, Yunjun Wang, and Xiaogang Peng. High quality ZnSe and ZnS nanocrystals formed by activating zinc carboxylate precursors. *Nano Letters*, 4(11):2261–2264, 2004.

[108] Siyu Liu, Hao Zhang, Yu Qiao, and Xingguang Su. One-pot synthesis of ternary $CuInS_2$ quantum dots with near-infrared fluorescence in aqueous solution. *Rsc Advances*, 2(3):819–825, 2012.

[109] Thomas Pons, Emilie Pic, Nicolas Lequeux, Elsa Cassette, Lina Bezdetnaya, Franois Guillemin, Frdric Marchal, and Benoit Dubertret. Cadmium-free $CuInS_2$/ZnS quantum dots for sentinel lymph node imaging with reduced toxicity. *ACS nano*, 4(5):2531–2538, 2010.

[110] Tongtong Jiang, Jiangluqi Song, Huijie Wang, Xuecheng Ye, Hao Wang, Wenting Zhang, Mingya Yang, Ruixiang Xia, Lixin Zhu, and Xiaoliang Xu. Aqueous synthesis of color tunable Cu doped ZnInS/ZnS nanoparticles in the whole visible region for cellular imaging. *Journal of Materials Chemistry B*, 3(11):2402–2410, 2015.

[111] Jie Zhang, Renguo Xie, and Wensheng Yang. A simple route for highly luminescent quaternary Cu-Zn-In-S nanocrystal emitters. *Chemistry of Materials*, 23(14):3357–3361, 2011.

[112] Quinten A. Akkerman, Alessandro Genovese, Chandramohan George, Mirko Prato, Iwan Moreels, Alberto Casu, Sergio Marras, Alberto Curcio, Alice Scarpellini, and Teresa Pellegrino. From binary Cu_2S to ternary CuInS and quaternary CuInZnS nanocrystals with tunable composition via partial cation exchange. *ACS nano*, 9(1):521–531, 2015.

[113] Anne C. Berends, Freddy T. Rabouw, Frank CM Spoor, Eva Bladt, Ferdinand C. Grozema, Arjan J. Houtepen, Laurens DA Siebbeles, and Celso de Mello Doneg. Radiative and nonradiative recombination in $CuInS_2$ nanocrystals and $CuInS_2$-based core/shell nanocrystals. *The Journal of Physical Chemistry Letters*, 7(17):3503–3509, 2016.

[114] Shigeru Tsuchiya, Michiko Yamabe, Yoshiko Yamaguchi, Yasuko Kobayashi, Tasuke Konno, and Keiya Tada. Establishment and characterization of a human acute monocytic leukemia cell line (THP-1). *International journal of cancer*, 26(2):171–176, 1980.

[115] B. Mograbi, N. Rochet, V. Imbert, I. Bourget, R. Bocciardi, C. Emiliozzi, and B. Rossi. Human monocytes express amphiregulin and heregulin growth factors upon activation. *European cytokine network*, 8(1):73–81, Mar 1997.

[116] SH Choi, JM Mendrola, and MA Lemmon. Egf-independent activation of cell-surface egf receptors harboring mutations found in gefitinib-sensitive lung cancer. *Oncogene*, 26(11):1567–1576, 2007.

[117] Junya Ichinose, Masayuki Murata, Toshio Yanagida, and Yasushi Sako. EGF signalling amplification induced by dynamic clustering of EGFR. *Biochemical and biophysical research communications*, 324(3):1143–1149, 2004.

[118] Wolfgang J. Parak, Rosanne Boudreau, Mark Le Gros, Daniele Gerion, Daniela Zanchet, Christine M. Micheel, Shara C. Williams, A. Paul Alivisatos, and Carolyn Larabell. Cell motility and metastatic potential studies based on quantum dot imaging of phagokinetic tracks. *Advanced Materials*, 14(12):882–885, 2002.

[119] Neus Feliu, Jonas Hhn, Mikhail V. Zyuzin, Sumaira Ashraf, Daniel Valdeperez, Atif Masood, Alaa Hassan Said, Alberto Escudero, Beatriz Pelaz, and Elena Gonzalez. Quantitative uptake of colloidal particles by cell cultures. *Science of the Total Environment*, 568:819–828, 2016.

[120] Haizheng Zhong, Shun S. Lo, Tihana Mirkovic, Yunchao Li, Yuqin Ding, Yongfang Li, and Gregory D. Scholes. Noninjection gram-scale synthesis of monodisperse pyramidal $CuInS_2$ nanocrystals and their size-dependent properties. *ACS nano*, 4(9):5253–5262, 2010.

[121] Nandanan Erathodiyil and Jackie Y. Ying. Functionalization of inorganic nanoparticles for bioimaging applications. *Accounts of Chemical Research*, 44(10):925–935, 2011.

[122] Akira Fujishima and Kenichi Honda. Electrochemical photolysis of water at a semiconductor electrode. *Nature*, 238(5258):37, 1972.

[123] Yajun Wang, Qisheng Wang, Xueying Zhan, Fengmei Wang, Muhammad Safdar, and Jun He. Visible light driven type II heterostructures and their enhanced photocatalysis properties: a review. *Nanoscale*, 5:8326–8339, 2013.

[124] Guancai Xie, Kai Zhang, Beidou Guo, Qian Liu, Liang Fang, and Jian Ru Gong. Graphene-based materials for hydrogen generation from light-driven water splitting. *Advanced Materials*, 25(28):3820–3839, 2013.

[125] Qin Li, Xin Li, S. Wageh, Ahmed. A. AlGhamdi, and Jiaguo Yu. CdS/graphene nanocomposite photocatalysts. *Advanced Energy Materials*, 5(14):1500010, 2015.

[126] Sasha Stankovich, Dmitriy A. Dikin, Richard D. Piner, Kevin A. Kohlhaas, Alfred Kleinhammes, Yuanyuan Jia, Yue Wu, Son Binh T. Nguyen, and Rodney S. Ruof. Synthesis of graphene-based nanosheets via chemical reduction of exfoliated graphite oxide. *Carbon*, 45(7):1558–1565, 2007.

[127] Jiabin Wang, Elif Caliskan Salihi, and Lidija iller. Green reduction of graphene oxide using alanine. *Materials Science and Engineering: C*, 72:1 – 6, 2017.

[128] Dezhi Chen, Lidong Li, and Lin Guo. An environment-friendly preparation of reduced graphene oxide nanosheets via amino acid. *Nanotechnology*, 22(32):325601, 2011.

[129] Suman Thakur and Niranjan Karak. Green reduction of graphene oxide by aqueous phytoextracts. *Carbon*, 50(14):5331 – 5339, 2012.

[130] Everett C. Salas, Zhengzong Sun, Andreas Lttge, and James M. Tour. Reduction of graphene oxide via bacterial respiration. *ACS Nano*, 4(8):4852–4856, 2010.

[131] Gongming Wang, Fang Qian, Chad W. Saltikov, Yongqin Jiao, and Yat Li. Microbial reduction of graphene oxide by *Shewanella*. *Nano Research*, 4(6):563–570, Jun 2011.

[132] Sangiliyandi Gurunathan, Jae Woong Han, Vasuki Eppakayala, and Jin-Hoi Kim. Microbial reduction of graphene oxide by *Escherichia coli*: A green chemistry approach. *Colloids and Surfaces B: Biointerfaces*, 102:772 – 777, 2013.

[133] Yingwei Zhang, Jingqi Tian, Haiyan Li, Lei Wang, Xiaoyun Qin, Abdullah M. Asiri, Abdulrahman O. Al-Youbi, and Xuping Sun. Biomolecule-assisted, environmentally friendly, one-pot synthesis of CuS/reduced graphene oxide nanocomposites with enhanced photocatalytic performance. *Langmuir*, 28(35):12893–12900, 2012.

[134] Steffen Rupp. *New Bioproduction Systems: From Molecular Circuits to Novel Reactor Concepts in Cell-Free Biotechnology*, pages 103–123. Springer Berlin Heidelberg, Berlin, Heidelberg, 2013.

[135] Jinbin Liu, Songhe Fu, Bin Yuan, Yulin Li, and Zhaoxiang Deng. Toward a universal adhesive nanosheet for the assembly of multiple nanoparticles based on a protein-induced reduction/decoration of graphene oxide. *Journal of the American Chemical Society*, 132(21):7279–7281, 2010.

[136] Dachao Luo, Guoxin Zhang, Junfeng Liu, and Xiaoming Sun. Evaluation criteria for reduced graphene oxide. *The Journal of Physical Chemistry C*, 115(23):11327–11335, 2011.

[137] BJ Clark, T Frost, and MA Russell. *UV Spectroscopy: Techniques, instrumentation and data handling*, volume 4. Springer Science & Business Media, 1993.

[138] Q. Sun, R. Collins, S. Huang, L. Holmberg-Schiavone, G. S. Anand, C. H. Tan, S. van-den Berg, L. W. Deng, P. K. Moore, T. Karlberg, and J. Sivaraman. Structural basis for the inhibition mechanism of human cystathionine gamma-lyase, an enzyme responsible for the production of H_2S. *The Journal of Biological Chemistry*, 284(5):3076–3085, 2009.

[139] Chen Zhang, Wei Lv, Weiguo Zhang, Xiaoyu Zheng, Ming-Bo Wu, Wei Wei, Ying Tao, Zhengjie Li, and Quan-Hong Yang. Reduction of graphene oxide by hydrogen sulfide: A promising strategy for pollutant control and as an electrode for Li-S batteries. *Advanced Energy Materials*, 4(7):1301565–n/a, 2014.

[140] Karthikeyan Krishnamoorthy, Murugan Veerapandian, Kyusik Yun, and S.-J. Kim. The chemical and structural analysis of graphene oxide with different degrees of oxidation. *Carbon*, 53:38 – 49, 2013.

[141] Ohtani Bunsho. Preparing articles on photocatalysisbeyond the illusions, misconceptions, and speculation. *Chemistry Letters*, 37(3):216–229, 2008.

[142] Nan Zhang, Yanhui Zhang, Xiaoyang Pan, Xianzhi Fu, Siqi Liu, and Yi-Jun Xu. Assembly of CdS nanoparticles on the two-dimensional graphene scaffold as visible-light-driven photocatalyst for selective organic transformation under ambient conditions. *The Journal of Physical Chemistry C*, 115(47):23501–23511, 2011.

[143] M. J. Matthews, M. A. Pimenta, G. Dresselhaus, M. S. Dresselhaus, and M. Endo. Origin of dispersive effects of the Raman D band in carbon materials. *Phys. Rev. B*, 59:R6585–R6588, Mar 1999.

[144] Hui-Lin Guo, Xian-Fei Wang, Qing-Yun Qian, Feng-Bin Wang, and Xing-Hua Xia. A green approach to the synthesis of graphene nanosheets. *ACS Nano*, 3(9):2653–2659, 2009.

[145] M. Rozenberg and G. Shoham. FTIR spectra of solid poly-l-lysine in the stretching NH mode range. *Biophysical Chemistry*, 125(1):166 – 171, 2007.

[146] Shang-Hsiu Hu, Yu-Wei Chen, Wen-Ting Hung, I-Wei Chen, and San-Yuan Chen. Quantum-dot-tagged reduced graphene oxide nanocomposites for bright fluorescence bioimaging and photothermal therapy monitored in situ. *Advanced Materials*, 24(13):1748–1754, 2012.

[147] Vladimir Hlady and Jos Buijs. Protein adsorption on solid surfaces. *Current Opinion in Biotechnology*, 7(1):72 – 77, 1996.

[148] Jenny Schneider and Detlef W. Bahnemann. Undesired role of sacrificial reagents in photocatalysis. *The Journal of Physical Chemistry Letters*, 4(20):3479–3483, 2013.

[149] Jun Zhang, Jiaguo Yu, Mietek Jaroniec, and Jian Ru Gong. Noble metal-free reduced graphene oxide-$Zn_xCd_{1x}S$ nanocomposite with enhanced solar photocatalytic H_2-production performance. *Nano Letters*, 12(9):4584–4589, 2012.

[150] ZhiJun Li, JiuJu Wang, XuBing Li, XiangBing Fan, QingYuan Meng, Ke Feng, Bin Chen, ChenHo Tung, and LiZhu Wu. An exceptional artificial photocatalyst, Ni_hCdSe/CdS core/shell hybrid, made in situ from CdSe quantum dots and nickel salts for efficient hydrogen evolution. *Advanced Materials*, 25(45):6613–6618, 2013.

[151] Abdolhamid Sadeghnejad, Li Lu, Christopher J. Kiely, Bryan W. Berger, and Steven McIntosh. Single enzyme direct biomineralization of ZnS, $Zn_xCd_{1-x}S$ and $Zn_xCd_{1-x}S$-ZnS quantum confined nanocrystals. *RSC Adv.*, 7:38490–38497, 2017.

[152] Zhou Yang, Li Lu, Christopher J. Kiely, Bryan W. Berger, and Steven McIntosh. Single enzyme direct biomineralization of CdSe and CdSe-CdS core-shell quantum dots. *ACS Applied Materials & Interfaces*, 2017.

[153] Victor K. LaMer and Robert H. Dinegar. Theory, production and mechanism of formation of monodispersed hydrosols. *Journal of the American Chemical Society*, 72(11):4847–4854, 1950.

[154] Renguo Xie, Zheng Li, and Xiaogang Peng. Nucleation kinetics vs chemical kinetics in the initial formation of semiconductor nanocrystals. *Journal of the American Chemical Society*, 131(42):15457–15466, 2009.

[155] Dmitri V. Talapin, Andrey L. Rogach, Markus Haase, and Horst Weller. Evolution of an ensemble of nanoparticles in a colloidal solution: theoretical study. *The Journal of Physical Chemistry B*, 105(49):12278–12285, 2001.

[156] Lihong Jing, Stephen V. Kershaw, Yilin Li, Xiaodan Huang, Yingying Li, Andrey L. Rogach, and Mingyuan Gao. Aqueous based semiconductor nanocrystals. *Chemical Reviews*, 116(18):10623–10730, 2016.

[157] A Priyam, S Ghosh, A Datta, A Chatterjee, and A Saha. *A Brief Overview on Synthesis and Size Dependent Photocatalytic Behaviour of Luminescent Semiconductor Quantum Dots*, chapter 18, pages 271–296. World Scientific Publishing Company, 2014.

[158] T. Vossmeyer, L. Katsikas, M. Giersig, I. G. Popovic, K. Diesner, A. Chemseddine, A. Eychmueller, and H. Weller. CdS nanoclusters: Synthesis, characterization, size dependent oscillator strength, temperature shift of the excitonic

transition energy, and reversible absorbance shift. *The Journal of Physical Chemistry*, 98(31):7665–7673, 1994.

[159] W. William Yu, Lianhua Qu, Wenzhuo Guo, and Xiaogang Peng. Experimental determination of the extinction coefficient of CdTe, CdSe, and CdS nanocrystals. *Chemistry of Materials*, 15(14):2854–2860, 2003.

[160] Horst Weller. Colloidal semiconductor QParticles: Chemistry in the transition region between solid state and molecules. *Angewandte Chemie International Edition in English*, 32(1):41–53, 1993.

[161] Nguyen T. K. Thanh, N. Maclean, and S. Mahiddine. Mechanisms of nucleation and growth of nanoparticles in solution. *Chemical Reviews*, 114(15):7610–7630, 2014.

[162] Farideh Jalilehvand, Bonnie O. Leung, and Vicky Mah. Cadmium(II) complex formation with cysteine and penicillamine. *Inorganic Chemistry*, 48(13):5758–5771, 2009.

Biographical Information

Leah Spangler was born on October 4, 1990 in Lock Haven, Pennsylvania. She lived in Altoona, PA until the age 12, after which she moved to York, PA where she attended middle and high school. After graduating as salutatorian from William Penn Senior High School in 2008, she attended Drexel University for Chemical Engineering, earning a dual BS/MS degree in June of 2013. Her Masters thesis research was on extremely thin absorber solar cells, performed under the supervision of Dr. Jason Baxter. During her time at Drexel, she also completed two 6 month internships at the Philadelphia Water Department and Arkema Inc. She began her Ph.D. in Chemical Engineering at Lehigh University in September at 2013. In addition to research, she has served as ChEGA president for one year, founding the Chemical Engineering Graduate Student Symposium during that time. Leah has received the inaugural John C. Chen Endowed Fellowship, Teaching Assistant of the Year Award, the Graduate Student Life Leadership Award, and the Leonard A. Wenzel Award for Excellence in the Ph.D. Qualifying Examination. When she is not doing research, Leah enjoys taking ballet classes, cooking, and tending to her numerous pets.